THESIS

DIRECT DIGITAL MANUFACTURING OF UNIFORM THICKNESS CONTINUOUS FIBER GRID STIFFENED COMPOSITES THROUGH TOW SPREADING VIA ROLLER BASED DEPOSITION

Submitted by

Harry Ratkai

Department of Mechanical Engineering

In partial fulfillment of the requirements

For the Degree of Master of Science

Colorado State University

Fort Collins, Colorado

Summer 2024

Master's Committee:

Advisor: Donald Radford

Mostafa Yourdkhani
Paul Heyliger

ABSTRACT

DIRECT DIGITAL MANUFACTURING OF UNIFORM THICKNESS CONTINUOUS FIBER GRID STIFFENED COMPOSITES THROUGH TOW SPREADING VIA ROLLER BASED DEPOSITION

Grid stiffened structures are an effective method for lightweighting designs. While continuous fiber composites are attractive materials for creating grid stiffened structures, there are two major impediments to the wider acceptance of such structures: the high capital costs for manufacturing and the material buildup at the crossover points. The high capital costs not only come from the complex tooling but also from the need to cure the parts after deposition. The material buildup at the crossover points is not only geometrically undesirable but can reduce the mechanical performance of the part. Many options to overcome this additional thickness have been implemented, but the majority cut the continuous fiber at the crossover, further reducing the performance. Previous work at Colorado State University has demonstrated that crossovers can be manufactured using a nozzle-based gantry printer and continuous glass fiber/PET commingled tow with a minimal thickness buildup at the crossover, all with radically reduced tooling, without compromising the structural performance. Unfortunately, the direct digital manufacturing system used did not utilize a cut and refeed system for the commingled tow; thus requiring the part to be made using continuous pathing or for a person to manually stop, cut and restart the tow at the end/beginning of each discrete path. These shortfalls of the nozzle-based printer make this technology, in its current form, impractical for adoption by industry.

This work details the development of a robotic end effector for a new manufacturing method utilizing a heated roller for deposition and a programmable cut and refeed system. Initially, a comparison of the two methods of deposition, nozzle and roller, was done; both systems made crossover samples where part thickness and void and fiber volume fractions were measured. Next, an optimization of process

parameters was performed on the beam and crossover sections, separately, for the roller-based end effector. Both the beams and crossovers were evaluated using thickness measurements, void and fiber volume fraction measurements and microscope imaging. Finally, a molding shoe was attached to the end effector to determine the effectiveness of molding the beam side walls, in-situ.

It was demonstrated that the roller-based system can manufacture grid stiffened parts with less thickness deviations and fewer voids then the nozzle-based system. Additionally, optimized processing parameters were found for beams at three different deposition speeds, 450mm/min, 600mm/min and 750mm/min. Under the best conditions. The system is capable of direct digital manufacture of continuous fiber reinforced composite grids with under 2% void content. By slowing the deposition speed and increasing the consolidation force at the crossover points, the system is able to spread and thin the tow, thus, minimizing the thickness buildup at the crossover points. Using the understanding developed in determining optimized parameter two additional demonstrations of the capabilities of the system were completed: a preliminary example of full molding of the grid cross-section and the manufacture of curvilinear grids via in-plane steering. Combined, the outcomes demonstrate that a roller-based system with cut and refeed can produce grid stiffened structures with discrete fiber paths, that have crossovers of uniform thickness, at higher deposition rates than previous nozzle-based technology.

ACKNOWLEDGEMENTS

I would like to express my gratitude to Dr. Donald Radford for giving me the opportunity to perform this work at the Composite Materials, Manufacturing and Structures laboratory. This experience has helped me develop both technically and professionally and is due in no small part to his guidance. Additionally, I would like to thank all of the students at the CMMS lab, particularly Sumaiya Tanu, with whom I directly collaborated to perform the work comparing the two systems. Further, I thank the students in the MDPL lab for their support as well. Finally, I thank both my parents, Andy and Joanne Ratkai, and Taylor Cohen for providing support through this process.

This material is based upon work supported by the U.S. Department of Energy's Office of Energy Efficiency and Renewable Energy (EERE) under the Advanced Manufacturing Office, Award Number DE-EE0009404. The views expressed herein do not necessarily represent the views of the U.S. Department of Energy or the United States Government.

TABLE OF CONTENTS

LIST OF TABLES

LIST OF FIGURES

CHAPTER 1: INTRODUCTION AND BACKGROUND

Polymer matrix composites have long been popular to create structures with good specific properties, or structures with high strength to weight or high stiffness to weight ratios. For structural applications, the reinforcement type used is typically fibers, such as glass or carbon. These composites are typically manufactured in a layer-by-layer process; if done on a flat surface, the resulting part has reinforcing fibers plane parallel to the tool surface and subsequently anisotropic properties in-plane compared to through the part thickness. Additionally, the direction and amount of fibers in the plane will also alter the strength and stiffness of the part depending on the direction of the loading, resulting in further anisotropy. This ability to tailor the properties of the material allows for an optimization of the material properties as well as the part shape; this is the major advantage of continuous fiber polymer matrix composites over traditional isotropic materials and where significant weight savings can be realized.

1.1 Traditional Composites Manufacturing

A variety of manufacturing methods are available to create composite structures. These methods can be separated into two general categories: closed molding and open molding.

1.1.1 Closed Mold Techniques

Closed molding techniques include resin transfer molding (RTM), pultrusion, and compression molding. In these processes, the parts are cured in a sealed mold on all sides. This results in parts with a predefined, accurate geometry and good surface finish on all part surfaces.

RTM is a process in which a dry fabric or preform is placed in one half of the mold; the second half of the mold is closed, and the resin is injected into the mold under high pressure. This is generally limited to thermosetting resins as a low viscosity resin is needed to permeate the preform or fabric. One variant on

this process is vacuum assisted resin transfer molding (VARTM) where the preform is subjected to vacuum inside the closed mold before the resin is injected. This not only pulls the resin through the preform, but more importantly, removes void causing air from the preform. While this process does have good geometric control over the parts and can quickly process parts, there is significant capital investment. This is due to the press needed for rapid processing and the high surface quality molds. Further, this process is generally limited to smaller parts [1].

Pultrusion is a process in which reinforcing fibers are drawn into a constant cross section heated die where the part is cured. The reinforcing fibers can be unidirectional tow (UD), braid, woven or non-woven broad goods, or a combination thereof. For thermosetting matrix pultrusion, the fibers are run through a resin bath whereas for thermoplastic pultrusion, the feedstock is typically prepreg or comingled tow. Advantages of this process are generally very controlled and high fiber volume fraction while using lower cost materials, especially for thermoset matrix pultrusion. Unfortunately, the parts are limited in complexity.

Compression molding is similar to RTM where the constituent materials are pressed between two matching molds and pressure is applied, generally by a press. Compression molding can use discontinuous fiber feedstocks such as long fiber thermoplastic pellets in a plasticizer or sheet molding compound [2]. Alternatively, thermoplastic tapes or commingled tow are two fiber forms that allow for continuous fiber parts to be made using compression molding [3].

1.1.2 Open Mold Techniques

Open mold techniques are characterized by having a single molded surface; this includes hand lay-up, resin infusion molding (RIM) and fiber placement. The part geometry is dictated by the tool surface but also by how much material is then placed on that tool. The thickness of the part can be changed if more or less material is placed on the mold.

Hand lay-up can be done with fibers hand impregnated with wet resin. This is generally difficult to control the resin and fiber volume fraction, especially part to part. A much more reliable method of controlling the content of the constituent materials is to use prepreg. Prepreg or pre-impregnated fibers can come in a variety of form such as UD tapes, UD fabric and both woven and non-woven broad goods. The fibers of thermoset prepreg are covered in a partially cured B-stage resin. This results in material with good tack, which aids the lay-up process. Thermoplastic prepreg has virtually no tack and because of this, it makes hand lay-up of this material difficult and impractical. The fabrics are cut to shape prior to lay-up. For both wet resin and prepreg hand lay-up, the part is generally bagged, and vacuum is applied to the part after all the lay-up has been complete. This removes voids, can remove excess resin and provide consolidation to aid in the fusion of the layers. Further, thermosetting resins need to be cured, which generally takes place at elevated temperatures. This can be done in an oven or in an autoclave; the autoclave is a heated, pressurized chamber. The autoclave, in combination with vacuum, further assists in removal of voids, additional consolidation of the part layers, and can keep volatiles dissolved in the solution. Hand lay-up can be used to make complex shapes of large size but is labor intensive and complex parts require complex tooling. Further, prepreg is generally expensive, has a limited shelf life and must be kept refrigerated. Additionally, if used, autoclaves require large amounts of capital to purchase and large amounts of energy to run. Finally, the part must be able to fit in the autoclave, limiting the size of the parts that can be made.

RIM is similar to VARTM with only one mold half. In RIM, a hand lay-up is done on the tool using dry fibers; this is analogous to placing the dry fiber preform in the mold for VARTM. Once all the fiber has been laid-up, the tool is covered in some kind of transport media and then a vacuum bag. Transport media is a consumable material that aids the in the flow of liquid resin. Once the part is sealed under the bag, the part is subjected to a vacuum, pulling out excess air and consolidating the part. Liquid resin is then introduced; unlike with RTM, the resin is pulled in via the vacuum instead of being injected in. RIM

is one way to produce large, out-of-autoclave parts with low void content. Additionally, the constituent materials used in RIM are generally cheaper than prepregs. Unfortunately, the fiber volume fraction has an upper limit of ~55%.

1.2 Automated Tape and Fiber Placement

Automated tape placement and automated fiber placement (ATP/AFP) are practically the same process but done with different feedstocks. ATP utilizes pre-impregnated tapes which can range from 75mm to 300mm whereas AFP uses individual tows in parallel; AFP can use up to 32 tows in parallel ranging from 1/8in to 1/2in wide tows [4]. Both of these techniques effectively replace the manual lay-up process, increasing the speed and accuracy of the placement process while reducing the amount of material scrap [5]. The rapid speed of deposition, beyond 1000mm/s, makes this technology well suited for large acreage parts such wing skins and fuselages. The basic concept of this technology is the tapes or tows are deposited onto the tool surface via a deposition roller. In general, due to the width and inability to readily shear the feedstock composite tape, these processes place material in straight paths. The incoming material and substrate surface is heated to increase tack and can help to reduce entrained voids between plies. Heat can be supplied by a variety of sources such as hot gas, infrared, pulsed light/flashlamp and laser [6], [7], [8]. An image of the placement process can be seen in Figure 1.

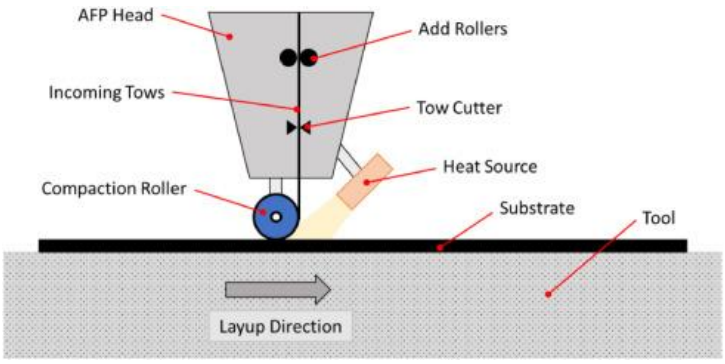

Figure 1: ATP/AFP lay-up process [4].

A more in depth look at the heat sources and variations on roller geometry and types follows.

1.2.1 ATP/AFP Heat Sources

As previously stated, a variety of heating methods exist for heating the incoming tapes as well as the substrate. The first patent filed for an ATP head was done in the early 1970's and utilized a quartz heat lamp to increase the tack of the incoming thermosetting tape [9], [10]. IR lamps are generally used for thermosetting materials and has good temperature response but has unwanted heating of adjacent plies and placement equipment [4], [11]. The use of hot gas torches is one of the simplest methods but is generally less controlled than IR lamps. Hot gas torches generally have worse performance than other methods as the forced convection is not as directed, as a result the hot air heats adjacent plies and the placement equipment. Additionally, the hot gas temperatures have to be extremely elevated for in-situ consolidation of thermoplastic composites. The main draw for using hot gas is low capital costs [4], [11], [12]. Pulsed light/flashlamp are more efficient than IR lamps, allowing for faster deposition and less residual heat transfer to the part when the lamp is turned off [13]. Lasers allow for localized heating of individual tows, rapid response and very high deposition rates [14], [15]. Lasers are generally the most expensive method of heating the incoming tow, but because of the power density, frequently they are used for materials needing higher deposition temperatures, such as PEEK.

Another issue exists for radiative heating methods. While Funck et al were able to use lasers with preheated glass/PPS and glass/PP tapes, previous unpublished work within the lab groups indicate heating of glass fibers with a laser may be ineffective [15]. Because glass only absorbs a limited range of wavelengths of light, the output wavelength of the laser must match that of glass to effectively heat the incoming tape. Alternatively, the matrix material can be dyed or contain fillers so that it absorbs the incoming radiation [16].

1.2.2 ATP/AFP Deposition

In these tape placement processes, consolidation is typically done using a roller; an alternative was developed by Accudyne Systems for in-situ consolidation. This head had a preheated zone and compacter that provided the initial contact between the incoming tape and the substrate. A second heated compacter that was responsible for the polymer healing and intermingling of polymer chains between layers. Finally, a cooling compacter froze the material in place. For all of these zones, rigid steel shims were used in parallel in an effort to conform to the complex surfaces often seen in parts [17]. Examples of the compactors can be seen in Figure 2 (a) and (b).

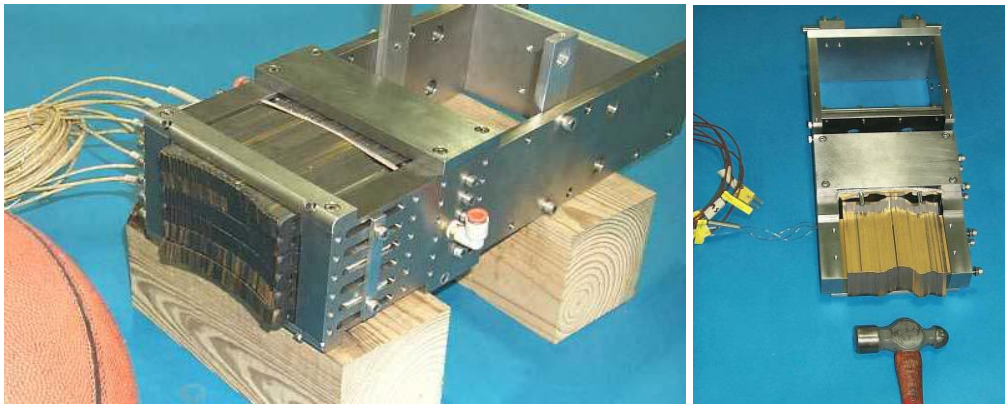

Figure 2: (a) left image of “area” compactor and (b) right image of “line” compactor [17].

While no mention was made in the paper about the effectiveness of such a design, this has not been widely adopted by industry [18].

Often, the compaction rollers used feature a rubber sleeve around a metal core which is supported by bearings. Due to the high temperatures that can be experienced by the roller, the rubber sleeve is often silicon. While the rubber sleeve style of roller is common, there are some issues with the pressure distribution, particularly when the mold has relatively small radii of curvature [19]. This can be seen in the pressure distribution plots in Figure 3 where the red areas are areas of high pressure.

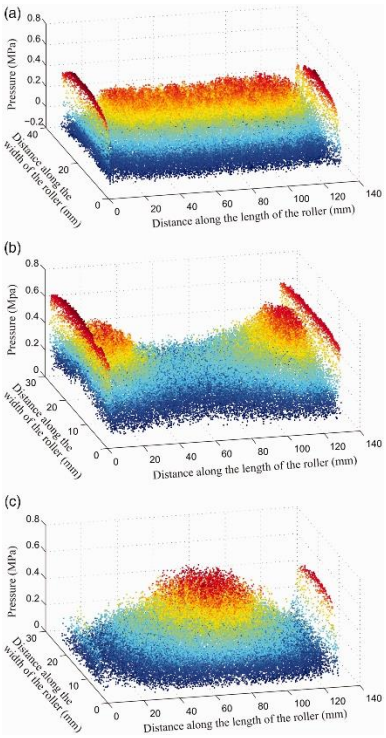

Figure 3: Pressure distribution on the roller surface with a: (a) flat mold, (b) concave mold and (c) convex mold [19].

Optimization of the silicon sleeve length, thickness, hardness and internal structure was done by Jiang et al. [19]. While changing the internal structure of the sleeve can create a larger contact area, Bakhshi et al. noted that using a perforated roller caused defects as there were local variations in the compaction pressure [20]. The roller used and the defects can be seen in Figure 4.

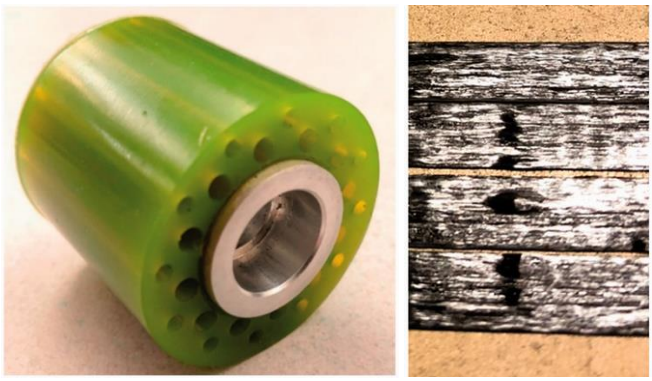

Figure 4: Perforated roller (left) and “blister” defect caused by pressure variations (right) [20].

Having a roller that can conform to the tool surface can also be done using segmented silicon rollers as seen in Figure 5.

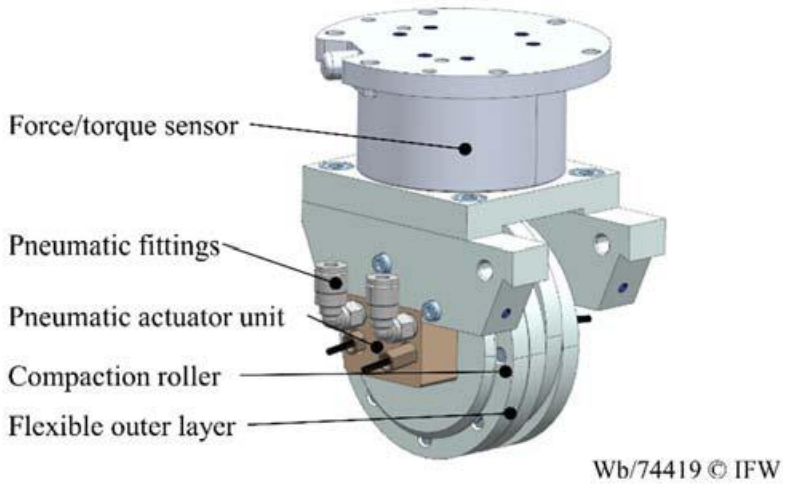

Figure 5: Compaction head with a multi-segment roller [7].

This does increase the complexity of the system which is why this design has not been adopted on a large scale [19].

1.2.3 ATP/AFP In-situ Consolidation

For thermosetting matrix materials, the part still needs to be cured which is typically done in an autoclave. For thermoplastic matrix materials, aerospace quality parts are often placed in an autoclave to remove voids and improve fiber distribution [8]. However, because thermoplastic composites do not have to be cured, the matrix just has to be heated beyond the melting temperature, the parts can theoretically be made and consolidated in-situ. This offers the advantage of a true “one shot” process that reduces the tooling required as no autoclave is needed, increases process speed and reduces the energy required to make the parts [8], [12], [14], [17], [21]. While in-situ consolidated composites offer good advantages, the quality does not meet the expectations set by autoclave cured composites. One of considerations when manufacturing using in-situ consolidation, is the fusion between the layers of the composite. With an autoclave, the matrix is above the melt temperature of the plastic and exposed to the elevated pressure for a long duration. The elevated temperature drops the viscosity of the matrix easing the flow [22]. When the matrix is subjected to elevated pressure for a long duration, the matrix can flow a greater distance [23]. As seen in the left sample in Figure 6, the fibers (white dots) are much

more evenly distributed and there are no large resin rich areas (light grey area). The resin rich areas, as seen in the right sample in Figure 6, indicate the regions between the layers, which are more likely to contain voids [8].

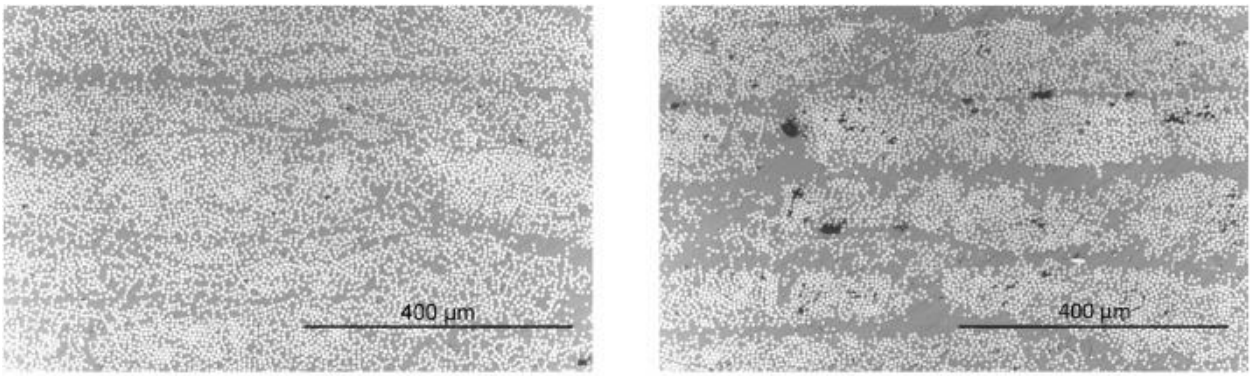

Figure 6: Micrographic imaging exemplifying autoclave vs. in-situ consolidated thermoplastic composites [8].

For in-situ consolidation, the process of interlayer fusion can be divided into three parts: intimate contact, interdiffusion and solidification. This process is dependent on the flow of the matrix which is a function of pressure in the resin, the resin viscosity and the time of exposure to the pressure The pressure in the matrix is dependent on the force applied during consolidation but also the contact area of the roller. The viscosity of the matrix is dependent on the heat flux of the heat source and time of exposure to this heat source. Finally, the time the matrix is under pressure not only based on the speed of deposition but also the size of the contact patch of the roller [21], [24], [25], [26].

Some work has been done to determine if further consolidation can be done with additional passes without laying down more material. This is referred to a repass. The effect on the mechanical properties and void content is positive but still relatively minimal. However, this can have a significant improvement on the surface finish for the final layer [27], [28]. This is critical for out of autoclave composites that are external aerospace structures such as wing skins.

1.3 Grid Stiffened Composites

Grid stiffened structures have long been used as a method for lightweighting. Traditionally machined out of an aluminum billet, fiber reinforced composite grid stiffened structures are very attractive for such a design based on the high specific properties and greater tailorability of the reinforcing fibers. Additionally, grid stiffened structures show good damage tolerance and load path redundancy [29]. However, manufacturing composite grid stiffened structures is not without issues. Design, manufacturing, cost, quality control, and a relative lack of knowledge about these structures have made it difficult for industry to adopt, mature, and implement composite grid stiffened components.

One issue with manufacturing continuous fiber composite grid stiffened structures is build-up of the reinforcement at the intersection points; where there is twice as much fiber at the crossover point as in the straight rib sections. The material and thickness build-up at the intersections leads to fiber bridging which in turn leads to resin rich areas, before and after the crossing plies. The ribs, before and after these intersections, were the failure sites when Buragohain et al. performed compression testing on a cylindrical lattice structure [30]. Traditional manufacturing methods of composite grid stiffened structures rely on the expansion of the specialty tooling to provide lateral compaction of the ribs [31]. While this improves the mechanical properties and in-plane geometric control, it does not address the thickness deviations at the crossover points. Zhao et al., made grid stiffened structures using Automated Fiber Placement (AFP) and attempted to decrease the fiber waviness at the nodal intersections by introducing discontinuous tows at the crossover points. While this reduced the thickness differences between the ribs and intersections, the introduction of discontinuous tows did drop the compressive and bending properties [32]. Lee et al. proposed a rib compression method using rollers to minimize voids and fiber spreading in the thickness direction at resin rich areas [33]. Fiber build up at the intersections can be seen in figures 7 and 8.

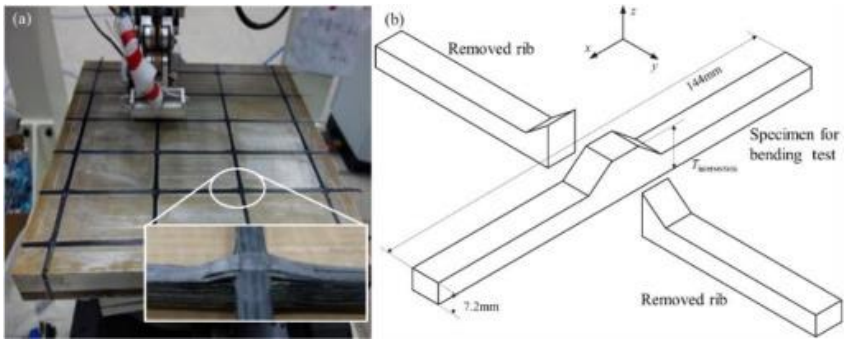

Figure 7: Aluminum tooling and fiber build up at intersections [32].

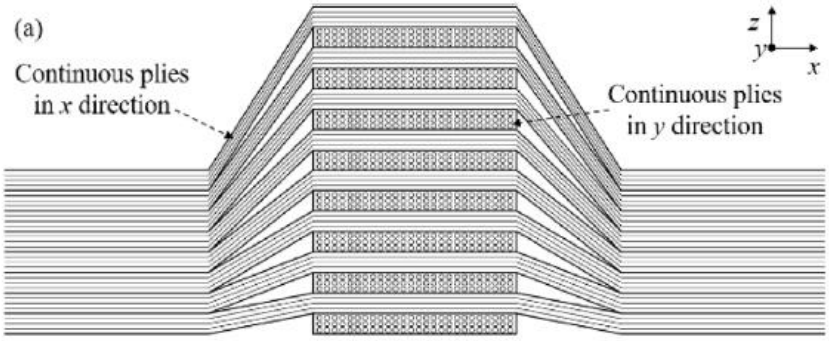

Figure 8: Fiber "bridging" due to material build up at crossovers [32].

Another issue with the manufacture of composite grid stiffened structures is the required tooling complexity. The earliest method of manufacturing tooling for grid stiffened panels was either by milling or fabrication of aluminum. Buragohain et al. used a polyurethane (PU) foam mandrel with grooves machined into it. Not only was the tool sacrificial, but the use of a 4-axis mill was necessitated [30]. Ahmadi et al. created an isogrid mesh by dry weaving fiber roving along the grooves of a silicon mold and then filled the grooves with epoxy resin [34]. This approach has the disadvantage that when the stacked fiber height exceeds the silicon guide, the fiber slips over the silicon guide and spreads out. Lee et al. prevented this by using an adhesive like paper tape to hold the fiber near the silicon guide, preventing the fiber from spreading [33]. When using expansion block tooling, each block is machined individually and sized carefully, or is cast in high tolerance tooling, to ensure part quality. Improper fabrication can cause higher loads to concentrate at the intersections. Vacuum assisted resin transfer molding has also been an alternative used to manufacture grid-stiffened panels, but this method is costly

for long composites parts due to the two-sided, closed mold requirement and due to the number of fixtures required in the process [35], [36].

1.4 Digital Manufacturing

Digital manufacturing is synonymous with 3D printing and has great promise for application to continuous fiber composites. For neat polymers, traditional filament extrusion (fused filament fabrication or FFF) offers the ability to rapidly manufacture parts, more complex than is possible with traditional manufacturing, like injection molding or machining. Further, FFF does not require the high capital costs of injection molding for the tooling, i.e. molds. Also, there is less material wasted as FFF is not a subtractive process, like machining. For continuous fiber composites, these advantages still hold true in theory. One of the difficulties is to achieve sufficient consolidation during the printing. Several companies have come up with different solutions to this issue and made commercially available 3D printers that utilize continuous fiber feedstock. These companies include Markforged, Anisoprint, and 9T Labs. All of these companies use a pre-impregnated filament as the continuous fiber feedstock. Markforged uses a heated nozzle and a heated pressure foot to help “iron” the continuous reinforcement into the part; it should be noted that the Markforged printers cannot exclusively use the continuous fiber feedstock in the manufactured parts. Some amount of the part has to be printed using neat polymer filament or polymer filament filled with discontinuous fiber. A substate has to be printed for the continuous fiber to be pressed into [37]. Anisoprint has a flat-bottomed heated nozzle that provides consolidation. Also, this process has two different matrix materials. The pre-impregnated continuous fiber feedstock is impregnated with a thermosetting polymer and then cured. This is then passed through a chamber of molten thermoplastic to manufacture parts [38]. 9T Labs employs a process where the part is initially “laid up” or printed where the reinforcing fibers are positioned. Then the part is placed into a compression molding machine where it is consolidated, fusing the layers and pressing out the voids [39].

At the CMMS lab, systems have been developed that have demonstrated advantages of digital manufacturing. While in-situ mixing has been explored, the most successful systems have utilized commingled tow passing through a heated nozzle [40], [41]. The nozzle had a flat nose, parallel to the build plane that provided consolidation. This can be seen in figure 9.

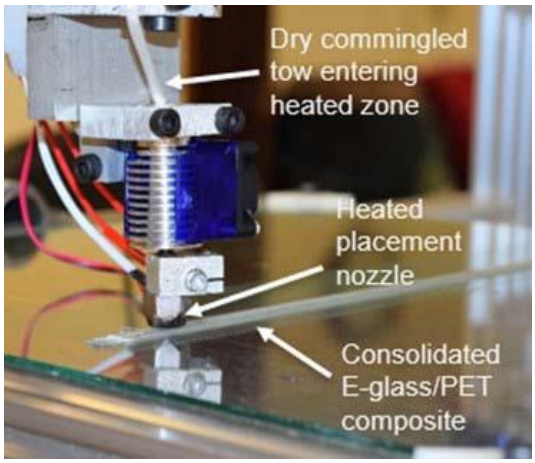

Figure 9: Composite printer with flat nosed nozzle [46].

One of these systems developed by Warlick et al., is a modified filament winder and was able print non-geodesic path. The geometric accuracy of the printed parts was improved by adding force convection cooling. This “froze” the tow in place forcing the sheared fibers to remain in place when the direction was changed [42], [43], [44]. Rodreguiz et al. developed a spring mechanism to control the force applied and implemented this on a 3-axis gantry printing system. This can be seen in Figure 10.

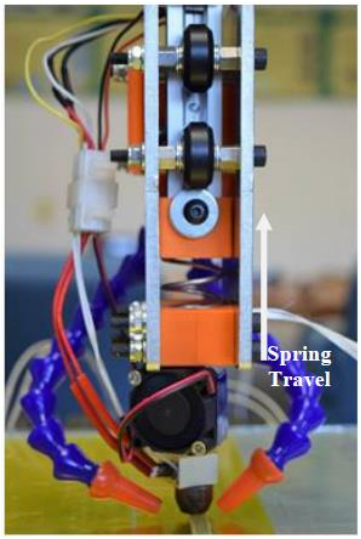

Figure 10: Spring loaded deposition head with flat nozzle [45].

This system was used to evaluate the effect consolidation force had on digitally manufactured composites; it was determined that increasing the consolidation force resulted in improved short beam shear strength [45]. Additionally, using this system, use of DMA results was correlated to void content and it was determined that slowing the deposition speed reduced the number of voids [46], [47]. Bourgeois et al. used the 3-axis gantry printer and a modified nozzle to manufacture truss core samples [48]. This 3-axis system was then modified to accommodate two additional axes. This was used to determine the tow had a varying final geometry depending on the angle of the nozzle; thus, for printing off the tool surface, it is extremely advantageous to have manipulate the nozzle to be perpendicular to the print path [49]. Finally, Hogan et al. examined high aspect ratio beams and it was found that there was not an increase in void content through the thickness of the beam [50].

1.4.1 Digital Manufacturing of Grid Structures

Costly 'trial and error' can be avoided, and the scrap rate can be minimized, by employing fiber placement heads with advanced capabilities and variable tow width handling in automated methods of fiber deposition. Two primary technologies: AFP and ATL using pre-impregnated fiber tows that can be placed or stacked to construct a grid of the required height. Compared to traditional manufacturing

processes, these methods offer quality, stability and placement efficiency [51]. Additionally, automated placement methods enable cost-effective production of large, complex, and high-quality components in a single step. However, in order to avoid fiber bridging during AFP, Netherlands Aerospace Center (NRL) demonstrated that cutting half of the tapes in one direction and the other half in the opposite direction at the intersections of orthogrid stiffeners was necessary [52]. Unfortunately, this results in a more complex grid intersection design and negatively effects the fiber continuity.

Previous work has demonstrated the manufacturing of high quality, high fiber volume fraction grid stiffener beams by direct digital manufacture with radically reduced tooling requirements. This research by Hogan et al. demonstrated the use of continuous fiber reinforced thermoplastic commingled tow to produce multi-layer, high aspect ratio grid stiffener beams directly on a tool surface without any channels or guides [50]. A fiber volume fraction in excess of 50% was reported, using a commingled glass/PET. In follow-on work by Hogan, it was determined that tow spreading, and ultimately tow thickness, could be effectively controlled through the variation of consolidation force of the hot nozzle used for the deposition of the commingled tow [53]. Further, this research culminated in the demonstration of grid intersections, which, through the local control of the processing parameters, had nearly equal thicknesses in the intersection and in the straight stiffener region, as shown in figure 11. The maintenance of thickness throughout the demonstration intersection, produced by Hogan [53], relied on local spreading and thinning during placement which yielded both a higher local fiber volume fraction at the crossover and a widening through local tow spreading.

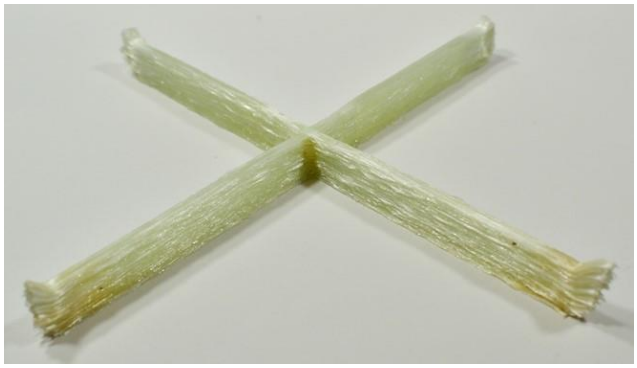

Figure 11: 40-layer stiffener grid intersection demonstration [53].

1.5 Cutting Systems

The need for a cut and refeed system is necessary of the advancement of the printing capabilities at the CMMS lab. Understanding the mechanisms for severing high performance fibers is necessary to accomplish this task. One of the simplest methods for producing discontinuous fiber composites is a spray-up manufacturing method. In this method, dry, unimpregnated tow is fed into a handheld gun known as a “chopper gun”. This system has a bladed roller which is pneumatically actuated. This roller is in contact with a softer rubber anvil roller. As the bladed roller rotates the tow is fed between the rollers and then severed by the blade. The severed fibers are then ejected out of the cutting system where it is intermixed with a spray of resin. This can be directed towards the part to build the part thickness. A chopper gun can be seen in figure 12 and the spray-up process can be seen in figure 13.

Figure 12: Chopper gun [54].

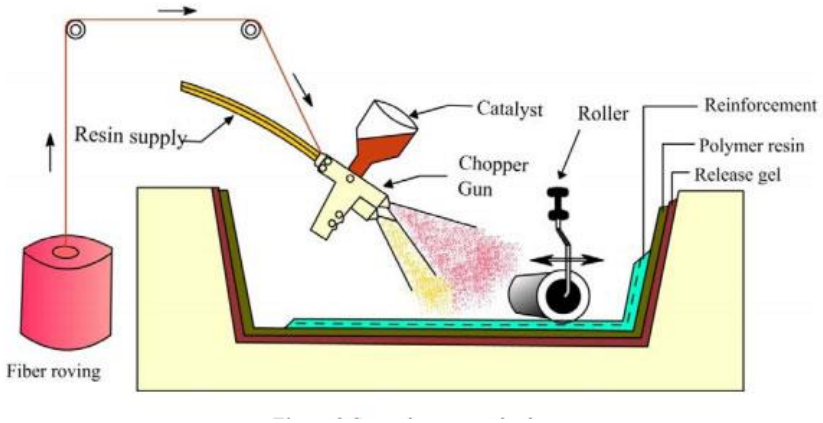

Figure 13: Spray-up process [55].

Generally, the spray-up process is used for low performance parts as the discontinuous fibers generally have worse performance than continuous fibers and the in-plane isotropy of the final part is not optimal for the minimization of weight. Additionally, lower performance resin systems are typically used in this process as well as low-cost glass fibers.

Sheet molding compound is another application of discontinuous fibers. The cutting method is the same as in a chopper gun where a bladed roller rotates, driving the deformable anvil roller, and severs the fibers when the blade contacts the fibers and anvil roller. This is then mixed with a B-stage resin for use in compression molding. In deformable backing cutting, like what is done using a chopper gun or for manufacturing sheet molding compound, the failure mode of the fiber is bending, not shearing. The differences in failure surfaces can be seen in figure 14.

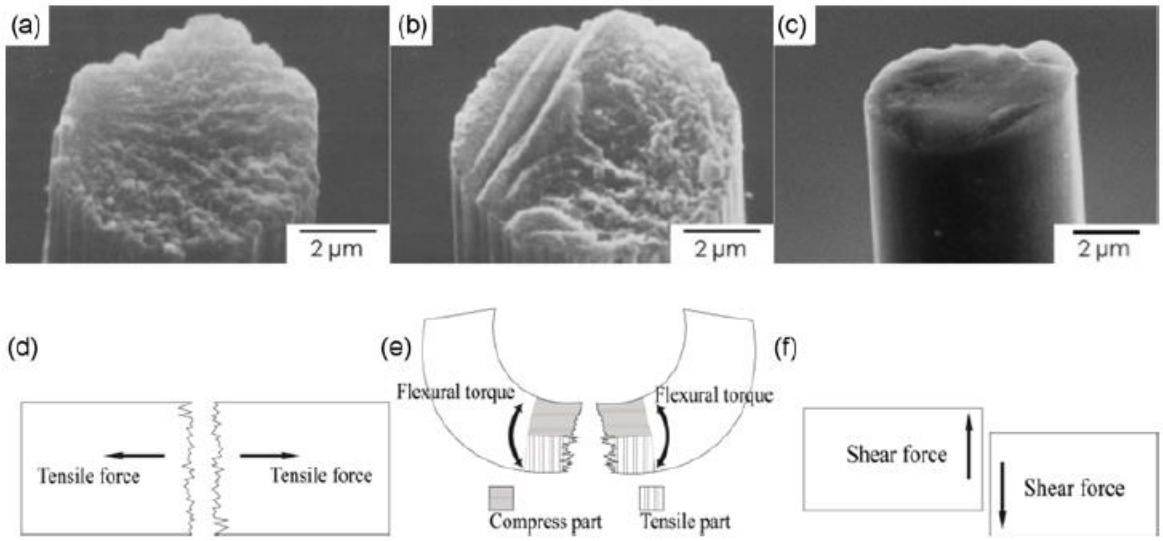

Figure 14: Different failure surfaces (a-c) and corresponding failure modes (d-f) [56].

This method of cutting is advantageous as this reduces the required cutting force to sever the fibers compared to shearing or crushing the fibers [57]. Additionally, increasing the durometer of the anvil roller increases the force during cutting [58]. Further, as the anvil roller wears, grooves form in the regions where the blades are in repeated contact. This “meshing” of the blade in the anvil roller reduce the wear rates on the blades [59]. Increasing the hardness of the blade also reduces the wear rate on the blades [60]. All of this research was done on reinforcement only, not any prepreg or commingled tow.

One researcher did look at severing against a deformable backing of glass/polypropylene commingled fibers for use in preforming. Due to the differences in ductility between the reinforcement and the matrix fibers, the mechanism of cutting was different. The brittle reinforcing fibers fail via bending as the anvil roller forces the fibers to bend and conform to the sharp radius of the blade. The thermoplastic fibers in the commingled tow could easily conform to the radius of the blade and subsequently would not sever. This was attributed to the cutting temperature being above the glass transition of the plastic fibers. Theoretically, cutting could take place at a colder temperature, but the low glass transition temperature of polypropylene (-18C) makes this impractical. However, because of the visco-elastic nature of thermoplastics, the matrix fibers were strain rate sensitive. As a result, the cutting of the

commingled tow improved with increasing line speed. Additionally, increasing the hardness of the anvil roller caused better severing of the plastic fibers [61].

1.6 Hypothesis/Goals

Based on the literature evaluated, including prior efforts in the CMMS lab, the current nozzle-based continuous fiber commingled tow digital manufacturing system is limited in terms of the manufacture of grid stiffened structures. Limitations include deposition rate, effectiveness of control of the consolidation force, and the inability to create discrete fiber path lengths without operator intervention. It is hypothesized that implementing a roller-based placement system with force feedback control will result in an equivalent quality composite, using the same commingled tow feedstock, while improving consolidation consistency are increased speeds, and the incorporation of a cut & refeed system will enable discrete fiber path lengths, reducing the need for operator intervention.

CHAPTER 2: SYSTEM DEVELOPMENT

As previously discussed, the work done at the CMMS has demonstrated the capabilities of digital manufacture of composite structures. The nozzle-based systems can manufacture objects at the lab scale but are not appropriate for industrial applications. The primary issue with these systems is the lack of a cut and refeed system. Manufacturing using the nozzle-based systems requires either manual starting, stopping and cutting or making objects where the fibers follow a continuous path. Manual starting and cutting is not desirable as it requires operator intervention, decreasing the level of automation of the process. Use of continuous pathing can minimize this issue but is not without fault. An example of continuous pathing can be seen below in figure 15; the left image is the manufactured structure while the right image is the structure of interest [50].

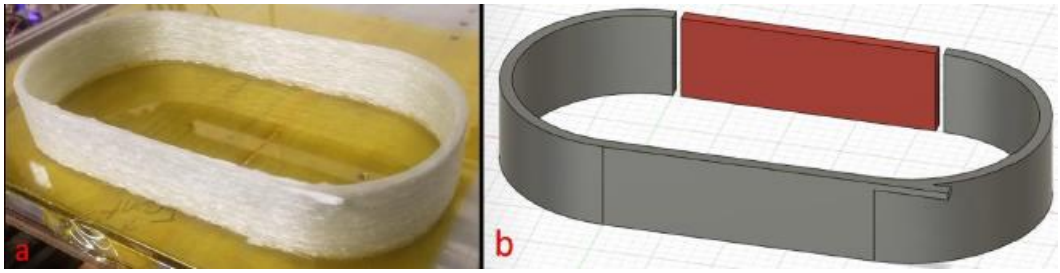

Figure 15: Continuous path manufactured by Hogan et al. [50].

Not only can this manufacturing method lead to substantial amounts of wasted material but can increase the process time and can limit the geometries that can be manufactured. As such, a cut and refeed system could eliminate these issues.

2.1 Cut and Refeed Previous Work

While the nozzle-based deposition can produce low void fraction composites and maintain a good ability to perform tow steering, the system has one major drawback: the lack of a cut and refeed system. Without this system, continuous paths must be employed for the print to be automated; discrete pathing must include a manual cutting and restarting of the tow. Previous efforts have included attempts

to cut the tow after pultrusion from the nozzle [62]. This design had some success but lacked a defined method of restarting the tow after cutting and can be seen in figure 16; the next iteration on the design needed to incorporate an active feed until the tow tacked. Finally, because the system used a nozzle for deposition, refeeding through the nozzle would require a rigid consolidated rod of composite. Utilizing the rigid rod for refeeding could limit the ability of the system to steer the tow. With these considerations in mind, an investigation into a roller-based deposition and a refeed system, more analogous to ATP/AFP, was undertaken.

Figure 16: Previous attempt at developing a cut and refeed system [62].

Due to the difficulty of refeeding and tacking with a nozzle-based system, a system using roller-based deposition was investigated. The use of a deposition roller as opposed to a nozzle was thought to aid in tacking as roller was free to rotate, reducing the friction on the tow during refeeding. A system with the designed for AFP/ATP had been previously made by Bahar et al. which utilized a bladed roller to cut incoming tape for AFP. The blade could be actuated along the length of the roller to have selective cutting. Additionally, the system utilizes a servo motor to engage the rollers in active feed (pushing the tape) and passive feed (tape being pulled through via tension). While this system ensures that the tow or tape is nipped during the cut and can feed indefinitely, the system is complex as seen in figure 17. The system has three actuators: a stepper motor to drive the feed/anvil roller (Roller 1), a servo motor to

engage the cutting roller (Roller 2) and a linear solenoid to move the cutting blade into/out of position [63].

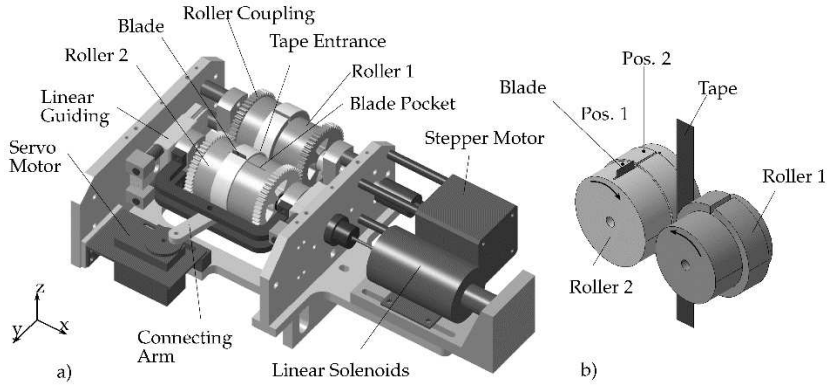

Figure 17: Integrated feed and cutting unit developed by Bahar et al [63].

Chopper guns and sheet molding compound machines also utilize bladed rollers to cut incoming tow against a deformable backing; both of these systems can cut the fibers while feeding the fibers forward but can only do so for predetermined lengths of fiber. A system needed to be made that simplified the design from Bahar et al. but could have “active” feed, nip the tow after cutting, and deposit continuous fibers. Nip refers to the pinch point of the tow between two rollers or a roller and a substrate as seen in figure 18.

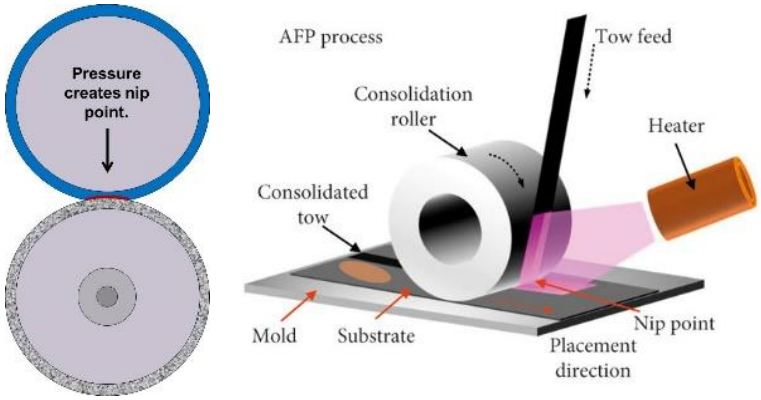

Figure 18: Nip point between two rollers (left) and between a roller and a surface (right) [64], [65].

2.2 Cut and Refeed

A bladed roller and an anvil roller were selected as the method of cutting as it will nip the tow as the cutting occurs. While this does eliminate the issue of nipping and feeding the tow after cutting, it requires the blade to actuate in order to deposit continuous fibers. Having the blade actuate independent of the roller, as done by Bahar et. al., would enable the system to have an “active” feed but would increase the complexity dramatically. Recognition that the tow only had to be fed until it was under the deposition nozzle or roller meant that the system only needed to feed the tow forward a finite distance. Further, the finite feeding of the tow meant that the bladed roller or the anvil roller could actuate as opposed to the blade itself actuating. This led to the design incorporating a bladed roller from a chopper gun, a spring-loaded anvil roller and a cam to move the anvil roller in and out of nip. The cam action can be seen in figure 19. Original concept for the system, including the heated nozzle/guide can be seen in figure 20.

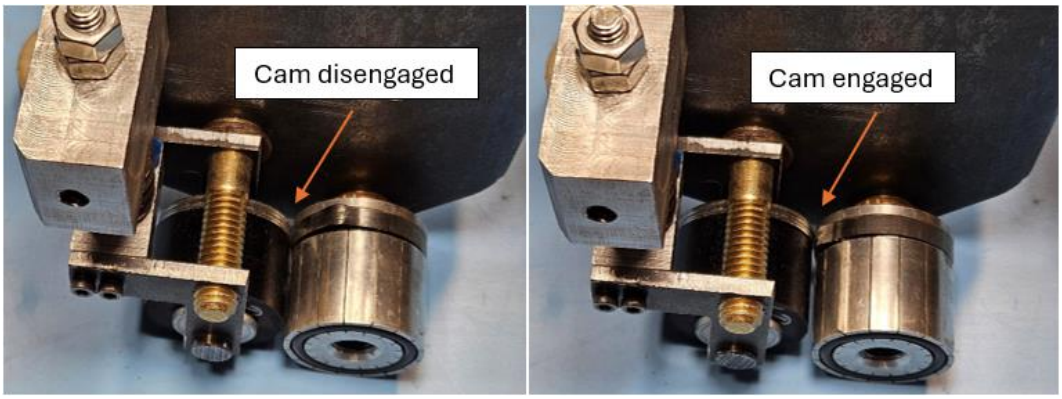

Figure 19: On the left, the cam is disengaged and there is no gap between the feed and anvil rollers. On the right, the cam is engaged and there is a gap between the rollers.

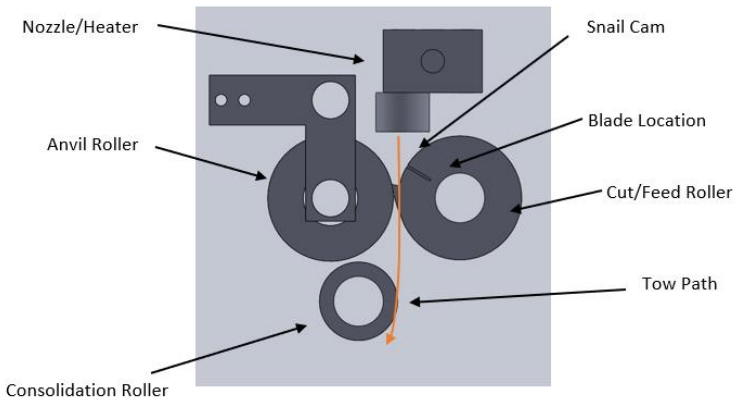

Figure 20: Original concept for cutting and heating prior to cutting.

The only driven part of the system is the bladed roller via a belt and pulleys. The cam is attached to the bladed roller in order to control the position of the cam. The anvil roller has a roller follower to interact with the cam. When the cam engages, the anvil roller is pushed away from the bladed roller, opening the nip point so the tow can be easily pulled through the system. This can be seen in figure 21.

Figure 21: Cam is engaged, and fiber can be pulled through (a), tow is pinched (b), blade contacts tow (c), tow is severed and fed forward (d), finally, tow is refed (e).

When it is time for the tow to be cut, the bladed roller rotates forward, and the cam disengages. The tow is then pinched between the bladed roller and the anvil roller. As the bladed roller continues to rotate forward, the blade comes into contact with the anvil roller, cutting the tow. Once the fibers are cut, the tow is immediately pinched in the nip and the fibers are then fed forward. As the bladed roller comes close to completing one revolution, the cam re-engages and the rollers separate, allowing the tow to be pulled through the system freely. Allowing the tow to be pulled through easily aids in refeeding and restarting the tow after cutting as there is less tension in the tow. As a result, the tow is easier to tack during the restart.

An anvil roller from a chopper gun was also purchased with the other chopper gun parts. The purchased anvil roller was made from 80A polyurethane. As part of the initial verification, the cut and refeed system was tested with a cold, dry commingled tow. The tow was a glass/PET commingled tow with an unprocessed glass fiber volume fraction of 55%. This worked without any issue, the glass fibers being severed every time.

2.2.1 Heated Cutting Attempts

With the cutting mechanism designed, the rest of the system needed to be designed. With all the previous lab experience with nozzle-based deposition, the original concept was to use a nozzle to heat and initially wet out the tow. The final deposition of the tow would be done by a roller after passing through the cut and refeed system. Once initially heated, the tow needed to be kept at the elevated temperature to ensure the individual fibers could shear, allowing the tow to be steered. This, in turn, meant that the cut and refeed system as well as the deposition roller must be heated as well. Due to the high temperatures required the majority of cut and refeed system to be made from steel; the only pieces from the original design that were not made from steel were the aluminum heat block, the brass nozzle and the aluminum roller from the chopper gun. For initial testing, the heat block and nozzle temperature were controlled via Azteeg X3 and heated with a 40W cartridge heater and was heated to 250C. During the first phase of the testing, only the heater block and nozzle were heated. This resulted in the tow freezing and sticking to one of the rollers after being nipped. This can be seen in figure 22.

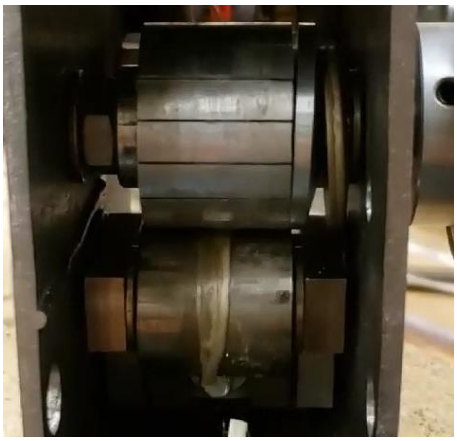

Figure 22: Tow freezing and adhering to anvil roller.

When this occurred, the tow could not be effectively refed. To resolve the tow sticking to the anvil roller, the whole system was heated, not just the nozzle. To heat the rest of the system, a heat gun was used to heat the nip of the anvil and cut roller up to 240C. This was verified with a thermocouple. When the rollers were hot, the thermoplastic resin reduced the friction between the tow and the rollers, so the driven roller just spun against the tow, not feeding it forward. Once the rollers cooled slightly, the rollers would nip the tow and push it forward, but the material was significantly damaged. This can be seen in figure 23.

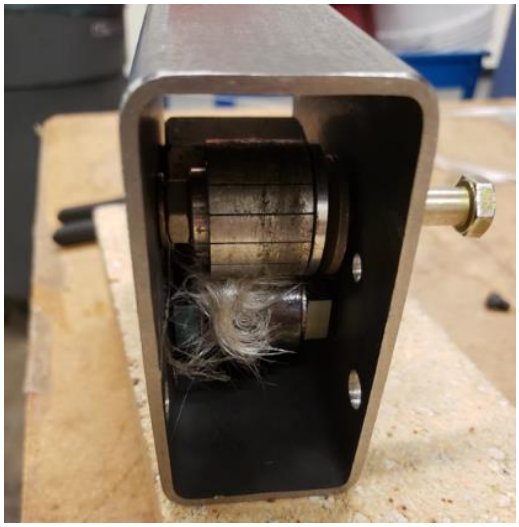

Figure 23: Tow damaged from free spinning rollers.

After testing the system at high temperatures, both rollers were polished and released. The tow initially slipped against the rollers as it did before. Once the rollers were heated to approximately 100C, the tow fed intermittently, still slipping against the rollers. Eventually, the tow rubbed enough of the release off so that feeding was more consistent, but some thermoplastic began to build up on the feed roller. This can be seen in figure 24.

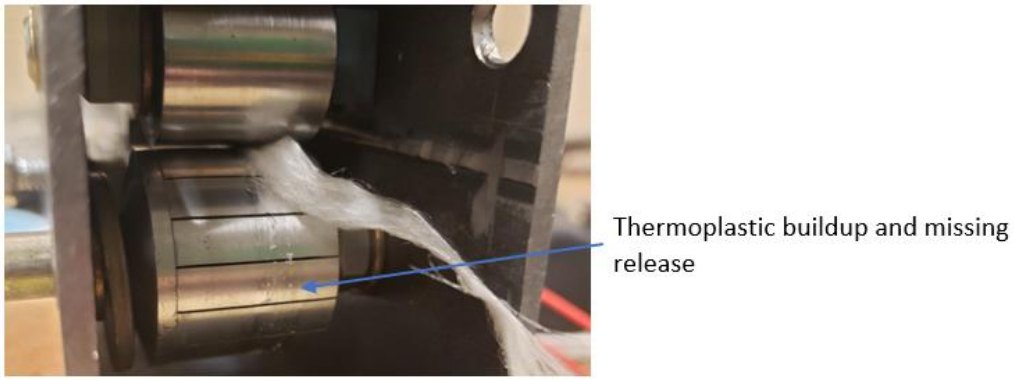

Figure 24: Refeed testing using released rollers.

An additional issue with this system was the use of the steel anvil roller. The blade used with the chopper gun blade was hard enough that the blade would chip after the first cut. The damage on the chopper gun blade can be seen in figure 25. After a limited number of cuts, the blade would fracture due to brittleness of the steel blade. Due to the issues with the heated refeeding and steel anvil roller, testing with the cut and refeed of the cold tow using a polyurethane anvil roller began.

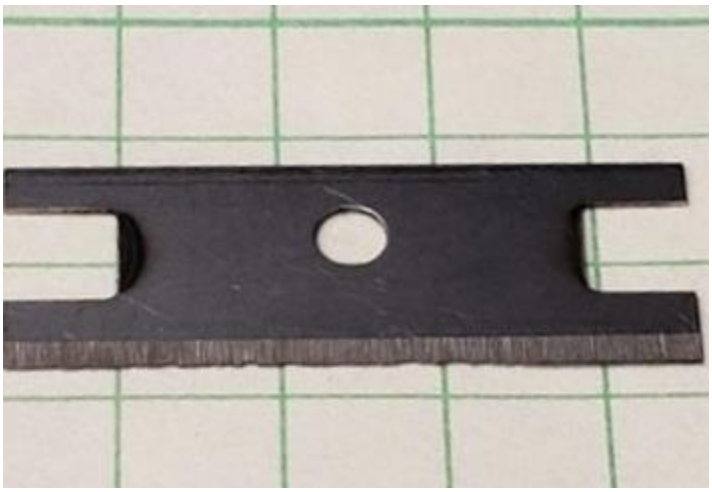

Figure 25: Damaged chopper gun blade.

2.2.2 Commingle Tow Material Changes and Issues

All previous testing had been done with a glass/PET commingled tow with an unprocessed fiber volume fraction of 55%. Cut and refeed testing with cold tow continued with the glass/PET tow and was very successful; the tow would consistently be cut and fed forward using this feedstock. When the material was changed to a glass/PP commingled tow, the fibers would not completely sever during the cutting. The glass/PP feedstock had a lower fiber volume fraction of 35%. This lower fiber volume fraction meant that the brittle glass fibers could not be sufficiently bent to cause severing. The solution was to increase the durometer of the anvil roller from 80A to 90A. With this change, the glass fibers were forced to conform around the blade, increasing the amount the fibers were bent; this then caused the fibers to bend and break consistently.

2.3 Heating/Deposition

With the cutting system developed, the rest of the system needed to be designed. While non-contact heating method have been developed for AFP processes, many were not appropriate for the application. Hot gas is inexpensive but inadvertently heat the whole head due to the wash of the hot air. Lasers are appealing but difficult to use with glass fiber reinforcement; the heating method should not limit the

feedstock usable with the system. Heating using an infrared array is the most appealing method of noncontact heating. However, an infrared heater that is small enough for heating a single tow was not found. Heating the roller seemed like a low-cost solution that also heated the tow at the nip. As a result, testing of heated roller deposition needed to be done. One of the current fiber printers was modified to accommodate a heated roller. The roller was heated using a 40W cartridge heater inside of the roller shaft. A DF Robot SEN 0256 IR thermometer was used to measure the temperature of the roller, a solid-state relay was used to change the power going to the heater and an Arduino Uno Rev3 was used to control the roller temperature. This testing was successful and proved that the tow would tack hands free. The test setup can be seen in figure 26.

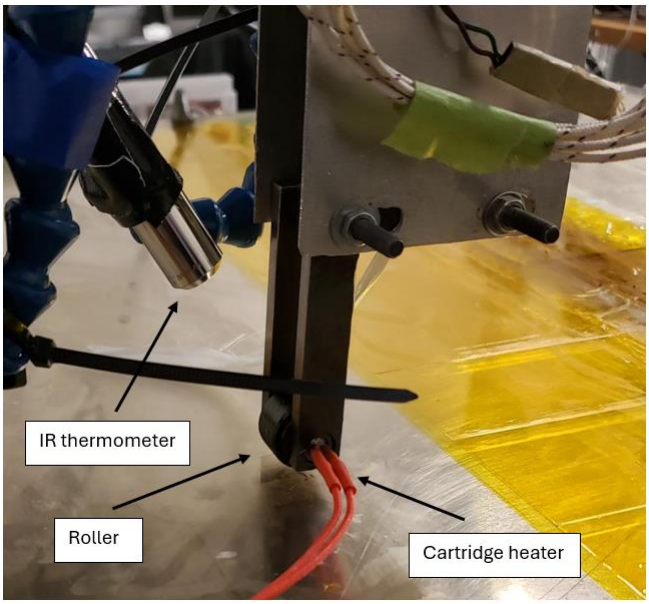

Figure 26: Test setup for heated roller deposition.

Additionally, the tow would wet out to some degree using this method; this was a qualitative observation as no burn-off testing on the samples was done. Performing the burn-off testing would give an overview of the constituent material content, such as the overall void and fiber volume fractions. With this method of deposition validated for an automated way of manufacturing samples, further development of the system proceeded.

While the use of a heated roller was validated, the roller still needed to be incorporated in the rest of the design. One eventual goal of this project was to have feedback control of the roller or deposition head as a whole. While feeding a signal back to the robotic arm was theoretically possible, actuating the roller would allow for greater precision of the roller height. A linear stepper motor was selected as the method of actuation as it provided a high force output and good resolution. A NEMA 34 linear stepper with a 0.0005” travel per step and a max force output of 500lbs was selected as the stepper as it had been used previously on a project at the lab but was not currently being used. The heated roller could be directly attached to the linear stepper. This is depicted in figure 27.

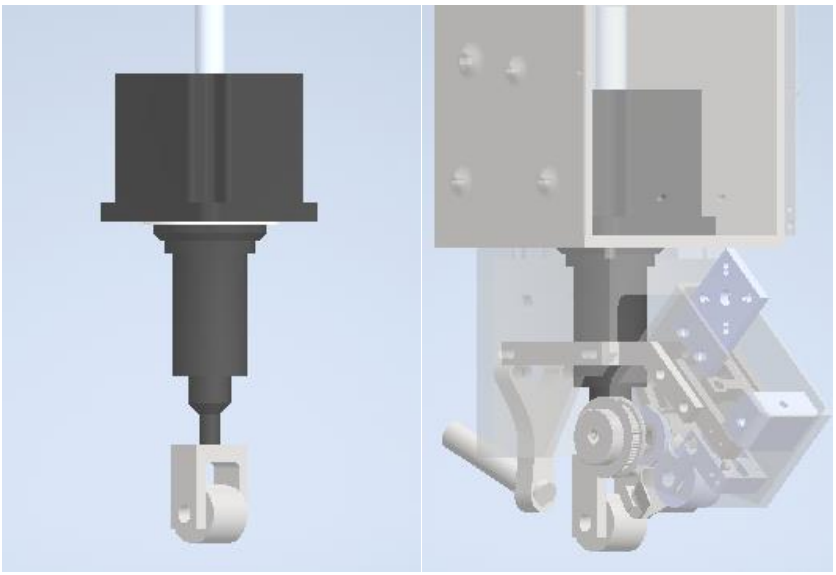

Figure 27: Attachment of roller assembly onto stepper motor isolated (left) and in the assembly (right).

The roller used in this work was a 31.8 mm (1.25”) diameter, steel roller with two internal plain bearings. Through the center of the roller is a hollow shaft that accepts two 40W cartridge heaters. Initially, the temperature of the roller was monitored by the same DF Robot SEN 0256 IR thermometer and controlled by the same Arduino Uno Rev3 used previously. Eventually, the IR thermometer was switched to an Optris CSLT as this sensor had a higher upper sensing temperature of 1030C vs. 270C for the DF Robot, further it had a programmable sensing emissivity, and could interfaced as either a digital or K-type thermocouple. The last feature was not used in this current work but does provide an easy path for

further integration of the system into a global controller (i.e. LabVIEW). The head can be seen in figure 28 displaying the relative locations of the cut and refeed system, the linear stepper and the heated roller.

On initial testing, the roller performed as expected. After some further use, the roller did not roll during deposition and just slide along the top of the tow. The roller was able to freely spin but the friction between the roller and the tow was less than the friction between the bearings and the shaft. The lack of friction was due to the molten plastic. While not intended, it is not clear how much this impacts functionality.

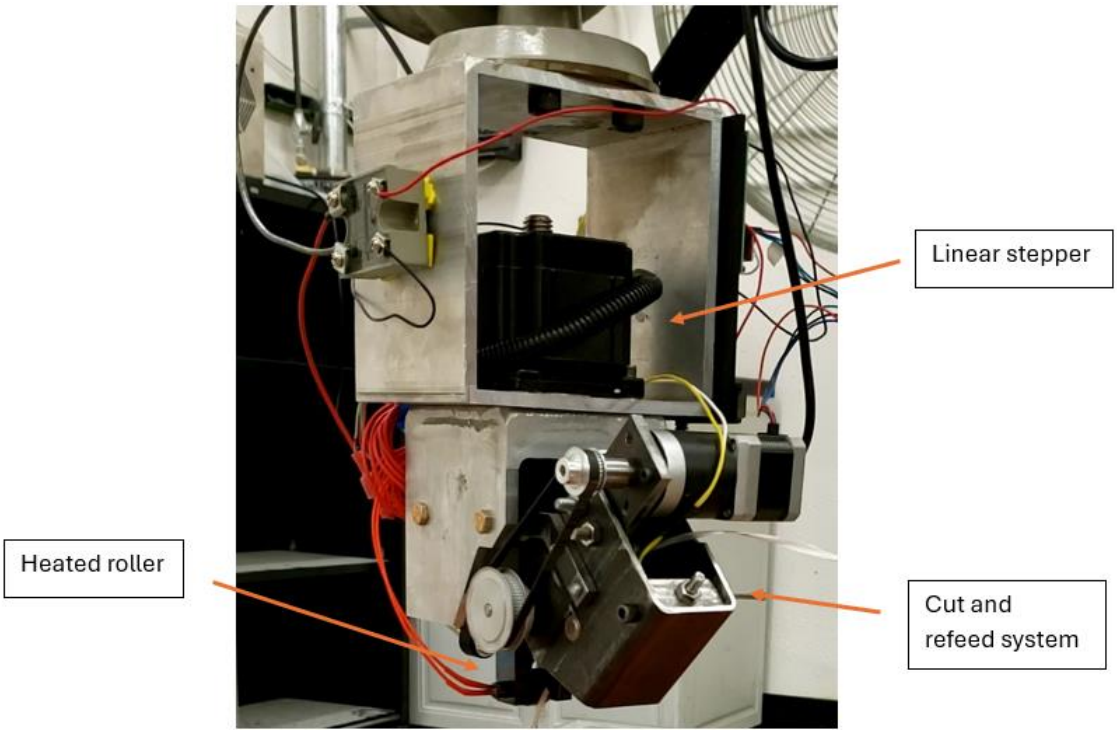

Figure 28: Deposition head.

2.4 Force Based Feedback

To sense the force, four CALT 30kg tension-compression S-type load cells were selected. Additionally, an HX711 load cell amplifier was used to interface the load cells with the controller, an additional Arduino. These load cells were wired in parallel to effectively sum the output voltages and had a max capacity of 120kg. This allows the load cells to be configured in a square pattern while still reading the applied load

correctly. With the load cells wired and configure like this, the summing of the circuit minimizes the impact of bending moments. The installed load cells can be seen in figure 29. Additionally, the load cells are not directly attached to the sixth axis but instead to an aluminum mating plate. This is advantageous as it makes the design more universal; if the end effector needs to be attached to a robot with a different bolt pattern, the only part that has to be manufactured is the mounting plate.

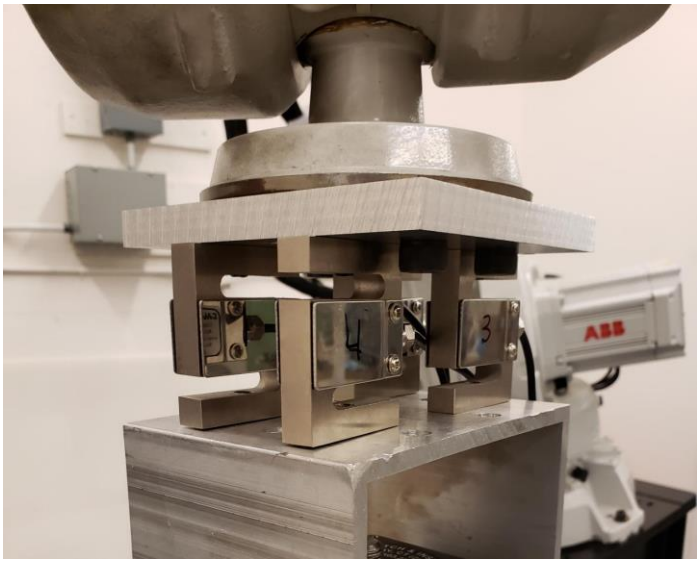

Figure 29: Installed load cells.

2.5 Other Design Considerations

To facilitate the tow moving under the roller during refeed, a simple guide was used. This not only helps to guide the tow under the roller, but also to keep the tow centered under the roller during deposition. Initially the guide had a funnel shape, but this caused the tow to bend and buckle during refeed. This bending caused the tow to get jammed in the guide, preventing refeed. The solution to this was to remove the bottom half of the guide; this allowed the tow to deform when the severed end contacted the wall of the guide without coiling up and jamming the guide. This issue can be seen in figure 30 and the revised guide design can be seen in figure 31 (a) and (b).

Figure 30: Tow guide bunching during refeed.

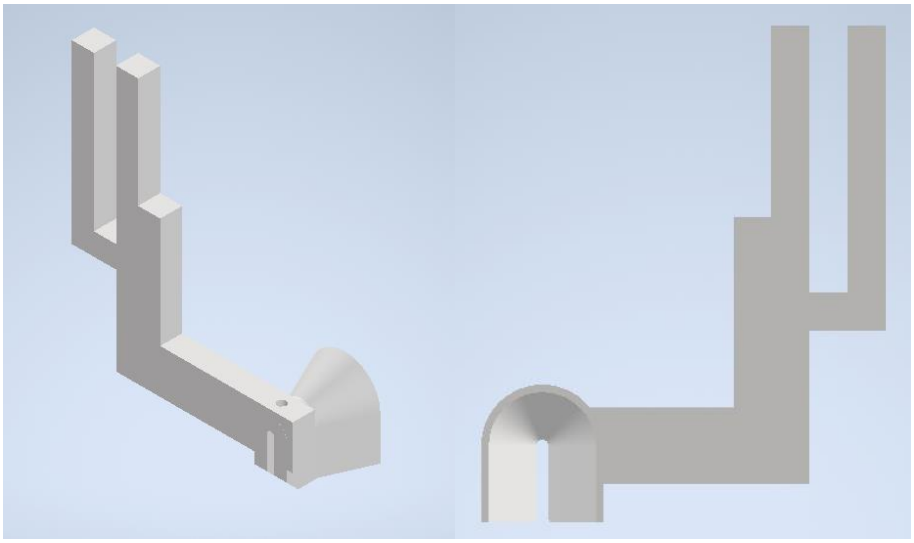

Figure 31: Isometric (left) and back (right) views of the current guide design.

2.6 Design Summary

The culmination of this design is an end effector that can be mounted on a variety of robotic systems with a minimal amount of retooling. This end effector can additively manufacture continuous fiber composites utilizing commingled tow as feedstock. Additionally, this system is capable of automated manufacture of these composites but using discrete pathing. The ability to make discretely pathed parts is due to a cut and refeed system developed utilizing a bladed roller with a cam to not only cut the tow

but to also feed it forward with a single mechanism. This reduced the complexity of the cut and refeed system while maintaining functionality. Changing the style of deposition from a nozzle to a roller made this refeed system possible. Finally, the end effector is capable of manufacturing parts using force feedback control. This is possible due to the implementation of load cells onto the head and a linear stepper motor that controls the z position of the deposition roller.

CHAPTER 3: SYSTEM COMPARISON

This study investigates the quality of grid stiffeners produced using a 6-axis robot mounted roller consolidation end effector to previous grid stiffeners, and grid stiffener intersections, manufactured using a gantry mounted baseline nozzle consolidation process. In order to facilitate an effective comparison between the two cases, the geometry of the part was designed and characterized such that the stacking sequence of the grid at the intersection was $[(0/90)_{20}]$ and the number of tows placed are the same between the two systems. The placement systems were utilized to each generate two samples. One sample was printed at a deposition rate of 50mm/min, while the other was printed at 300mm/min. These speeds were chosen based on experience with rates used successfully with the nozzle-based system and are lower than the maximum speeds of the robot mounted roller consolidation system. All of the sample manufacturing and preparation for the nozzle-based system was done by S. Tanu, a PhD student and collaborator at CSU's CMMS Laboratory. The analysis of the results of both systems and the subsequent discussion was also done in collaboration with S. Tanu.

3.1 Materials

The commingled tow feedstock used in this study is Compofil PP-60-R-1870N (Fiberglass Industries Twintex), a continuous E-glass/Polypropylene (EG/PP) untwisted commingled tow. The Tex of the roving is 1870. The unprocessed weight fraction of the reinforcement is 60%, which corresponds to a 35% fiber volume fraction. Warlick et al., used the same material and reported the glass transition temperature of the PP polymer in the commingled tow to be below 0C and the main melting peak, via differential scanning calorimetry (DSC), at a temperature of 163.8C (327F) [44]. The processing temperature for the heated zone of each end effector is set to a fixed, predetermined, 250C based on prior processing experience. A low-tack adhesive backed PP tape was placed on top of the glass build plate to improve

the bed adhesion of the commingled tow and to maintain the as-printed position on the substrate. The unprocessed commingled tow width is approximately 6mm.

3.2 System Overview

3.2.1 Nozzle Consolidation Fiber Deposition System

A custom gantry-based fiber deposition system was purpose-built to manufacture complex geometries and high fiber volume fraction structures, as shown in figure 32(a). This system has two print heads - one for the placement of conventional thermoplastic 3D printing filament and the other for the processing of continuous fiber reinforced composite materials in a manner similar to pultrusion, allowing the commingled tow to be pulled through a short, heated zone and custom designed nozzle. This work will make use of only the continuous fiber print head, as shown in figure 32(b).

The additional components added to the common FFF (Fused Filament Fabrication) hot end used as the basis for the continuous fiber processing print head consist of a custom fiber placement nozzle, cooling manifold, and spring-loaded consolidation system. A brass nozzle of 1.5mm (0.059”) inside diameter and 7 mm (0.276”) outside diameter, shown in figure 32(b), was designed to allow for a single tow of commingled material to be compacted as it is being pulled through the nozzle, and then consolidated between the nozzle face and the previous surface. The outside diameter of the face of the nozzle is manufactured to be greater than the width of the spread commingled tow. For this nozzle-based process, the tow is shaped as it moves through the nozzle, to approximately the nozzle dimensions, and is then spread under the nozzle face. This results in a processed tow width narrower than that of the original 6mm tow. A cooling manifold is attached to the end effector with two adjustable ducts for computer-controlled compressed air flow to locally cool and rapidly rigidize the newly placed composite. Warlick et al. developed this cooling system to increase positional fidelity when tow shearing of continuous fiber reinforced thermoplastic composite (CFRTC), using EG/PP, was implemented to enable

enhanced tow steering [44]. By switching the cooling air on and off for localized cooling, this feature provides advantages of enhanced tow spreading and consolidation during programmed manufacture.

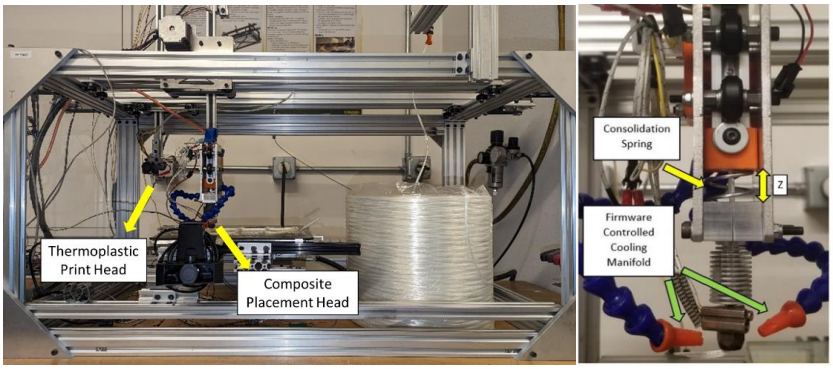

Figure 32: Gantry fiber deposition system setup (left) and composite placement head (right) [50].

In order to improve consolidation quality and uniformity over surface variations and to eliminate voids, Rodriguez et al. [45] included a spring-loaded system which supports the nozzle. This spring-loaded end effector has a spring constant of approximately 7.5 N/mm which results in the application of a repeatable consolidation force on the placed tows. The amount of force applied is controlled by positioning the nozzle in the build direction (Z axis) at a height above the previous position such that a known amount of spring compression is introduced. To reduce the thickness of the composite tow and increase the tow width, it is possible to program a negative height value in relation to the build plate which results in a greater spring displacement and a correspondingly greater force. This enables the nozzle to exert pressure on the build plate, or on previously positioned tows, and spread the tows being currently placed. Load cells in the dual gantry system, supporting the build plate, are available to monitor the resultant consolidation force while continuous fiber placement is underway.

3.2.2 Sample Preparation for Nozzle-Based System

To manufacture grid stiffeners and grid intersections, a similar approach to that described by Hogan et al. was used to generate a continuous print path incorporating loops outside the basic stiffener profile [50]. The benefit of this approach is that it avoids the need to manually cut and restart the fibers after each

layer is printed as was the case for the demonstration intersection shown in figure 15. This is convenient as multilayer grid stiffener specimens can take many hours to produce and the use of a continuous path removes the need for operator intervention. The deposition path program and toolpaths were defined using CAD software. Once the coordinates of the first layer are generated within the software, the X and Y coordinates are transferred to Fullcontrol Gcode Designer [66] to generate the points for the subsequent layers of the part without having to manually change the Z position for every layer. The layer height, or Z step, was set to a predetermined 0.3mm. The consolidation of the layers is controlled by controlling the Z position of the gantry system. The initial Z position of the system is set by reading a force output from load cells installed under the build plate. The value for these tests was set to 11N, enabling the initial layer to effectively tack to the build plate. With a goal of a uniform grid height at the intersections, even with the local doubling of fiber count, the consolidation force, at the crossover region, the Z step was programmed to a value consistent with a 22N force. The higher consolidation force at the grid intersections allows for the tows to spread out, thus reducing the individual layer thickness, as depicted in figure 33.

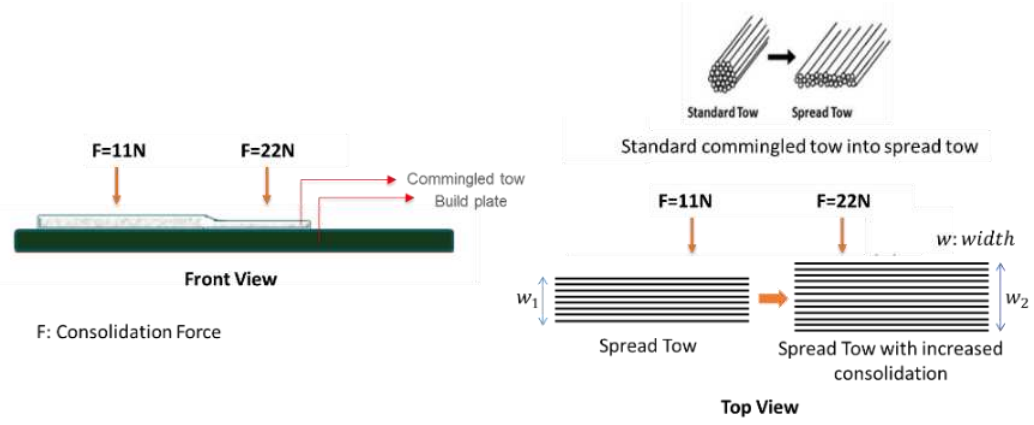

Figure 33: Image of spread of commingled yarn: Front view (left) and top view (right) [48].

The specific continuous tool path used to create the reinforcing grids for the samples of this work is shown in figure 34. Only the straight regions adjacent to the 3 intersections and the intersections themselves are used in this effort.

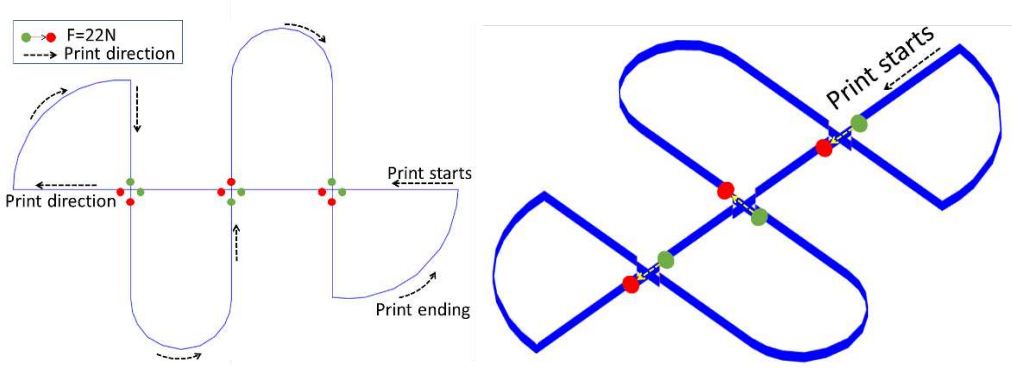

Figure 34: Continuous print path planning on single layer (left) and 20 layers generated using Full control Gcode Designer (right).

3.2.3 Roller Consolidation Fiber Deposition System

Due to the limitations of the gantry-mounted nozzle consolidation fiber deposition system in terms of speed and the required manual starting/stopping, a new continuous fiber deposition head was designed to be integrated with an ABB IRB4600 6-axis robot. The new deposition head includes a heated roller and a cut and refeed system to increase the deposition rate and to automate the stopping and starting of the composite placement, negating the need for the continuous paths described for the nozzle consolidation system.

The roller consolidation system consists of a 31.8 mm (1.25”) diameter, heated steel roller with two internal plain bearings. Through the center of the roller is a hollow shaft that accepts two 40W cartridge heaters. An infrared (IR) thermometer, DF Robot SEN 0256, is used to sense the temperature of the roller consolidation surface and enable temperature control using an Arduino Uno Rev 3 operating through a solid-state relay. The system is shown in figure 35(a). The cut and refeed subsystem consists of a spring actuated anvil roller, a driven cutting roller, similar to that used in a composite chopper gun, a cam, and a roller follower. Portions of the cut and refeed system can be seen in figure 35(b). This cut and refeed system, in concept, allows the tow to be cut while the placement head is still in motion; however, in practice, the system motion rate is reduced during the cut and refeed process.

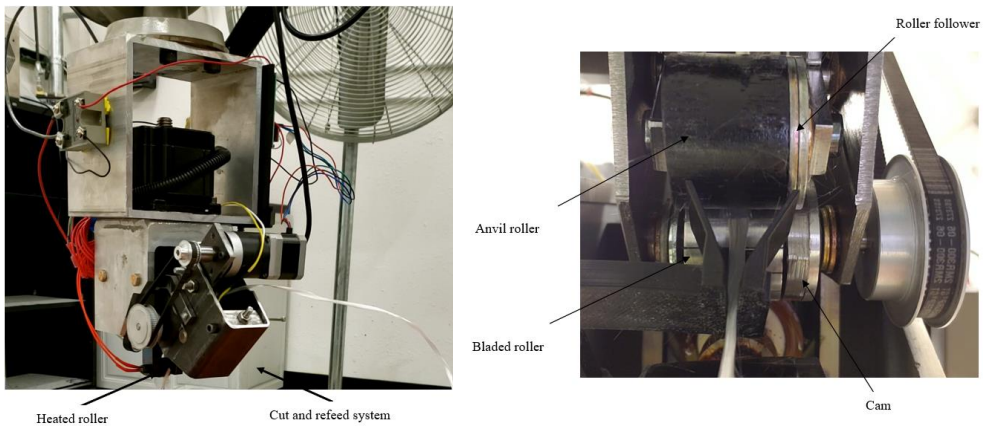

Figure 35: The deposition head (left) and cut and refeed system (right).

Differences between the gantry deposition and robotic deposition include the method of consolidation, ability to automatically cut and refeed, stiffness of each system and load monitoring. The gantry system uses a heated nozzle to initially form the tow into a cylindrical cross section and then presses the shaped tow into a rectangular "tape". Further, the gantry system has no ability to automatically cut and refeed the fibers; all stopping and starting is a manual process. The gantry system does have a spring integrated into the nozzle, enabling a more consistent application of the consolidation force and less affect from deviations in the bed flatness and levelness. Finally, the gantry system has load cells supporting the print bed, enabling load monitoring during printing. The robotic system deposits the tow using a heated roller and the commingled feedstock is introduced in the original form and is directly deposited as a "tape". This results in a greater placed tow width than the nozzle consolidation system, for a given consolidation force. The robotic deposition system has no spring integrated into the system, yielding a stiffer system and less tolerance for bed variations from level. Finally, this research was performed before force monitoring and feedback capabilities were implemented in the robotic system.

3.2.4 Sample Preparation for the Roller-Based System

The samples, using the robot, were printed on a sheet of glass secured to a stationary turntable. The roller temperature was set at 250C in an attempt to match the parameter used in the nozzle-based process, and the layer height was set at 0.15mm. The reduced layer height, compared to the nozzle-

based system, is necessitated by the difference in tow geometry prior to consolidation. For the crossover, the robot displaces an additional -0.1mm in the Z direction to increase consolidation force and, as a result, spread and thin the tow. The layer height is 0.15mm and the tow would need to thin half a layer height to get a uniform thickness across the crossover. If the end effector/robot arm were infinitely rigid, this would be a z step of -0.075mm. Some additional displacement was added as the system isn't infinitely rigid. The print speed was set to 300 mm/min for one sample and 50 mm/min for the second sample, matching the placement speeds of the nozzle-based system. Both samples had 20 layers in the beam sections and 40 layers at the crossovers.

To program the print path for the ABB robot, the centerlines of each single layer were created in CAD and were then exported to a commercial robot simulation software. The path was aligned with the X and Y axes to make the code more intuitive and easier to read. To find the correct User and WorkObject coordinate systems, the robot was manually jogged to the start/stop locations of the X and Y paths and the crossover point. At each of these points, the robot was jogged along the Z axis until the roller was in slight contact with a piece of 0.10mm (0.004") shim stock; the height was then recorded, and the coordinate system was reoriented accordingly to account for build plate variations from level. Due to variations in the levelness of the print bed, some manipulation of the print path was needed as compensation. This manipulation is summarized in table 1. The same compensation was applied to, and verified for, all three paths in the Y direction. A "FOR" loop was then used to step the robot through the print path, in a layer-wise fashion.

Table 1: Z Height Compensation in the Print Paths

	Z height (mm)			Z height (mm)
Xstart	0.2		Ystart	0.3
Crossover	0		Crossover	0
Xstop	0.2		Ystop	0.1

3.3 Specimen Evaluation Procedures

The four samples were evaluated for thickness variations, both within the straight grid stiffeners and at the crossovers and were then sectioned to enable local fiber and void fraction determination.

3.3.1 Geometry Measurement Procedure

The quality of the fabricated parts was investigated by measuring the variation in the 20 layer height over the length of the straight beam (X, Y1, Y2 and Y3) sections as well as in the 40 layer crossovers (C1, C2 and C3), as shown in figure 36. The geometry of each specimen was measured 3 times at the same location, using a micrometer prior to sectioning.

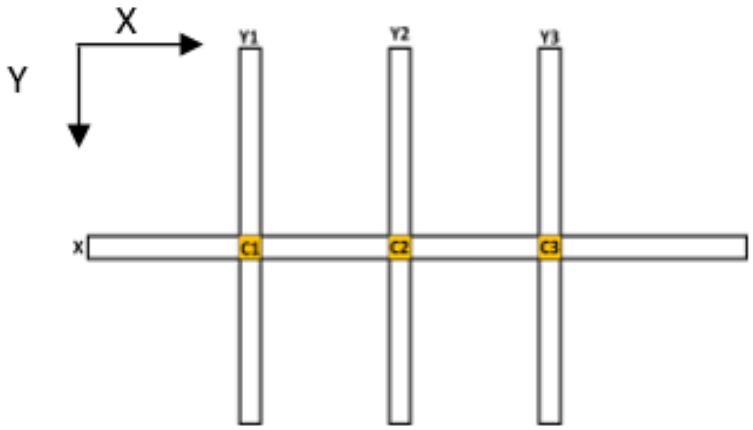

Figure 36: Image of sample and labeling. From left to right: Y1, Y2, and Y3.

Samples from each manufacturing system are shown in figure 37. The differences outside the areas to be analyzed are clear, with the full continuous path shown in figure 37(a) and the discrete path, which is the result of the added cut and refeed capabilities, in figure 37(b).

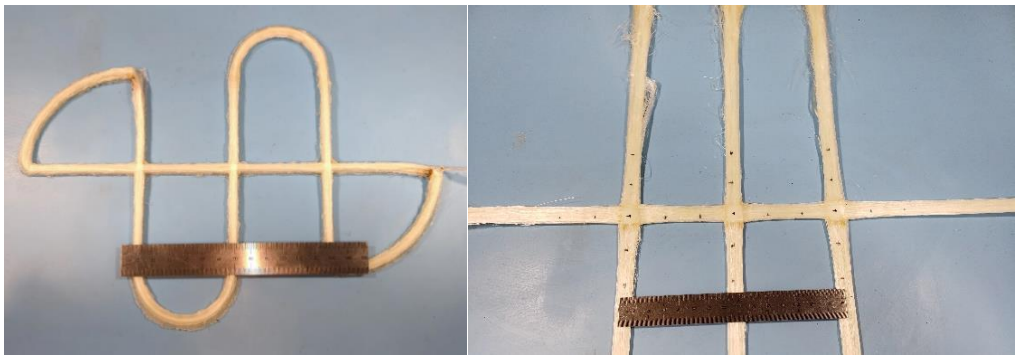

Figure 37: Examples of samples printed at 300mm/min using, the gantry-based nozzle consolidation system (left) and the robot-mounted roller consolidation system (right).

Also apparent is the difference in beam width of the two 20 layer specimens at the same 300mm/minute deposition speed. Since the amount of fiber positioned by the two systems, in each layer, is identical, the greater width shown in figure 37(b) is consistent with a smaller layer thickness. Specifically, the thicknesses were evaluated at the positions indicated by the black dots visible in figure 37(b), corresponding to the three straight beams and crossovers labeled in figure 36.

3.3.2 Volume Fraction Determination

To prepare the specimens for quality evaluation, a water-cooled diamond saw was used to section the crossover regions from the grid stiffener beams produced by both placement systems. The sectioning was done at least 10mm from the crossover region, and the straight beam specimens were cut to a length of 25mm. This sectioning of the specimens is shown, for one of the roller consolidated specimens, in figure 38. To ensure consistency between specimens generated via the nozzle and roller deposition heads, 10 straight beams and 3 crossover specimens were prepared from each sample. No post-processing was performed on the samples in an attempt preserve the as-printed properties. The quality of the composite stiffener beams was analyzed by determination of the fiber volume fraction and the void volume fraction of both the straight beam and crossover specimens.

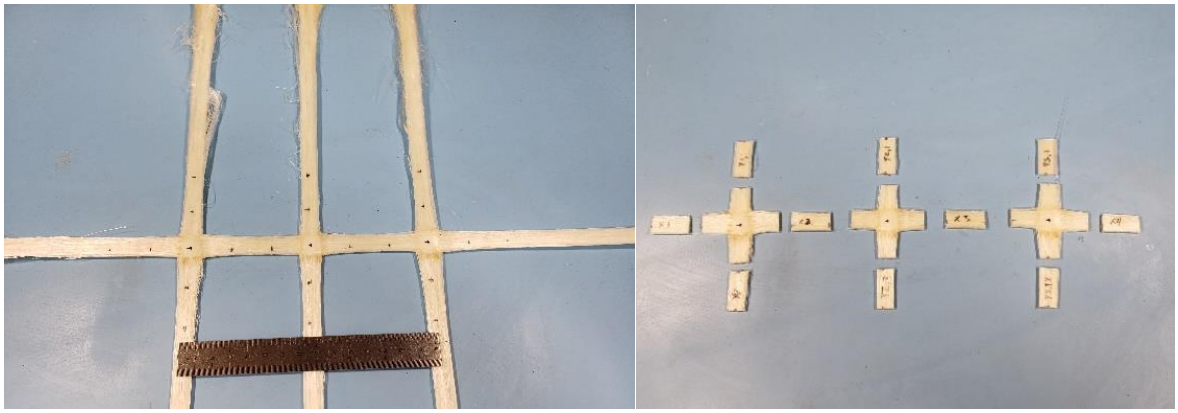

Figure 38: Examples of a roller consolidated, 3 crossover sample before cutting (left) and, the associated specimens after cutting in preparation for volume fraction analysis (right).

To determine the void volume fraction of a specimen, the Archimedes principle was used to find the density. To determine the volume of each specimen, the fluid displacement method, based on ASTM 792, was used [67]. RedLine Water Wetter was used, in a ratio of 32:1 deionized (DI) water to RedLine,Water Wetter in order to minimize the bubble formation on the specimens and thus improve the accuracy of the measurement. To determine the weight fraction of fibers in each specimen, the matrix burn-off method was performed, according to ASTM D3171-15 [68]. To perform the matrix burn-off method, the specimens are first placed in a ceramic crucible and dried at 70C in an oven with desiccant for an hour to reach equilibrium. Then, the specimens are put in the furnace, in air, and the temperature is set to 596°C for at least 4 hours to ensure complete removal of the matrix. The loose fibers are then weighed, allowing determination of both fiber and void volume fractions through the use of manufacturer supplied densities.

3.4 RESULTS

3.4.1 Geometry Measurements: Gantry Deposition

The variation in grid thickness over the length of the grid stiffeners and at the crossovers for the gantry deposition is given in table 2.

Table 2: Summary of Thickness Measurements for the Gantry Deposition.

	X					
		X Avg. (mm)	% Standard Deviation	Crossover Average (mm)	% Crossover Deviation	% Programmed Deviation
Speed (mm/min)	300	5.686	5.00%	6.276	10.37%	-5.23%
	50	4.366	0.88%	4.794	9.81%	-27.23%
	Y1					
		Y1 Avg. (mm)	% Standard Deviation	C1 (mm)	% Crossover Deviation	% Programmed Deviation
Speed (mm/min)	300	5.761	5.21%	6.254	8.57%	-3.99%
	50	4.509	0.72%	4.772	5.82%	-24.85%
	Y2					
		Y2 Avg. (mm)	% Standard Deviation	C2 (mm)	% Crossover Deviation	% Programmed Deviation
Speed (mm/min)	300	5.457	5.50%	6.242	14.39%	-9.05%
	50	4.267	1.91%	4.769	11.78%	-28.89%
	Y3					

		Y3 Avg. (mm)	% Standard Deviation	C3 (mm)	% Crossover Deviation	% Programmed Deviation
Speed (mm/min)	300	5.628	4.88%	6.331	12.48%	-6.19%
	50	4.442	1.03%	4.842	9.02%	-25.98%

A comparison of the beams and crossovers, using % Crossover Deviation and % Programmed Deviation data, calculated from the thickness data, is also included in the tabulated data. The % Crossover Deviation is the comparison of the straight beam section thickness to the crossover thickness. The % Programmed Deviation measures the difference between the average beam thickness and the programmed thickness of 6 mm, based on 20 layers, each with a layer height of 0.3mm. From table 2, it is observed that sample printed at 300 mm/min consistently shows a higher crossover thickness deviation than the sample printed at 50 mm/min. The average standard deviation of the beam thicknesses for the 300 mm/minute sample is 4 times higher than that of the sample printed at 50 mm/min. The increase in the standard deviation is likely caused by more limited matrix flow at the higher feed-rate. It is known that feed rate is related to the heat input to the tow as it determines the amount of time the commingled tow spends in the heated zone. Both samples are printed at the same nozzle temperature, 250C, and the feed rate is the only controlled parameter that changes between the two placement speeds. Therefore, printing at a higher feed rate (6 times greater in speed in this case) means the commingled tow spends less time in the hot zone compared to sample printed at 50 mm/min. The higher placement speed not only reduces the actual tow temperature leaving the nozzle, resulting in a higher matrix viscosity, resisting flow, but also the duration of time the tow is under the nozzle is reduced, allowing less time for the matrix to flow under consolidation pressure and increase the width of the tow at the crossover. Furthermore, when printing in a continuous path and making

sharp angle changes, the tow increases in thickness. At a faster deposition speed, the tow has less time to rigidize, leading to a more significant thickness deviation. As a result, the standard deviation of thickness in the sections printed at 300 mm/min is higher than that in the sections printed at 50 mm/min. This thickness deviation can be seen, graphically, in figure 39.

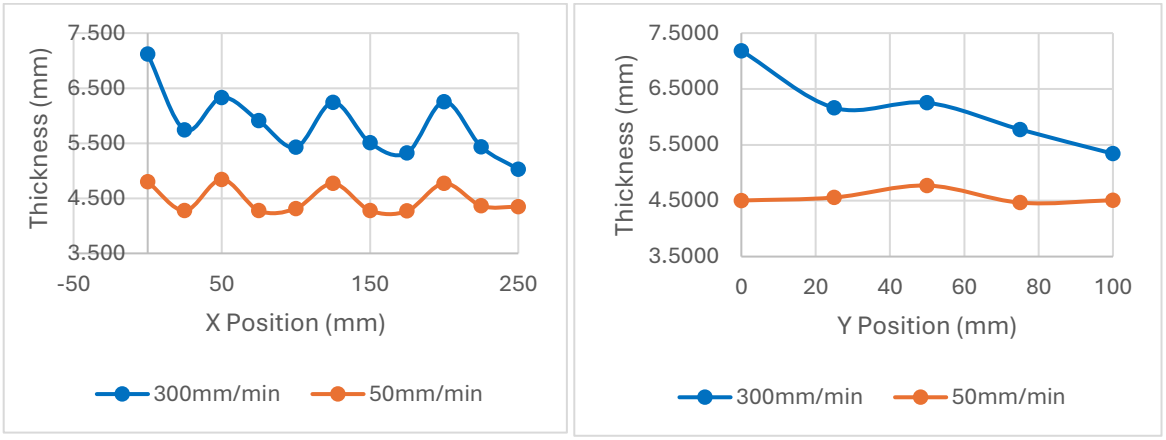

Figure 39: Graphical representation of X thickness variations (left) and representative graph of the Y thickness variation (right) for the gantry system.

The negative values for the % Programmed Deviation are due to the consolidation provided by the initial compression of the spring. The slower print speed allows the tow to spread more, allowing the spring to extend further and results in a greater deviation from the programmed height.

3.4.2 Geometry Measurements: Robotic Deposition

Thickness measurements of the roller consolidated specimens are summarized in table 3. Table 3 displays the average thickness of four beams (X, Y1, Y2, and Y3) and a comparison with the corresponding crossover values (C1, C2, and C3). The X-direction beam is compared with the average of the three crossovers as it is part of all three crossovers. To calculate the % Programmed Deviation, a programmed thickness of 3 mm was used.

Table 3: Summary of Thickness Measurements for Robotic Deposition.

	X

		X Avg. (mm)	% Standard Deviation	Crossover Average (mm)	% Crossover Deviation	% Programmed Deviation
Speed (mm/min)	300	3.318	2.30%	3.482	4.93%	10.61%
	50	3.232	1.65%	3.182	-1.55%	7.73%
	Y1					
		Y1 Avg. (mm)	% Standard Deviation	C1 (mm)	% Crossover Deviation	% Programmed Deviation
Speed (mm/min)	300	3.197	3.82%	3.453	8.01%	6.56%
	50	3.162	4.22%	3.096	-2.08%	5.40%
	Y2					
		Y2 Avg. (mm)	% Standard Deviation	C2 (mm)	% Crossover Deviation	% Programmed Deviation
Speed (mm/min)	300	3.273	1.94%	3.517	7.45%	9.11%
	50	3.253	2.50%	3.214	-1.22%	8.45%
	Y3					
		Y3 Avg. (mm)	% Standard Deviation	C3 (mm)	% Crossover Deviation	% Programmed Deviation
Speed (mm/min)	300	3.272	1.97%	3.476	6.22%	9.08%
	50	3.227	1.92%	3.235	0.26%	7.56%

In general, the slower speed results in significantly better geometric control in the crossovers than the faster speed. This is not surprising as the matrix has more time to flow while under the pressure of the consolidation roller. Further, the matrix experiences the heat of the consolidation roller for longer, allowing more heat to transfer into the matrix. This, in turn, lowers the viscosity of the matrix, allowing more flow to take place. The thickness of the X-direction beams and of the crossovers is depicted in figure 40 and a clear trend is apparent. The sample printed at 300 mm/min has local thickness maximums at the crossover points, whereas the sample printed at 50 mm/min has local minimums at the crossover points. This is due to additional tow spreading, consistent with a longer time under the heated roller.

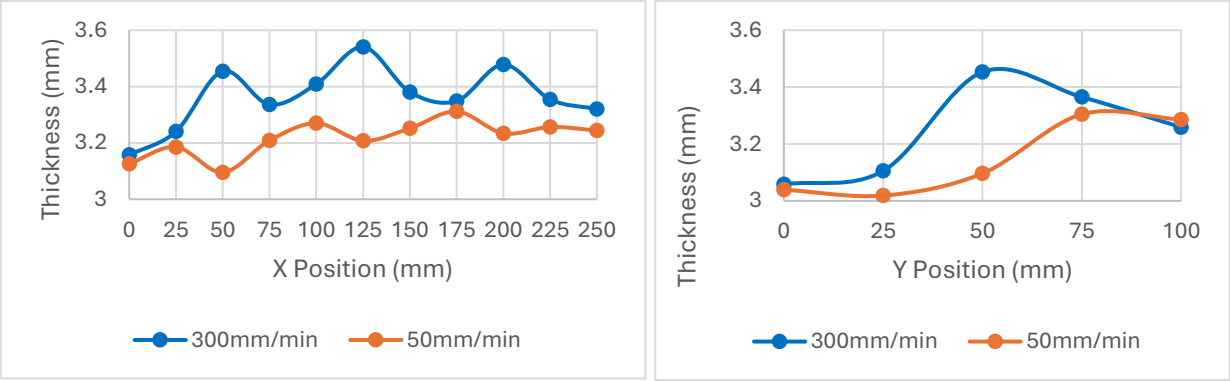

Figure 40: Graphical representation of X thickness variations (left) and representative graph of the Y thickness variation (right) for the robotic system.

One trend for the robotic deposition system is the general increase in thickness with an increase in position for both X and Y, as shown in figure 40. An explanation is related to imperfect bed leveling and height compensation.

3.4.3 Volume Fraction Analysis: Gantry Deposition

The fiber and void fractions of the gantry deposition system are summarized in table 4. As previously stated, the unprocessed commingled EG/PP tow contains 35% fiber volume fraction. The crossover specimens have a higher fiber volume fraction compared to that of the beam specimens. It is

particularly evident in the case of the sample printed at a speed of 50 mm/min, which exhibits superior quality, with a fiber volume fraction of 45.5% and void fraction of 7.12%. This is primarily due to the doubling of fiber in the crossover regions, which results in a greater amount of fiber being packed into a given laminate volume.

In Section 3.1.1, the geometry analysis revealed that the sample printed at a speed of 300 mm/min had lower geometric fidelity than the one printed at 50 mm/min. For the sample printed at a higher speed, the tow spent less time in the heated zone of the nozzle and under the consolidation face, limiting the heat into the tow and the resultant flow and subsequent spreading. Consequently, there is less time for flattening the tow and voids are not squeezed out of the laminate effectively. This leads to the accumulation of voids within the laminate due to the entrapment of air and moisture, resulting in a higher void volume fraction for sample printed at 300 mm/min.

Table 4: Average Fiber and Void Fraction Determined at Crossovers, X and Y Positions (Gantry).

		X		Y1		Y2		Y3		Beam		Crossover	
		Ave (%)	SD (%)	Ave (%)	SD (%)	Ave (%)	SD (%)	Ave (%)	SD (%)	Ave (%)	SD (%)	Ave (%)	SD (%)
300mm/min	V_f	32.48	0.53	31.22	0.96	31.83	0.64	33.11	0.56	32.16	0.67	36.07	0.69
	V_v	7.53	0.28	13.58	2.10	7.04	0.52	5.62	0.43	8.44	0.58	13.58	0.87
50mm/min	V_f	35.26	0.79	34.42	0.68	36.03	0.54	34.35	0.62	35.01	0.66	45.51	0.66

	V_v	3.11	0.63	5.42	0.37	2.40	0.39	2.93	0.45	3.46	0.46	7.12	0.46

3.4.4 Volume Fraction Analysis: Robotic Deposition

The fiber and void volume fractions for the robotic fiber head and roller consolidation are summarized in table 5.

Table 5: Average Fiber and Void Fraction Determined at Crossovers, X and Y Positions (Robot).

		X		Y1		Y2		Y3		Beam		Crossover	
		Ave (%)	SD (%)	Ave (%)	SD (%)	Ave (%)	SD (%)	Ave (%)	SD (%)	Ave (%)	SD (%)	Ave (%)	SD (%)
300mm/min	V_f	33.63	0.16	33.94	0.11	34.47	0.38	34.00	0.21	33.93	0.38	34.32	0.25
	V_v	5.02	0.34	5.13	0.32	4.22	0.40	4.95	0.29	4.87	0.48	9.21	0.27
50mm/min	V_f	35.91	0.73	35.94	0.46	36.23	0.57	36.48	0.50	36.09	0.65	39.96	0.29
	V_v	2.51	0.55	2.75	0.26	2.25	0.16	2.59	0.23	2.52	0.42	5.89	0.14

The overall results of the fiber and void fraction analysis for the roller consolidation system are promising. For the sample printed at 300 mm/min, the average fiber volume fraction of all the beam sections is approximately 34% and a void volume fraction is below 5%. The crossover sections of this sample show poor consolidation, with only a 34.32% fiber volume fraction and a 9.21% void fraction. For the sample printed at 50 mm/min, the average fiber volume fraction of the beam sections is slightly above 36% with a void volume fraction of just greater than 2.5%. The quality of the crossover sections of

this sample was an improvement over that of the higher speed sample, with a fiber volume fraction of 39.96% and a void content of 5.89% by volume.

The most obvious trend is that the fiber volume fraction increased while the void volume fraction decreased when the deposition speed was reduced. This is consistent with additional matrix flow and a longer duration of the applied consolidation. Similar to the reasoning for the crossover geometry being better at the slower speed, the longer time at the elevated temperature resulted in a lower matrix viscosity, improving the flow. Additionally, the slower speed also allows the matrix more time to flow while under the pressure of the consolidation roller. Interestingly, despite the reduced thickness of the Y1 samples, there is no drop in void content for these specimens. The thinner geometry would suggest a higher consolidation pressure on this sample, but there is no obvious influence of this higher pressure on the void content.

3.5 DISCUSSION

3.5.1 Geometry Comparison

The compliance difference of the structures of the two automation systems, as well as variations in the initial shaping of the tow between the two systems caused discrepancies in the produced geometry. When analyzing the samples produced with the gantry system, it was observed that there were significant variations in the % Programmed Deviation for the parts printed at 300 mm/min and for those printed at 50 mm/min. This suggests that there is a noticeable difference between the actual and theoretical thickness of the parts. Based on the information shown in figure 39, it is evident that a greater thickness value is observed at both X and Y positions when at 0 for the gantry system. This is due to the sharp angle, leaving the turn of the continuous path, causing tow buckling, which affects the start of the X and Y beam prints. These findings provide valuable insight into the direct digital continuous fiber deposition process and can inform future improvements.

The compliance, due to the spring-loaded print head in the gantry printer, makes predicting the sample thickness difficult. The stiffness of the robotic deposition system generates a more predictable output geometry, as indicated by the consistency between the standard deviations for each beam at different speeds. However, in both cases, using a Z-position control based on a presumed layer height would require some iteration for the actual thicknesses to match predictions.

The width of the deposited tow is significantly different between the two fiber placement systems. While this was not a parameter that was directly monitored in this study, it is worth discussing. The tow deposited by the gantry system with nozzle consolidation is approximately 50% of the width of the top layer of the tow deposited by roller consolidation using the robotic system. While the tow width is strongly impacted by the applied consolidation force during deposition, the shaping of the deposited tow, prior to consolidation, is different for each system. The gantry deposition system uses a heated zone and a nozzle that initially shapes the flat commingled tow into a cylinder, approximately 1.5 mm diameter, before flattening it under the nozzle. The robotic deposition system heats and consolidates the flat, nominally 6mm wide, commingled tow without any prior shaping, resulting in the wider resultant consolidated tow. Similarly, the amount of tow spreading at the crossovers is another indication of how the initial shaping of the tow impacts the geometry of the final part. The gantry deposition system spreads the 1.5mm cylindrical tow to around 7mm, while the robotic deposition system starts with the flat, unprocessed 6mm tow and spreads it to approximately 12 mm in the straight sections and about 16 mm at the crossovers. The initial shaping of the tow clearly affects the resulting width of the corresponding samples and limits the ability to further thin the tow with the increased consolidation force at the crossovers.

A similar trend was noted for the geometry of the samples, independent of the placement system used. Generally, the slower deposition rate yielded improved crossover geometry, more consistent with the respective beam thickness, as shown in figures 39 and 40. This is due to the matrix having more time to

flow while under the pressure of the nozzle or the consolidation roller. Further, the matrix experiences the heat of the nozzle or consolidation roller for a longer time, allowing more heat transfer into the matrix. This, in turn, lowers the viscosity of the thermoplastic matrix, allowing easier flow to take place. Interestingly, the robotic deposition sample printed at 50 mm/min shows a local minimum at the crossover locations whereas all other samples show a local maximum at the crossover points, as seen in figures 39 and 40. This indicates how the stiffer automation system of the robot, coupled with higher heat in the matrix, can effectively increase the spreading and thinning of the tow.

Both of these systems have demonstrated a capability to generate consistent crossover geometries. The gantry deposition system was able to create a crossover with a maximum thickness increase of 14.38% at 300 mm/min deposition speed. The robotic deposition system was able to create a crossover with a maximum thickness increase of only 8.01% at 300 mm/min deposition rate. Zhao et al. were only able to achieve a minimum height increase of 35% by utilizing the clamp-cut-restart strategy of AFP [30]. Thus, these preliminary results show improved thickness retention over what has been previously reported and does so without the need to cut the continuous fiber at the grid intersections.

3.5.2 Volume Fraction Comparison

Fiber and void volume fractions are summarized in figure 41. In general, both systems follow many of the same trends. Lower void fractions at the slower speed were measured with both systems. The longer time at the elevated temperature lowered the viscosity of the thermoplastic matrix, easing the flow. Additionally, the slower speed also meant that the matrix had more time to flow while under the pressure of the nozzle or consolidation roller enabling higher fiber fractions. Higher fiber and void fractions appeared in the crossovers produced by both systems.

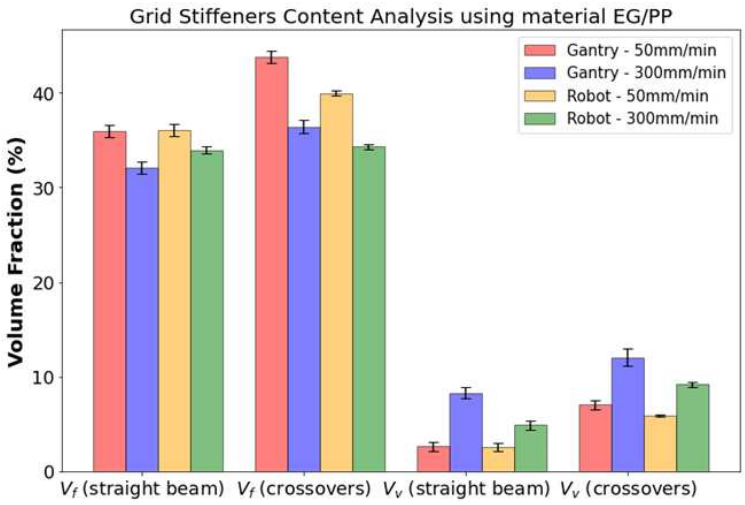

Figure 41: Fiber and void contents of beams and crossovers for Gantry and Robot Deposition.

One source of the increased void fraction could be related to fiber bridging at the crossovers, as suggested in figure 42. Buragohain et al. noted a resin rich area adjacent to the crossover which was due to fiber bridging present in the manufacture of grid stiffened structures. However, Buragohain used a thermoset prepreg and cured those structures in an autoclave, resulting in a resin rich, but low void content volume where fiber bridging is apparent [30].

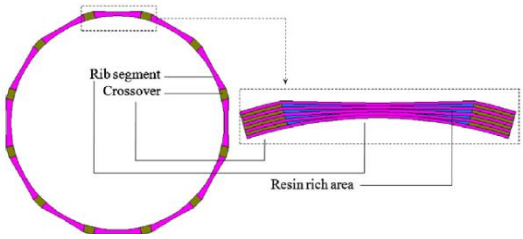

Figure 42: Example of fiber bridging as seen by Buragohain et al. [32].

In the present study, because there is only in-situ consolidation, the fiber bridging present may be more likely to trap voids as the local consolidation force is reduced. Based on the work of Hogan [50], investigating volume fraction variations within the straight beam sections, the fiber volume fraction was found to be lower, and the void volume fraction higher as he traversed toward the lateral edges of the placed tow. Thus, additional micrographic studies would be required to assess the void location and distribution at these crossovers and ultimately determine if voids are concentrated at the fiber bridging.

3.6 CONCLUSIONS

Both the gantry deposition using a nozzle for consolidation and the robotic deposition with a roller have successfully demonstrated the ability to produce high-quality, continuous fiber, composite grid crossovers with good thickness control at the intersections. The gantry system was able to achieve thickness deviations lower than 14.38% at the crossovers compared to the straight grid sections while the robotic system was able to achieve thickness deviations less than 8.01% at the crossovers. Although both systems are capable of minimizing thickness build-up at the crossovers, the roller deposition head on the robot, being mounted on a stiffer automation system, seems to be able to produce a more consistent geometry at varying speeds. Both systems can produce low void, high volume fraction continuous fiber reinforced composite grid stiffeners, particularly at low speeds, all with radically reduced tooling.

CHAPTER 4: BEAM OPTIMIZATION

After the baseline was established for the roller-based system and force-based feedback control of the system was implemented, attempts were made to reproduce the samples printed for the baseline testing. Samples were initially printed with force monitoring, no force control, to determine the force setpoints for the beams and for the crossovers. These prints were done with the same process parameters used for the baseline prints: a roller temperature of 250C, a print speed of 5mm/s, a layer height of 0.15mm and a z-step at the crossovers of -0.1mm. From these tests, the beam and crossover force setpoints were estimated to be 5lbs and 25lbs, respectively. Using these two force setpoints, a simple single crossover sample was printed using the previous values for temperature, print speed, and layer height. The negative z-step was replaced with the increased force of 25lbs, and the sample was printed with 20 layers. When this was done, the resulting thickness was around 1.6-1.7mm where the theoretical thickness of the sample was 3.0mm. To generate a more appropriate thickness, the force setpoint for the beams was decreased to 2.5lb and the speed increased to 10mm/s. Subsequent crossover prints revealed that the tow thinning that occurred during the crossover would not recover after the force setpoint changed from high back to low. This resulted in a thin beam section after the crossover which was not desirable. It was found that adding tension would cause thickening. Due to the difficulty in controlling the geometry of the crossover samples, it was decided to investigate how to control the geometry of simpler beam samples. The parameters found would then be applied to the crossover prints to see if the geometry of the prints could be improved.

4.1 Materials

The commingled tow feedstock used in this study is Compofil PP-60-R-1870N (Fiberglass Industries Twintex), a continuous E-glass/Polypropylene (EG/PP) untwisted commingled tow. The Tex of the roving

is 1870. The unprocessed weight fraction of the reinforcement is 60%, which corresponds to a 35% fiber volume fraction. PP tape was placed on top of the glass build plate to improve the bed adhesion of the commingled tow and to maintain the as-printed position on the substrate. The unprocessed commingled tow width is approximately 6mm.

4.2 Experimentation

The purpose of these tests was to determine parameters for printing the beams. For these studies, simple beams were printed with the intent to optimize towards having the correct (3mm) geometry. The 3mm thickness was determined by multiplying the layer height by the number of layers. From previous work, the layer height was determined to be 0.15mm. Additionally, the number of layers per sample was 20; this again aligned with the previous work discussed in Chapter 3: Baseline Testing and Comparison.

The thickness of each samples was measured using a micrometer, at 25mm increments along the length of the beam. Each location was measured 3 times. The start and stop locations represent where the load control was turned on and off, respectively. These are at the same location for every beam. An example of a beam printed can be seen in figure 43. The black dots on the sample are the locations where thickness was measured and range from 0mm to 250mm. The sample was printed right to left.

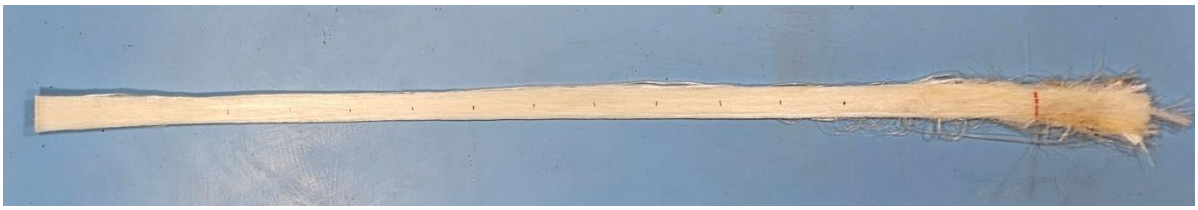

Figure 43: Printed beam sample.

While the print bed can accommodate multiple beam samples at once, only one beam was printed at a time, at the same location. This removes any variation of the bed levelness from impacting the samples in different ways; all the samples should have the same variation due to the position of the bed.

4.2.1 Taguchi Design of Experiments

A Taguchi method for design of experiments (DoE) was selected for these tests as it radically reduces the number of experiments needed when analyzing several parameters at multiple levels. Taguchi's method uses orthogonal arrays to help organize and run the series of experiments. An example of an L8 orthogonal array can be seen in table 6.

Table 6: Example of an L8 orthogonal array [69].

FACTOR / TRIAL	A	B	C	D	E	F	G
1	1	1	1	1	1	1	1
2	1	1	1	2	2	2	2
3	1	2	2	1	1	2	2
4	1	2	2	2	2	1	1
5	2	1	2	1	2	1	2
6	2	1	2	2	1	2	1
7	2	2	1	1	2	2	1
8	2	2	1	2	1	1	2

The L8 array allows seven different parameters to be tested against each other at two levels with only eight trials. In Table 1, A, B, C, etc., refer to the parameters being tested. Trial refers to which experiment is being run. The 1's and 2's in the table are the parameter levels, such as low or high. The organization of the parameters help to minimize the confounding and interference from the other parameters. The two types of orthogonal arrays that were used in this study were an L8 array and an L9 array. Where an L8 array tests seven parameters at two different levels, the L9 array can test four parameters at three different levels (low, med, high). Additionally, the L9 array takes nine trials to fill the array compared to the L8 which only takes eight.

Initially, an L9 orthogonal array was selected as the DoE that would be run. After these tests were run, the results were analyzed and found to be inconclusive. An L8 orthogonal array DoE was then run to investigate the interaction effects of the parameters in order to draw more meaningful conclusions from the original L9 array.

The initial L9 study had four parameters varying at three different levels. The four parameters that were manipulated are tension, force setpoint, roller temperature and print speed. The parameters and levels are summarized in table 7.

Table 7: Parameter summary.

Tension		No Tube	Half length	Full length
Temp		240C	260C	280C
Speed		7.5mm/s	10mm/s	12.5mm/s
Force		2lb	3lb	4lb

Tension is generated by passing the tow through a narrow tube; the contact between the tow and the tube wall generates friction and subsequently tension in the tow. The longer the length of tubing the more friction is generated and the higher the tow tension. Three different lengths of tubing were used at the three different tension levels. The tensioning method and the lengths of tube can be seen in figure 44. The tube is ¼" ID polyethylene air hose; the shorter tube is 2.5" in length while the longer tube is 5" in length.

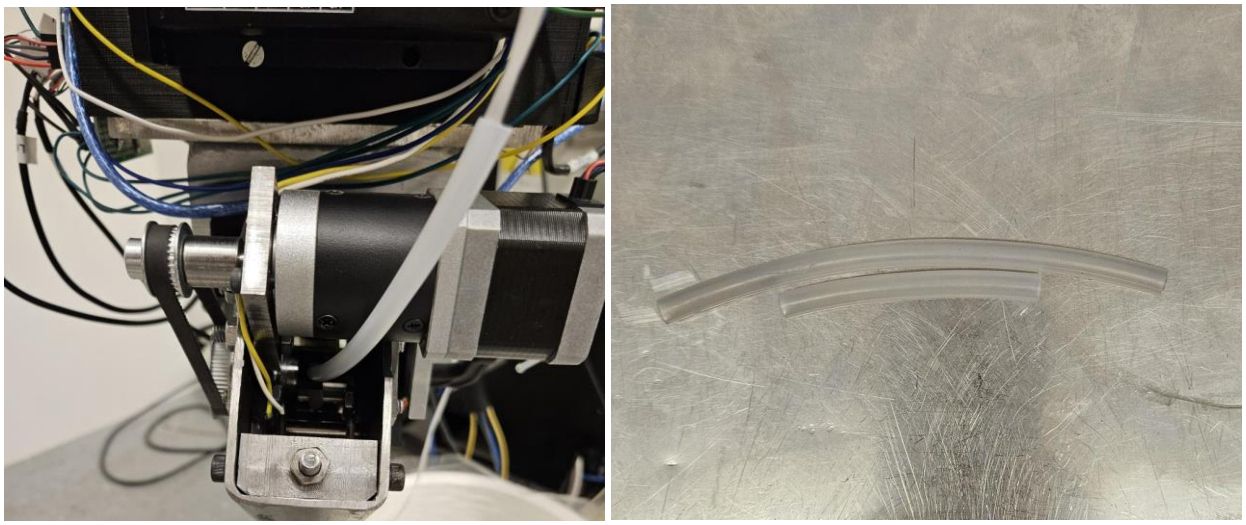

Figure 44: Tensioning method (left) and varying lengths of tube (right).

The Taguchi DoE is summarized in Table 8. Each of these parameter sets, or treatments, have three replicates.

Table 8: Taguchi DoE.

Sample	Tension	Temp	Speed	Force
1	No tube	240C	7.5mm/s	2lb
2	No tube	260C	10mm/s	3lb
3	No tube	280C	12.5mm/s	4lb
4	Half length	240C	10mm/s	4lb
5	Half length	260C	12.5mm/s	2lb
6	Half length	280C	7.5mm/s	3lb
7	Full length	240C	12.5mm/s	3lb
8	Full length	260C	7.5mm/s	4lb
9	Full length	280C	10mm/s	2lb

With the samples for this study manufactured, analysis was done using the average thickness as the output response. It is typical to use the signal-to-noise (S/N) ratio in this type of analysis and that is what was done. The S/N ratio is calculated using the mean sum of deviations or MSD. For the thickness data, the MSD used was "nominal is best" in which a nominal value is subtracted from the average of each run and the mean sum of squares is then calculated using the runs from a specific sample [69]. The equation for this can be seen below.

$$MSD = ((y_1 - m)^2 + (y_2 - m)^2 + \cdots + (y_n - m)^2)/n \quad (1)$$

Where y_i is the average of each run, m is the nominal value (3 in this case) and n is the number of runs. Mean squared deviations have the benefit of capturing the variance within each parameter set and the variation from the target value. This is then converted into the S/N ratio by the following equation.

$$SN = -10 * \log(MSD) \quad (2)$$

The next step in the analysis is to calculate the "main effects." This refers to the influence or significance each individual parameter has on the variation and the target value. The process to capture the main effects is as follows: the S/N ratio of all the samples with the same parameter at the same level are averaged to get the main effect for that parameter at that level [69]. For example, to determine the influence of the low level of tension, the S/N ratios of the first three runs would be averaged. As another example, to determine the influence of the high temperature setpoint (280C), the S/N ratio for samples

3, 6, and 9 are averaged. Finally, an ANOVA test was run on the data to determine the statistical significance; note that the ANOVA test was done using the thickness data not using the S/N ratios.

Incorporating a second output was thought to give a better set of optimized parameters. The two outputs to be considered were the sample average thickness and the thickness deviation along the length of the sample. The method selected for analyzing the two outputs was Grey's Relational Analysis. This method normalizes the S/N ratios between 1 and 0 of each of the outputs and then uses those to compute the grey relational coefficient (GCs). The GCs are then used to compute the grey relational grade; these are then used to similar to the main effects graphs/tables previously employed.

A second set of experiments were planned and executed to determine the interaction effects between parameters. For this set of experiments, only two levels were used and speed was held constant; this allows for investigation of interaction between tension, temperature and force. A summary of the parameters and the levels can be seen in table 9.

Table 9: Summary of parameters and levels.

	1	2
Tension	No tube	Full length
Temp	260C	280C
Speed	10mm/s	
Force	3lb	4lb

The levels of the experiment were selected by eliminating the lowest S/N ratio of each parameter seen in Table 8. The L8 Taguchi DoE can be seen in table 10.

Table 10: L8 orthogonal array.

Sample	Tension	Temp	Tension x Temp	Force	Tension x Force	Temp x Force	e
1	No tube	260C	1	3lb	1	1	1
2	No tube	260C	1	4lb	2	2	2
3	No tube	280C	2	3lb	1	2	2
4	No tube	280C	2	4lb	2	1	1
5	Full length	260C	2	3lb	2	1	2
6	Full length	260C	2	4lb	1	2	1
7	Full length	280C	1	3lb	2	2	1
8	Full length	280C	1	4lb	1	1	2

At least one repetition has been printed for each parameter set. The last column is not testing any additional parameters but can be used to calculate the error of the experiment so an ANOVA analysis can be run with only a single replicate per treatment. The data from this study was not transformed into the S/N ratio as the previous attempt to use the S/N ratio was not successful; the "optimized" print conditions found using the S/N ratio resulted in very thin samples The average thicknesses of the samples were used as the output responses.

To find the optimum, the output was predicted by using the following formula from [70].

$$Y_{opt} = Y_{ave} + (Y_A - Y_{ave}) + (Y_B - Y_{ave}) + \cdots + (Y_N - Y_{ave}) \quad (3)$$

Y_{opt} is the optimum output, Y_{ave} is the average output from all the samples, Y_A is the contribution from parameter A and there are N number of parameters.

4.2.2 Void and Fiber Volume Fraction Measurement

A void and fiber volume fraction measurement was also performed. For the void and fiber volume fraction analysis, the specimens were cut from samples and the densities were found. 50mm specimen were cut from one sample from each parameter set used in the L9 Taguchi array using a water-cooled diamond saw. The sectioned specimen thickness was matched to the corresponding average thickness of the sample. To determine the void volume fraction of a specimen, the Archimedes principle was used to find the density. To determine the volume of each specimen, the fluid displacement method, based on

ASTM 792, was used [67]. A water-based solution was used, in a ratio of 32:1 deionized (DI) water to RedLine Water Wetter in order to minimize the bubble formation on the specimens and thus improve the accuracy of the measurement. This specimen volume is then divided into the measured mass to give the measured density. This is compared to the theoretical density to determine void content. To determine the weight fraction of fibers in each specimen, the matrix burn-off method was performed, according to ASTM D3171 [68]. The specimens are put in the furnace, in air, and the temperature is set to 547°C for at least 4 hours to ensure complete removal of the matrix. The loose fibers are then weighed, allowing determination of both fiber and void volume fractions through the use of manufacturer supplied densities. Note that the previous temperature used for burn-offs was 596°C. This discrepancy is due to a setpoint change on the muffle furnace that was not noticed until the end of the burn-off. While this temperature is not consistent compared to previous testing, it does still align with the ASTM D3171, which states heating the furnace to 565±30°C [68].

4.2.3 Metallographic Evaluation

Microscopic evaluation of several beams was done as a final evaluation. While the burn-off testing does provide a birds-eye view of the constituent materials and void contents, it excludes information about void size and locations within the laminate. These specimens were harvested from beams used in the void fraction analysis. Only three specimens were used in the microscopy analysis; these three specimens represented low, medium and high void contents.

4.3 Results

4.3.1 Taguchi Study and Optimization

The results of the original L9 Taguchi DoE are summarized in table 11.

Table 11: Run averages and subsequent S/N ratios. S/N ratio is dimensionless.

Sample	Tension	Temp	Speed	Force	Run 1	Run 2	Run 3	Thickness	Std Dev	MSD	SN
1	No tube	240C	7.5mm/s	2lb	3.380mm	3.191mm	3.365mm	3.312mm	0.086mm	0.105	9.800
2	No tube	260C	10mm/s	3lb	3.073mm	2.893mm	2.912mm	2.959mm	0.081mm	0.008	20.876
3	No tube	280C	12.5mm/s	4lb	2.198mm	2.821mm	2.771mm	2.579mm	0.283mm	0.243	6.152
4	Half length	240C	10mm/s	4lb	2.837mm	2.863mm	2.998mm	2.889mm	0.071mm	0.015	18.206
5	Half length	260C	12.5mm/s	2lb	4.141mm	4.027mm	4.15mm	4.106mm	0.056mm	1.226	-0.886
6	Half length	280C	7.5mm/s	3lb	2.701mm	2.701mm	2.468mm	2.623mm	0.110mm	0.154	8.126
7	Full length	240C	12.5mm/s	3lb	3.874mm	4.209mm	3.411mm	3.831mm	0.327mm	0.798	0.979
8	Full length	260C	7.5mm/s	4lb	2.675mm	2.808mm	2.753mm	2.754mm	0.055mm	0.068	11.686
9	Full length	280C	10mm/s	2lb	3.094mm	3.002mm	3.274mm	3.123mm	0.113mm	0.028	15.533

The main effects of this DoE are summarized in tables 12 and 13.

Table 12: Main effects using S/N ratio summary with optimum parameters highlighted. S/N ratio is dimensionless.

Level	Tension	Temp	Speed	Force
1	12.286	9.928	9.871	8.153
2	8.481	10.568	18.214	10.266
3	9.669	9.939	2.350	12.016
Delta	3.805	0.639	15.864	3.863

Table 13: Main effects using average thickness summary.

Level	Tension	Temp	Speed	Force
1	2.956mm	3.327mm	2.893mm	3.514mm
2	3.209mm	3.270mm	2.994mm	3.118mm
3	3.213mm	2.781mm	3.491mm	2.747mm
diff	0.257mm	0.547mm	0.598mm	0.766mm

The delta row is the range for each parameter across the different levels; this can give an indication of the significance each parameter has. The S/N ratio main effects graph is presented in figure 45.

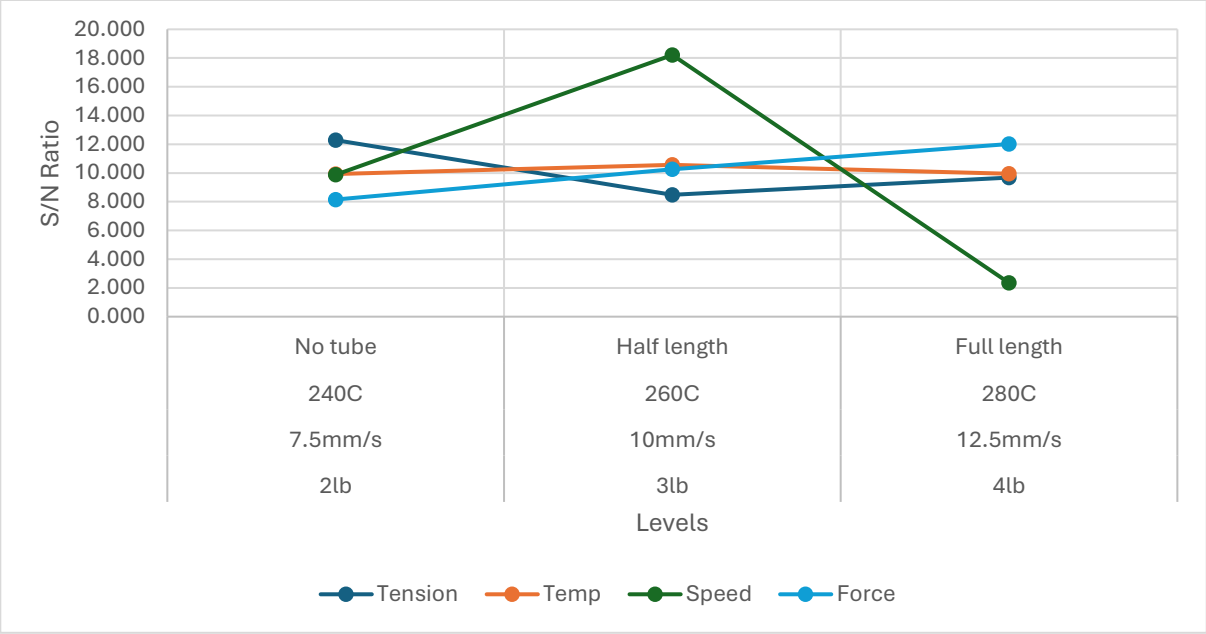

Figure 45: S/N ratio main effects graph.

According to this data after the transformation to S/N ratio, speed has the largest impact on the variance of the output geometry. The larger the magnitude, the more the influence the parameter level has on the output. From this data, some optimized parameters can be found; the maximums of each of the main effects indicate the parameters giving the minimum variance. As such, the “optimum” parameters found by this study are no tube, a speed of 10mm/s, a temperature of 260C and a force setpoint of 4lbs. However, looking at the untransformed average thickness data, the force is the parameter with the greatest influence over the output geometry. An ANOVA test was run on the data to determine the statistical significance; note that the ANOVA test was done using the thickness data not using the S/N ratios. This was done by hand in Excel and the results were then confirmed in MATLAB; the results can be seen in table 14.

Table 14: ANOVA Results.

	f	Sum Sq.	Mean Sq.	F	Contribution (%)	P	Pcrit
Tension	2	0.391	0.196	5.915	4.58%	0.011	0.049
Temp	2	1.624	0.812	24.548	21.94%	0.000	
Speed	2	1.844	0.922	27.875	25.04%	0.000	
Force	2	2.644	1.322	39.979	36.32%	0.000	
Error	18	0.595	0.033	1	0		
Total	26	7.098					

The critical P value for the null hypothesis to be true was 0.0486; this means that for any P value less than the critical value, the null hypothesis is false and therefore the parameter is significant. Interestingly, according to the ANOVA, the force is the most significant parameter while the tension is by far the least. The contribution column is a percentage. However, all the parameters are statistically significant.

A sample was printed at the “optimized” parameters and the average thickness of this sample was 2.625mm with the target thickness being 3mm. Clearly, there is a discrepancy between the “optimized” output and the target output. This is most likely due to interaction effects between the parameters which were not considered.

With the poor prediction offered by the original analysis, incorporating a second output into the analysis was done. As previously stated, the use of Grey’s Relational Analysis was the method used to incorporate an additional output. The table with the summary of the effects can be seen in table 15.

Table 15: Main effects summary using Grey’s Relational Analysis.

Level	Tension(a)	Temp(b)	Speed(C)	Force(d)
1	0.673	0.606	0.733	0.628
2	0.649	0.730	0.768	0.698
3	0.714	0.699	0.534	0.710
diff	0.065	0.124	0.234	0.082

As can be seen in Table 15, the optimum parameter levels are full tension, a temperature of 260C, a speed of 10mm/s, and a force of 4lbs. Only two samples were printed at the optimized parameters; the average thickness of each sample was 2.692mm and 2.724mm with deviations along the length (standard deviation) of 0.163mm and 0.113mm. The deviation of the original optimized parameter set was 0.160mm. Some slight improvement to both the average thickness and the deviations were seen with the use of two outputs. Still, interactions were not considered and doing so could yield improved accuracy of the resulting analysis.

The second Taguchi DoE was done to investigate the interaction effects between parameters while holding the speed constant. The average thicknesses of the samples were used as the output responses. The results of the L8 DoE are summarized in table 16, the main effects are summarized in table 17 and the ANOVA results can be seen in table 18.

Table 16: Average thickness data from the L8 Taguchi DoE.

Sample	Tension	Temp	Tension x Temp	Force	Tension x Force	Temp x Force	e	Ave Thickness
1	No tube	260C	1	3lb	1	1	1	2.959mm
2	No tube	260C	1	4lb	2	2	2	2.625mm
3	No tube	280C	2	3lb	1	2	2	2.744mm
4	No tube	280C	2	4lb	2	1	1	2.572mm
5	Full length	260C	2	3lb	2	1	2	3.067mm
6	Full length	260C	2	4lb	1	2	1	2.708mm
7	Full length	280C	1	3lb	2	2	1	2.574mm
8	Full length	280C	1	4lb	1	1	2	2.431mm

Table 17: Main effects table for L8 orthogonal array.

Level	Tension	Temp	Force	Tension x Temp	Tension x Force	Temp x Force	e
1	2.725mm	2.840mm	2.836mm	2.647mm	2.711mm	2.757mm	2.703mm
2	2.695mm	2.580mm	2.584mm	2.773mm	2.710mm	2.663mm	2.717mm
diff	0.030mm	0.260mm	0.252mm	0.126mm	0.001mm	0.095mm	0.014mm

Table 18: ANOVA results from L8 array.

	f	S	V	F	Contribution (%)	P	Pcrit
Tension	1	0.001	0.001	4.974	0.002	0.268	0.140
Temp	1	0.068	0.068	367.482	0.215	0.033	
Tension x Temp	1	0.016	0.016	85.857	0.050	0.068	
Force	1	0.064	0.064	345.420	0.202	0.034	
Tension x Force	1	1.190E-06	1.190E-06	0.006	-0.001	0.949	
Temp x Force	1	0.009	0.009	48.563	0.028	0.091	
e	1	1.839E-04	1.839E-04	1	0		
Sstot	7	0.314					

The results of the ANOVA indicate that temperature, force, the interaction between temperature and tension and the interaction between temperature and force are the only effects that have an impact on the average thickness of the sample. Interaction graphs were also used to confirm the interactions indicated by the ANOVA; the difference in slope between the plotted lines in the interaction graph reveal the influence of the interaction. These graphs can be seen in figures 46-48.

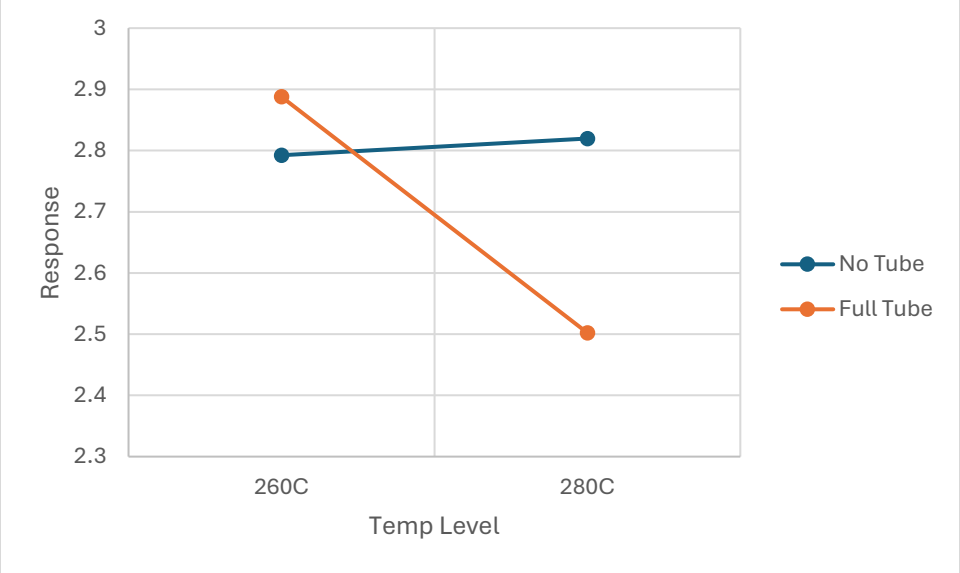

Figure 46: Tension-temperature interaction.

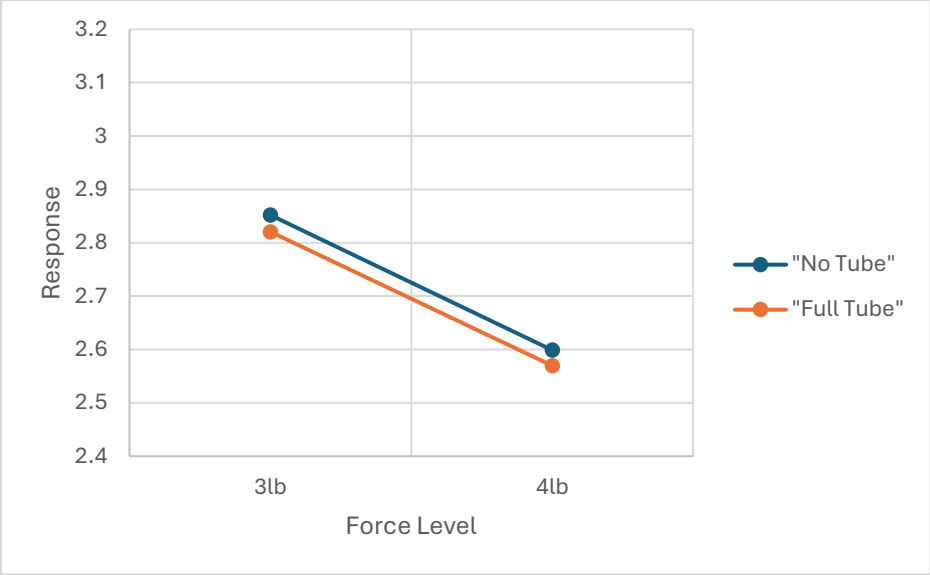

Figure 47: Tension-force interaction.

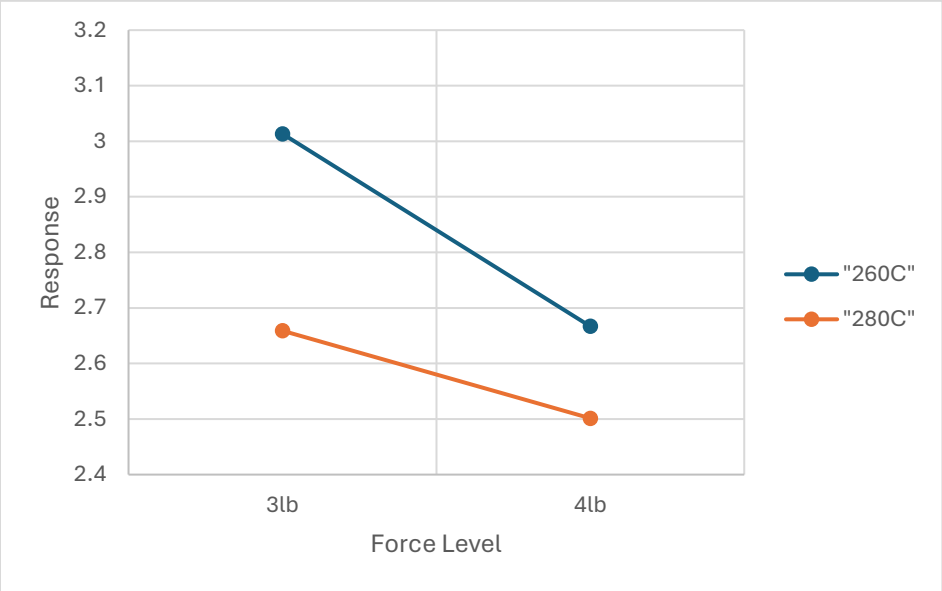

Figure 48: Temperature-force interaction.

In Figure 46, the intersection indicates strong interaction between the temperature and tension parameters; similarly, in Figure 48 the difference in slope between the two lines suggests an interaction between the temperature and the force. Finally, there was no interaction between the force and the tension. This can be seen in Figure 47 and is indicated by the parallel lines of the interaction graph.

Equation (3) was used to predict the optimized output of the parameters. For example, the following calculation was done to find the optimum parameters for the 7.5mm/s speed:

$$Y_{opt} = Y_{ave} + (2.956mm - Y_{ave}) + (3.328mm - Y_{ave}) + (2.894mm - Y_{ave}) + (3.118mm - Y_{ave}) = 2.916mm \quad (3)$$

Using this method, an optimum parameter sets for the 7.5mm/s and 10mm/s speeds. From the thickness data from the L9 array, the 7.5mm/s parameters were found to be no tube (low tension), a roller temperature of 240C and a force setpoint of 3lbs. From the thickness data from the L8 array the 10mm/s parameters were selected as: high tension, a temperature of 260C and a force of 3lbs. With these parameters, the predicted average thicknesses were2.916mm and 3.029mm for the 7.5mm/s and 10mm/s speeds, respectively. Five samples were printed at each speed to test the validity of these parameters; the average thickness of the samples printed at 7.5mm/s was 3.021mm and the average thickness of the samples made at 10mm/s was 3.008mm. The results can be seen in table 20.

Equation 3 was also used to predict the output for the 12.5mm/s speed; the parameters of this prediction were low tension (no tube), a temperature of 280C and a force setpoint of 3lb with a predicted thickness of 2.967mm. The result of this test was a beam with a thickness of 2.713mm. Only one sample was printed using this parameter set. After this, tension was added as the high setpoint (full length tube); the temperature was held at 280C, and the force was held at 3lb. This resulted in a sample with a thickness of 2.535mm and only a single sample was made. Finally, a sample was printed with high tension, a roller temperature of 280C and force setpoint of 2lb. Only one sample was printed at these parameters and the thickness of this sample was 3.571mm. From these tests, it was assumed that interpolating between the force setpoints was the best way to get an appropriate thickness. In doing this, the interpolation of a 2.5lb setpoint predicted a thickness of 3.054mm. The initial sample printed at these had a thickness of 2.950mm and this was assumed to be a good parameter set for 12.5mm/s. From this iterative trial and error approach the following parameters were found for 12.5mm/s: full

tension, a roller temperature of 280C and a force setpoint of 2.5lbs. With the optimum parameters for 12.5mm/s found, 5 samples of each were printed as verification of the parameters. The optimum parameters are summarized in table 19 and results of the verification prints can be seen in table 20.

Table 19: Optimized parameter summary.

	Tension	Temp	Force
7.5mm/s	None	240C	3lb
10mm/s	Full	260C	3lb
12.5mm/s	Full	280C	2.5lb

Table 20: Verification of optimized parameters.

7.5mm/s						
	Run 1	Run 2	Run 3	Run 4	Run 5	
0mm	3.280mm	3.433mm	3.078mm	3.243mm	3.253mm	
25mm	2.991mm	3.268mm	3.142mm	3.2567mm	3.334mm	
50mm	2.996mm	3.178mm	3.278mm	3.181mm	3.455mm	
75mm	2.830mm	2.841mm	3.247mm	3.028mm	3.304mm	
100mm	2.723mm	2.750mm	3.311mm	2.903mm	3.162mm	
125mm	2.668mm	2.717mm	3.143mm	2.774mm	3.012mm	
150mm	2.766mm	2.816mm	3.205mm	2.828mm	3.076mm	
175mm	2.859mm	2.886mm	3.325mm	2.814mm	3.102mm	
200mm	2.757mm	2.885mm	3.281mm	2.865mm	3.041mm	
225mm	2.667mm	2.712mm	2.987mm	2.796mm	2.891mm	
250mm	2.991mm	2.880mm	3.033mm	2.933mm	2.988mm	Total
Average	2.866mm	2.942mm	3.185mm	2.966mm	3.147mm	3.021mm
SD	0.176mm	0.230mm	0.111mm	0.174mm	0.163mm	0.123mm
10mm/s						
0mm	2.895mm	2.909mm	2.977mm	3.093mm	3.173mm	

25mm	2.760mm	3.017mm	3.007mm	3.286mm	2.876mm	
50mm	3.044mm	3.236mm	3.036mm	3.269mm	2.907mm	
75mm	3.049mm	3.200mm	3.024mm	3.198mm	2.903mm	
100mm	3.023mm	3.023mm	3.064mm	3.098mm	2.809mm	
125mm	2.952mm	2.866mm	3.036mm	3.116mm	2.686mm	
150mm	2.954mm	2.958mm	3.172mm	3.134mm	2.798mm	
175mm	3.105mm	2.934mm	3.234mm	3.223mm	2.859mm	
200mm	3.125mm	2.933mm	3.119mm	3.271mm	2.886mm	
225mm	2.988mm	2.793mm	2.888mm	2.996mm	2.792mm	
250mm	3.003mm	2.893mm	2.933mm	3.000mm	2.910mm	Total
Average	2.991mm	2.978mm	3.045mm	3.153mm	2.873mm	3.008mm
SD	0.097mm	0.129mm	0.096mm	0.099mm	0.115mm	0.091mm
12.5mm/s						
0mm	3.034mm	2.746mm	3.274mm	3.363mm	3.038mm	
25mm	2.960mm	2.675mm	3.373mm	3.634mm	3.096mm	
50mm	3.146mm	2.871mm	3.532mm	3.893mm	3.198mm	
75mm	3.125mm	2.918mm	3.527mm	3.967mm	3.200mm	
100mm	3.273mm	2.935mm	3.391mm	3.767mm	3.113mm	
125mm	3.162mm	3.013mm	3.146mm	3.392mm	3.035mm	
150mm	3.243mm	2.985mm	3.240mm	3.293mm	3.031mm	
175mm	3.330mm	3.130mm	3.292mm	3.341mm	3.067mm	
200mm	3.185mm	3.232mm	3.392mm	3.290mm	3.070mm	
225mm	2.939mm	3.012mm	3.289mm	3.113mm	2.878mm	

250mm	2.953mm	2.935mm	3.301mm	3.153mm	2.993mm	Total
Average	3.123mm	2.950mm	3.342mm	3.473mm	3.065mm	3.191mm
SD	0.129mm	0.149mm	0.111mm	0.281mm	0.086mm	0.190mm

While further iterations on these parameters would yield better results, this establishes a baseline for the process. The high average thickness of the 12.5mm/s samples suggests that this was not a truly "optimized" parameter set. Also, the interpolation was based off of single samples that could have been anomalies. Additionally, the initial print done with 12.5mm/s parameters could have been an anomaly.

4.3.2 Void and Fiber Volume Fraction

A void and fiber volume fraction analysis of the beams was also performed. This was not the overall optimization objective but was included in the study. Void and fiber volume fraction are common metrics used to express the overall quality of the composite. As such, maintaining geometric fidelity is not applicable if the overall quality of the composite is poor. Only samples from the original L9 Taguchi array were used for this analysis. The results of the burn-offs can be seen summarized in table 21.

Table 21: Fiber and void volume fraction analysis summary and samples selected for microscopic evaluation.

Sample	Tension	Temp	Speed	Force	Vf	Vv
1	No tube	240	7.5	2	33.10%	6.82%
2	No tube	260	10	3	33.63%	4.70%
3	No tube	280	12.5	4	33.55%	4.92%
4	Half length	240	10	4	34.00%	5.56%
5	Half length	260	12.5	2	33.30%	5.66%
6	Half length	280	7.5	3	34.28%	1.98%
7	Full length	240	12.5	3	32.61%	8.73%
8	Full length	260	7.5	4	34.55%	3.25%
9	Full length	280	10	2	34.72%	3.19%

From these results, the main effects can be seen in tables 22 and 23 for fiber fraction and void fraction, respectively. These main effects were calculated in the same way the main effects were calculated for the thickness measurements in the previous Taguchi studies.

Table 22: Main effects table for fiber volume fraction.

Level	Tension	Temp	Speed	Force
1	33.43%	33.24%	33.97%	33.71%
2	33.86%	33.82%	34.12%	33.50%
3	33.96%	34.18%	33.15%	34.03%
Delta	0.54%	0.95%	0.96%	0.53%

Table 23: Main effects table for void volume fraction.

Level	Tension	Temp	Speed	Force
1	5.48%	7.04%	4.02%	5.22%
2	4.40%	4.54%	4.48%	5.14%
3	5.06%	3.36%	6.43%	4.57%
Delta	1.08%	3.67%	2.42%	0.65%

In tables 22 and 23, the “best” level for each parameter are highlighted in green; for fiber fraction, the maximum values are highlighted whereas for the void fraction, the minimum values are highlighted. Unsurprisingly, the highest temperature, the lowest speed and the highest force results in the lowest void content. Similarly, the temperature had the largest impact on void fraction and speed had the second largest impact. Equation (3) was used again to predict what the lowest void content achievable was. Using this method, the predicted minimum void content was 1.49%.

4.3.3 Metallographic Evaluation

Three specimen were also harvested from three of the samples used in void analysis for microscopic evaluation and are highlighted in table 21. These samples have the minimum and maximum void contents as well as the average of the two; samples 6, 7 and 4 represent these values, respectively. Images of these specimen can be seen in figures 49-51.

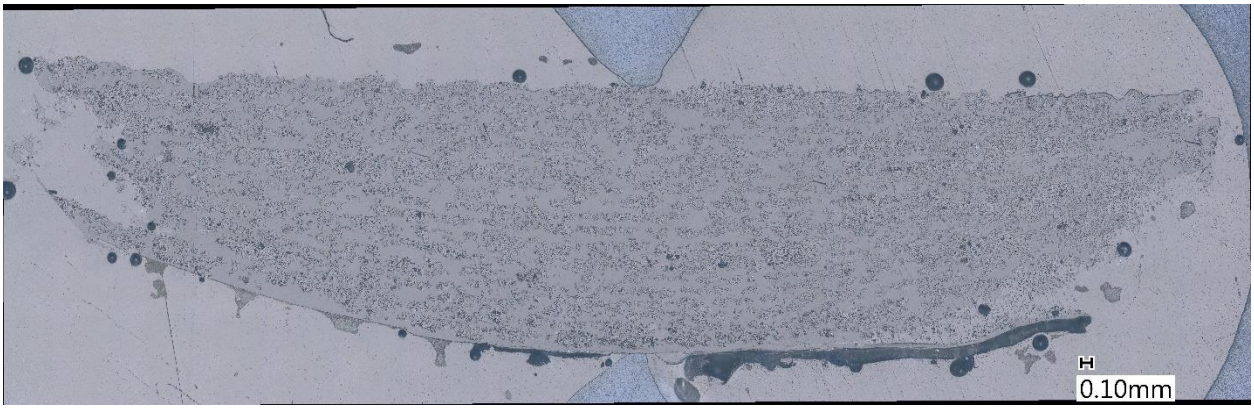

Figure 49: Image of sample 6, low void content.

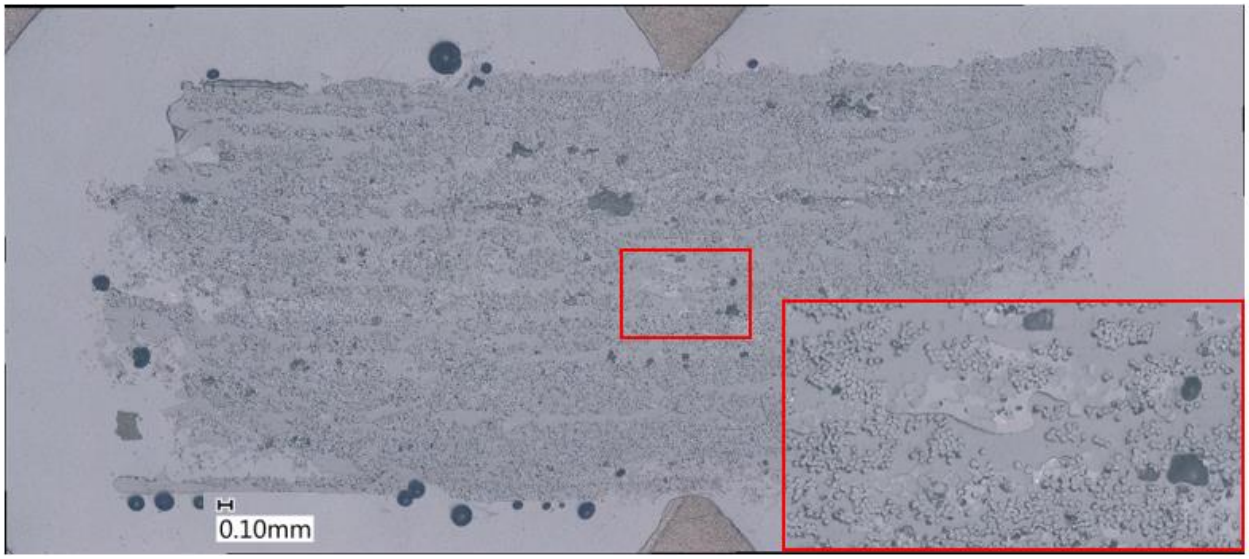

Figure 50: Image of sample 7, high void content. Red box indicates thermoplastic fibers.

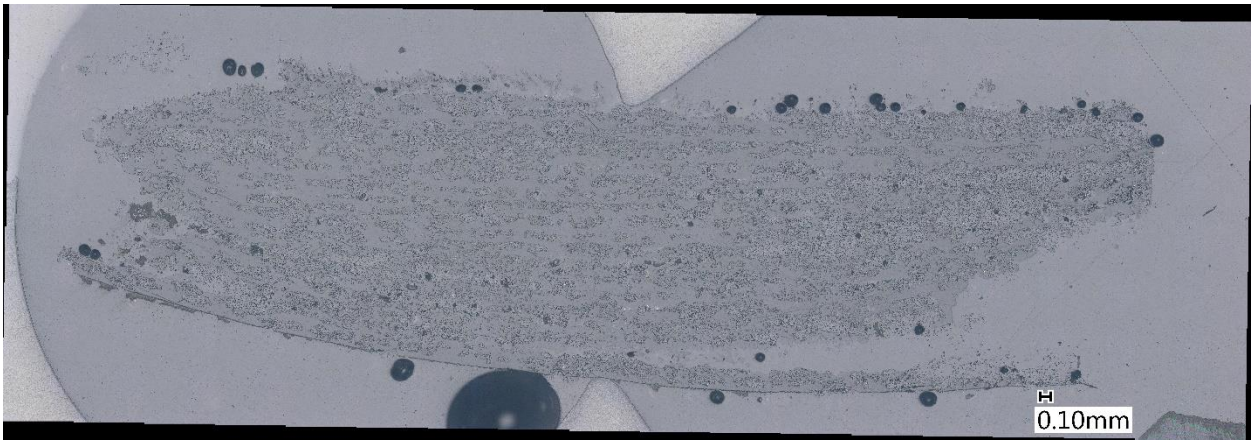

Figure 51: Image of sample 4, medium void content.

4.4 Discussion

From the initial study some general trends can be seen, especially when examining the main effects seen in table 12. Unsurprisingly, as the roller temperature increased, the sample thickness decreased. Similarly, as the force increased, the sample thickness decreased. Conversely, as the speed increased, so did the sample thickness. Finally, as tension on the tow increased, so did the thickness of the sample.

Thinning due to an increase in roller temperature is easily explained as the matrix viscosity drops with an increase in temperature. This allows the fibers in the tow bundle to shift with less resistance, resulting in a thinner tow. Thinning of the tow due to increased force is also intuitive as one would expect the fibers within the tow bundle to slide past each other and shift laterally as more force is applied through the thickness. The direct relationship between the speed and the thickness can be explained by a combination of the previous two arguments stated. As the tow passes under the roller more slowly, the matrix spends a longer time exposed to the high temperature of the roller, allowing for the matrix to reach a higher temperature and causing the matrix viscosity to drop more. Further, the more time the tow spends under the roller, the more time the tow experiences the force exerted by the roller, allowing for more spreading to occur.

The most difficult trend to explain is the increase in thickness due to an increase in tension. Typically, when tension is applied to a tow and the tow is passed over a roller or pin, the tow spreads. This is due to the resultant normal force applied to the tow bundle through the thickness of the bundle [71]. Increasing the tension applied to the tow has been seen to increase the degree of spreading [72], [73]. This contradicts the trend seen in the original Taguchi study. One explanation could be the tensioning method used; because the tow passes through a narrow tube, the tow is not inherently spread like it would be tensioning via a roller. This results in a tow that remains more collimated as it passes under the roller. Additionally, the high viscosity of the matrix may have contributed to the tow remaining

collimated as it passed under the roller. Examination of the interaction effects provides some evidence of this.

Interactions have a clear impact on effects of the parameters at the levels explored in these studies. From the L8 Taguchi study, the strongest interaction was between the tension and the temperature. As seen in Figure 46, adding tension while the roller was at the lower (260C) temperature caused a thickness increase while adding tension with the roller at the higher (280C) temperature caused a thickness decrease. This thinning at higher temperatures could be due to a viscosity drop in the matrix at the higher temperature. The temperature-force interaction was also present in the L8 Taguchi study but at a lesser degree than the tension-temperature interaction; this is indicated by the larger Contribution % seen in the ANOVA analysis, 4.97% for the tension-temperature interaction vs. 2.79% for the temperature-force interaction. The temperature force interaction is that at lower temperatures, changing the force output results in a greater thickness change. So, with a roller temperature of 260C, the change in force from 3lbs to 4lbs resulted in a thickness change of 0.35mm. With a roller temperature of 280C, the change in the force from 3lbs to 4lbs resulted in a thickness change of 0.15mm. This is counter intuitive as when the roller temperature increases, the matrix viscosity drops. At lower viscosity, that matrix flows more easily; one would expect that this would increase the influence the applied force has on the beam thickness. One explanation could be that the higher temperature the tow inherently spreads more. As a result, the wider tow increases the area of contact of the roller, effectively decreasing the pressure applied on the tow and therefore decreasing the effect of increasing the force output.

Unsurprisingly, when these interactions were not included in the original S/N analysis and the follow-up Grey's Relational analysis the impact of the parameters on the geometry output was badly misconstrued. Both of these methods for analysis resulted in parameter selection which resulted in samples below the target thickness. Interestingly, the unmodified thickness data was used to find parameters for the

7.5mm/s speed using equation (3). Despite not including interaction effects, this data did result in "optimized" parameters for the 7.5mm/s speed. This could indicate that the interaction effects seen in the second Taguchi study may only be significant at higher speeds, temperatures or forces. This is further supported by equation (3) failing to accurately predict the sample thickness at given parameters for the 12.5mm/s speed. Along similar lines, the average thickness and high standard deviation of the beam thickness at the "optimized" parameters at 12.5mm/s may indicate that other interaction effects are present. Alternatively, it may indicate that the parameter levels for tension, temperature and force are near the bounds for this speed. It could also indicate that the differences in the levels within a given parameter are too large i.e., 2.5lb force setpoint used in the "optimum" parameters for the 12.5mm/s speed.

Examination of the void content helps to provide support for previously known trends and sheds some light on new trends. Unsurprisingly, the higher the temperature of the roller, the lower the void content. Similarly, the slower the speed of the roller the lower the void content. Both these trends have been seen in past work at the CMMS, albeit with the use of a nozzle as opposed to a roller [42], [46], [47]. The higher temperature and slower speed both contribute to lowering the viscosity of the matrix material. This allows better wetting of the fibers and facilitates the removal of entrained air, lowering the void content. Surprisingly, the consolidation force parameter played the smallest role for void content. While it has been documented that there is an upper limit to benefits consolidation force has on void content, the lack of influence is unexpected [74]. One explanation is provided by examining metallographic specimen harvested from the beams used in the fiber and void fraction analysis.

As seen in Figures 50 and 51 there are thermoplastic fibers that remain un-melted within the laminate. The presence of thermoplastic fibers in the microscopic images does give an indication of the importance of heat flow into the material as a result of either temperature or deposition speed. Further, this also suggests why force has such a small impact. If plastic fibers are visible this indicates that not

enough heat was transferred into the tow to cause melting. Because the matrix did not flow, regions of air surrounding the plastic fibers did not get pushed out of the laminate, resulting in voids. Further, if the plastic fibers remain intact, varying the force will have little effect on the void content as matrix material is not in a state to be reformed.

Additionally, the limited impact of the consolidation force on the void content could be due to a lack of lateral constraint during deposition. As the tow is deposited, force is provided on the top and bottom of the tow from the roller and the previous layer/substrate, respectively. There is nothing, however, providing any constraint on the sides of the tow; as a result, there is a pressure gradient within the tow peaking at the center of the tow and at a minimum on the sides of the tow. This can result in the voids being pushed to the edges of the tow but not being collapsed.

4.5 Conclusions

This study has proven the ability to achieve consistent tow thicknesses through the manipulation of four variables: tow tension, roller temperature, deposition speed and compaction force. Further, at three different speeds, optimum tension, temperature and force settings were found to achieve the desired tow thickness of 3mm. Force was the most impactful parameter on the thickness of the samples followed by speed, then temperature and finally tension. When deposition speed was held constant, an interesting interaction occurred between tension and temperature: at lower temperature, increased tension caused thickening while at higher temperature, increased tension caused thinning. This was attributed to viscosity changes in the matrix and the tensioning method employed. An analysis of the constituent materials was also done to determine void and fiber volume fractions. In terms of void content, the temperature had the strongest influence on the output; as the temperature increased, the content decreased. For the deposition speed, the interaction was the second strongest and as the speed increased, the void content increased as well. Interestingly, the consolidation force had the smallest

impact on the sample void content. This was assumed to be due to incomplete melting of the matrix fibers during deposition. The un-melted thermoplastic cannot flow and therefore cannot be easily formed; this limits the influence of the compaction force on the void content.

Based on the results of optimization for straight beam segments, focus shifted to getting parameters for consistent crossovers. Previous work on the crossovers in the original study had indicated that by slowing the print head, there was better control over the crossover thickness. The previous work used a -0.1mm z step at the crossover to induce the tow thinning and subsequent spreading at the crossover. As discussed in Chapter 3, the z step was greater than the required half tow thickness as the system is not infinitely rigid. With the implementation of the force feedback control the force setpoint was changed at the crossover to induce the tow thinning/spreading at the crossover. However, the tow would remain thin after the crossovers and fail to recover, resulting in two different beam geometries, one before and another after the crossover. The difference before and after the crossover can be seen in figures 52 and 53, where the tow is narrower and thicker as it approaches the intersection and wider and thinner after passing the intersection.

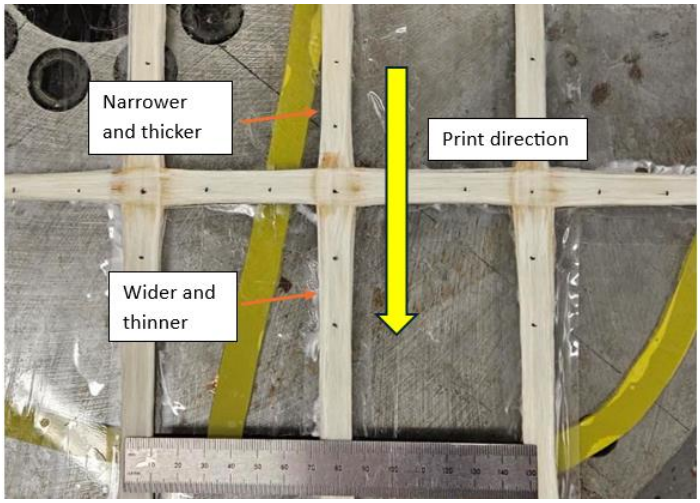

Figure 52: Width deviations before and after the crossover.

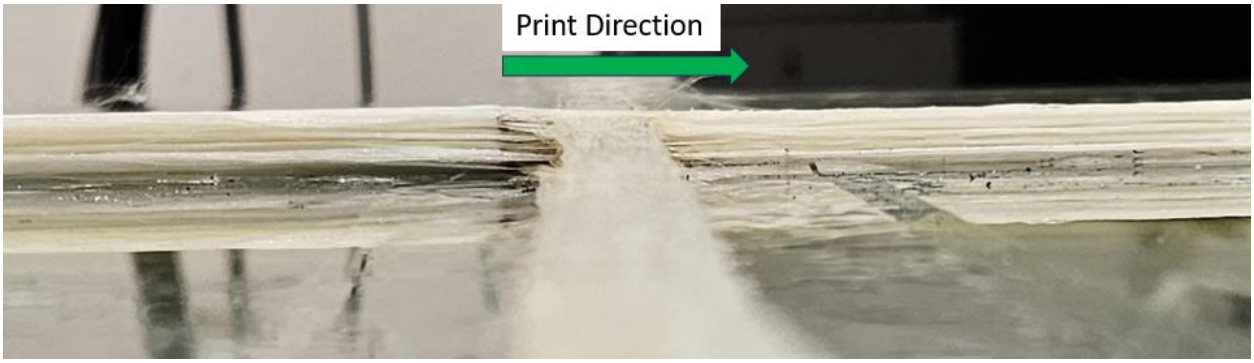

Figure 53: Thickness deviations before and after the crossover.

One resolution to this issue was found through observation of the tow spreading. It was noticed that the tow spread to a maximum width when the force setpoint changed from high to low which was programmed to occur. This can be seen in figure 55. Start indicates where the force increase began and stop indicates where the force setpoint from high to low.

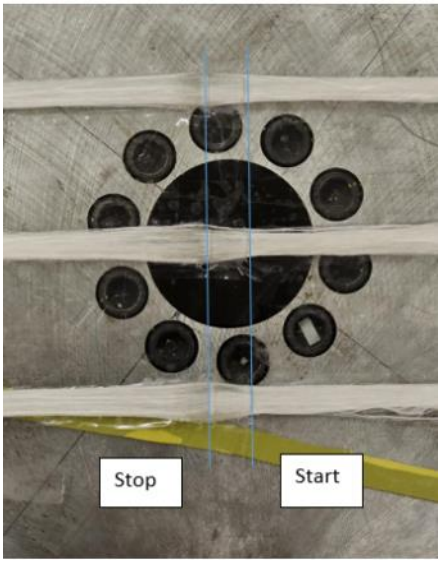

Figure 54: Tow thinning due to the force setpoint change.

To remedy this, the location of the force setpoint was shifted as seen in figure 55.

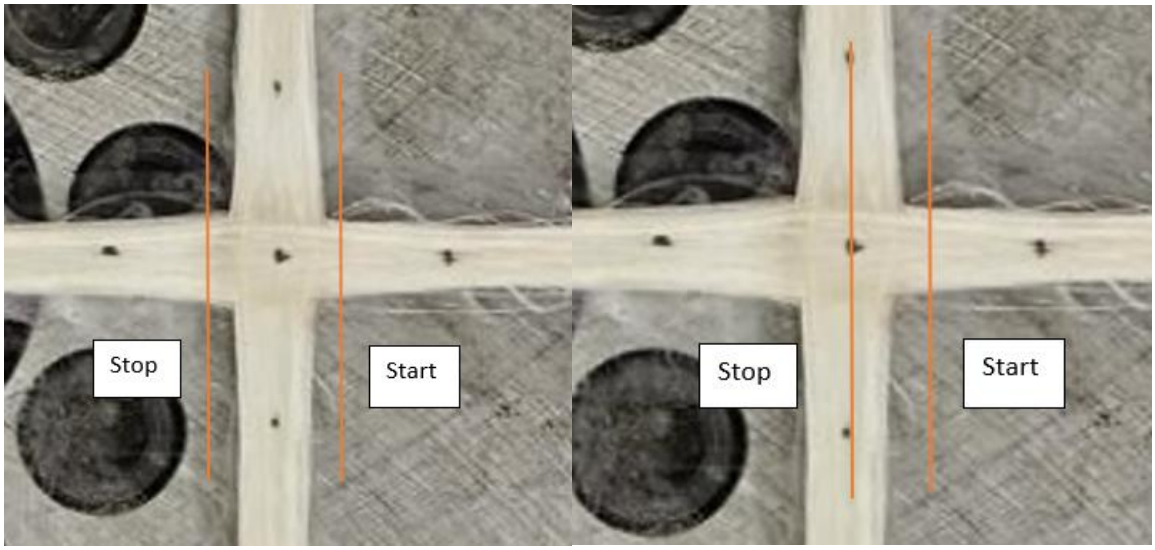

Figure 55: Original setpoint change (left) and shifted setpoint change (right).

With both the beams being optimized and the force setpoint change being shifted, the crossovers could be optimized using another Taguchi study.

5.1 Materials

The commingled tow feedstock used in this study is Compofil PP-60-R-1870N (Fiberglass Industries Twintex), a continuous E-glass/Polypropylene (EG/PP) untwisted commingled tow. The Tex of the roving is 1870. The unprocessed weight fraction of the reinforcement is 60%, which corresponds to a 35% fiber volume fraction. PP tape was placed on top of the glass build plate to improve the bed adhesion of the commingled tow and to maintain the as-printed position on the substrate. The unprocessed commingled tow width is approximately 6mm.

5.2 Experimentation

It is critical to have the height of the crossover and beam sections be the same height. The difference in height between the beam and the crossover can lead to out-of-plane fiber waviness which can negatively impact the strength of the structure. The purpose of these tests was to get the crossover thickness to match the programmed beam thickness. Again, the beam layer height was set at 0.15mm with the

number of layers in the beams set at 20. This results in a programmed layer height of 3mm. The parameters for the print were the same as those for the 450mm/min (7.5mm/s) optimized beams. These parameters were selected as they allowed the system to run in automatic mode with minimal intervention. The parameters were a roller temperature of 240C, no additional tension applied and the force setpoint for the beam sections was set to 3lbs.

5.2.1 Taguchi Design of Experiments

Optimization of the crossover prints was done using a small L4 Taguchi array. The parameters that were manipulated were the force at the crossover and the speed reduction at the crossover. A L4 Taguchi array was used for this study so only two levels of each parameter were investigated. The force levels were no additional force at the crossover and 25lb force at the crossovers. For the speed reduction, no speed reduction was the low value, and a 75% speed reduction was the high value. The orthogonal array can be seen in table 24.

Table 24: L4 orthogonal array.

Sample	Load Control	Speed Reduction	Interaction
1	1	1	1
2	1	2	2
3	2	1	2
4	2	2	1

The sample geometry used in this study is the same as the geometry used for the samples made in Chapter 3. This gives three crossovers per sample, allowing for an ANOVA to be performed, but also gives a direct comparison to the previous work done on crossovers. The geometry can be seen in figure 56.

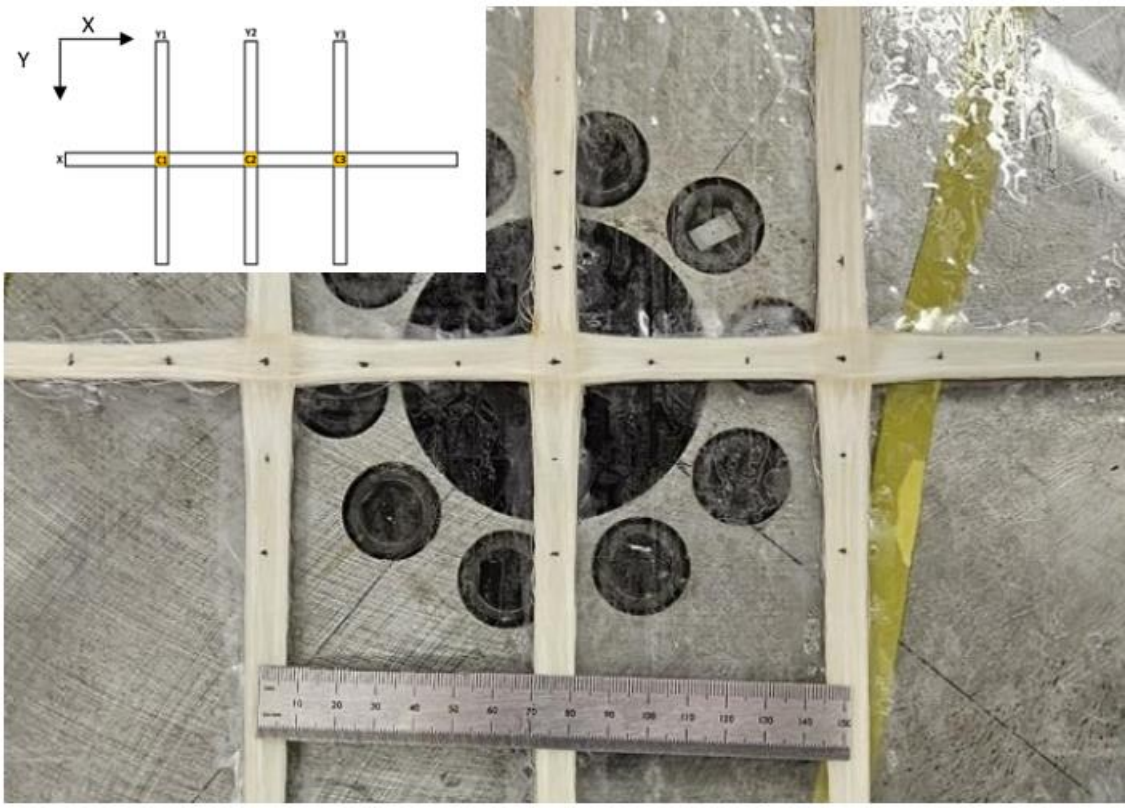

Figure 56: Example of crossover geometry.

The thickness of each sample was measured using a micrometer, at 25mm increments. Each location was measured 3 times. The quality of the fabricated parts was investigated by measuring the variation in the 20-layer height over the length of the straight beam (X, Y1, Y2 and Y3) sections as well as in the 40 layer crossovers (C1, C2 and C3), as shown in Figure 4. The black dots on the sample are the locations where thickness was measured.

For the analysis of the results in the orthogonal array, the data was not transformed in any way. In the previous study, the use of the S/N ratio and Grey's Relational Coefficient were not successful. While the thickness of beam sections were measured as well, these values were not used in the optimization; the thickness of the crossovers was optimization target.

Once the optimized parameters were found for the crossovers, two additional crossover samples were printed at the optimum beam parameters for 600mm/min (10mm/s) and 750mm/min (12.5mm/s).

These samples were printed to validate the optimized parameters, found from the Taguchi study, for the crossovers.

5.2.2 Void and Fiber Volume Fraction

A void and fiber volume fraction was done in order to determine the fractions of the constituent materials. For the void and fiber volume fraction analysis, the samples were sectioned, and the densities were found. An example of the sectioning can be seen in figure 57. The excess beam portions on the crossover sections were cut down to a minimum. This is done so that the results of the constituent material analysis accurately reflect the crossover sections and not a mix of the beams and crossovers. This can be seen in figure 58.

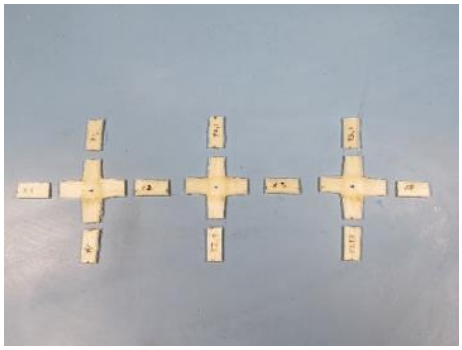

Figure 57: Example of section sample.

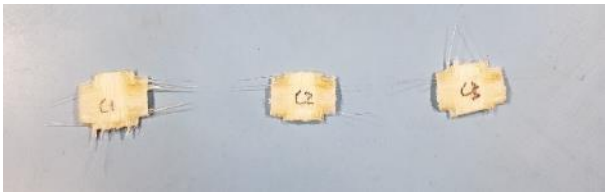

Figure 58: Example of crossover specimen for burn off testing.

The sectioning done matched that previously done in the original crossover study. The beam sections were nominally cut to 25mm in length. To determine the void volume fraction of a specimen, the Archimedes principle was used to find the density. To determine the volume of each specimen, the fluid displacement method, based on ASTM 792, was used [66]. RedLine Water Wetter was used, in a ratio of

32:1 deionized (DI) water to RedLine Water Wetter in order to minimize the bubble formation on the specimens and thus improve the accuracy of the measurement. To determine the weight fraction of fibers in each specimen, the matrix burn-off method was performed, according to ASTM D3171 [67]. The specimens are put in the furnace, in air, and the temperature is set to 547°C for at least 4 hours to ensure complete removal of the matrix. The loose fibers are then weighed, allowing determination of both fiber and void volume fractions through the use of manufacturer supplied densities. Only two of the crossover sections were used in the burn off analysis as one of the crossovers was sectioned a second time for the microscopic evaluation.

5.2.3 Metallographic Evaluation

Metallographic evaluation of the crossovers was done as a final evaluation. While the burn-off testing does provide a birds-eye view of the constituent materials and void contents, it excludes information about void size and locations within the laminate. One crossover specimen was harvested from each sample. The specimen was sectioned along the same plane for each parameter set. This can be seen in figure 59.

Figure 59: Example of sectioning used for microscopic evaluation.

5.3 Results

5.3.1 Taguchi Study and Optimization

The Taguchi study was done in order to optimize the parameters for manufacturing crossovers. As seen in Chapter 3, slowing the deposition speed allows the tow to spread and thin more. Similarly, increased force at the crossover also causes the tow to spread and thin more. Each crossover sample has three crossovers, each of which was measured three times. The results from the Taguchi thickness study can be seen in table 25.

Table 25: Crossover thickness results.

Sample	Load Control	Speed Reduction	Interaction	Y1 X-over (mm)	Y2 X-over (mm)	Y3 X-over (mm)	Total Ave (mm)
1	1	1	1	4.564	4.400	4.181	4.381
2	1	2	2	4.156	4.180	4.113	4.150
3	2	1	2	3.649	3.526	3.372	3.516
4	2	2	1	2.968	3.034	3.026	3.009

The target output for the crossovers is 3mm thickness, same as for the beams. Clearly, the parameters from sample 4, force increase and speed reduction, result in the best crossover geometry. The main effects table can be seen in table 26.

Table 26: Main effects table.

	Load Control	Speed Reduction	Interaction
1	4.265mm	3.948mm	3.695mm
2	3.262mm	3.579mm	3.833mm
Diff	1.003mm	0.369mm	0.137mm

Clearly, the changing force at the crossover (load control) has the largest impact on the crossover thickness while the interaction between the load control and speed reduction had little effect. The interactions graph can be seen in figure 60.

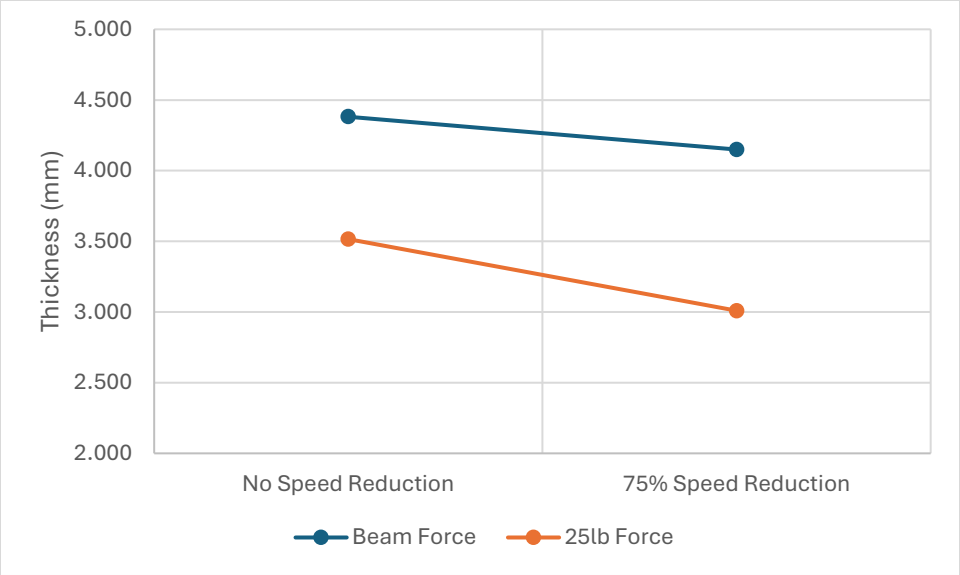

Figure 60: Speed reduction-force interaction graph.

The interaction graph can be interpreted by examining the difference in slope between the two lines. The greater the difference, the stronger the interaction and very strong interactions will intersect. From the interaction graph, little interaction takes place between speed reduction and increased force. This can also be seen in the ANOVA analysis in table 27.

Table 27: ANOVA analysis.

	f	Sum Sq.	Mean Sq.	F	Contribution (%)	P	Pcrit
LC	1	3.018	3.018	205.995	0.834	5.42E-07	0.171
SR	1	0.408	0.408	27.881	0.109	7.46E-04	
Interaction	1	0.028	0.028	1.928	0.004	0.202	
Error	8	0.117	0.015	1	0		
Total	11	3.600					

The critical P value for the null hypothesis to be true was 0.171; this means that for any P value less than the critical value, the null hypothesis is false and therefore the parameter is significant. From the ANOVA analysis, the interaction effects are seen to be insignificant as the P value is greater than the P crit value. Additionally, the ANOVA further supports the increased load control has a stronger influence on the crossover geometry than the speed reduction.

Clearly, having both the load control and speed reduction results in the most accurate (closest to 3mm) crossovers. To validate these parameters, two additional samples were printed. These additional samples were printed using the optimized parameters found for beams printed at 10mm/s and 12.5mm/s. The optimized parameters for the crossover points were held constant: a 25lb force setpoint at the crossovers and a 75% speed reduction at the crossovers. A comparison of the positional control (z-step) and the force control (current study) can be seen in Tables 28 and 29.

Table 28: Member by member comparison between positional control and force control of the crossover geometries.

	Positional Control					
		X				
		X Average (mm)	% Standard Deviation	Crossover Average (mm)	% Crossover Deviation	% Programmed Deviation
Speed (mm/min)	300	3.318	2.30%	3.482	4.93%	10.61%
	50	3.232	1.65%	3.182	-1.55%	7.73%
		Y1				
		Y1 Average (mm)	% Standard Deviation	C1 (mm)	% Crossover Deviation	% Programmed Deviation
Speed (mm/min)	300	3.197	3.82%	3.453	8.01%	6.56%
	50	3.162	4.22%	3.096	-2.08%	5.40%
		Y2				
		Y2 Average (mm)	% Standard Deviation	C2 (mm)	% Crossover Deviation	% Programmed Deviation
Speed (mm/min)	300	3.273	1.94%	3.517	7.45%	9.11%
	50	3.253	2.50%	3.214	-1.22%	8.45%
		Y3				
		Y3 Average (mm)	% Standard Deviation	C3 (mm)	% Crossover Deviation	% Programmed Deviation
Speed (mm/min)	300	3.272	1.97%	3.476	6.22%	9.08%
	50	3.227	1.92%	3.235	0.26%	7.56%

	Force Control					
		X				
		X Average (mm)	% Standard Deviation	Crossover Average (mm)	% Crossover Deviation	% Programmed Deviation
Speed (mm/min)	750	3.171	4.43%	3.211	1.27%	5.69%
	600	3.095	7.15%	3.217	3.93%	3.17%
	450	2.863	3.37%	3.001	4.80%	-4.55%
		Y1				
		Y1 Average (mm)	% Standard Deviation	C1 (mm)	% Crossover Deviation	% Programmed Deviation
Speed (mm/min)	750	3.113	4.25%	3.113	-0.01%	3.77%
	600	3.257	7.92%	3.273	0.51%	8.56%
	450	2.733	3.57%	2.968	8.58%	-8.89%
		Y2				
		Y2 Average (mm)	% Standard Deviation	C2 (mm)	% Crossover Deviation	% Programmed Deviation
Speed (mm/min)	750	3.333	9.82%	3.390	1.70%	11.10%
	600	3.184	7.06%	3.166	-0.55%	6.13%
	450	3.024	5.27%	3.034	0.36%	0.78%
		Y3				
		Y3 Average (mm)	% Standard Deviation	C3 (mm)	% Crossover Deviation	% Programmed Deviation
Speed (mm/min)	750	3.137	5.79%	3.139	0.09%	4.56%
	600	3.342	5.16%	3.216	-3.76%	11.40%
	450	2.811	4.19%	3.026	7.65%	-6.31%

Table 29: Global comparison between positional control and force control of the crossover geometries.

Load Control					
		Beam Average Thickness (mm)	Crossover Average Thickness (mm)	% Crossover Deviation	% Programmed Deviation
Speed (mm/min)	300	3.265	3.482	6.64%	8.84%
	50	3.218	3.182	-1.14%	7.28%
Force Control					
		Beam Average Thickness (mm)	Crossover Average Thickness (mm)	% Crossover Deviation	% Programmed Deviation
Speed (mm/min)	750	3.188	3.211	0.71%	6.28%
	600	3.219	3.217	-0.08%	7.31%
	450	2.858	3.001	5.01%	-4.74%

The crossover deviation represents the difference between the crossover and the average beam thickness, either by member, as seen in table 28, or by overall average as seen in table 29. The programmed deviation represents the average beam thickness deviation from the target of 3mm.

In general, these results are very promising as the crossover deviations of all force control samples were lower than the 300mm/min speed of the positional control samples. Further, the crossover deviations of

the 750mm/min and 600mm/min force control samples were lower than those of the 50mm/min positional control sample. It is surprising that the fastest two samples had the smallest deviations between the beams and the crossovers. Additionally, the average beam thickness of the load control samples was as good or better than that of the 50mm/min positional control sample. Despite the average thicknesses being as, or more accurate, the standard deviations of the load control samples were generally higher than those for the samples made using positional control.

5.3.2 Void and Volume Fraction

In addition to geometric evaluation of the samples, evaluation of the constituent materials was done as well. While not the primary optimization goal, examining the void and fiber volume provides useful information about the part quality and can be used in future optimizations. The summary of the void and fiber volume fraction analysis can be seen in table 30.

Table 30: Average void and fiber volume fraction analysis from crossover optimization study.

		X		Y1		Y2		Y3		Beam		Crossover	
		Average	SD	Average	SD	Average	SD	Average	SD	Average	SD	Average	SD
None	Fiber Volume Fraction	32.30%	0.91%	31.93%	0.09%	31.75%	0.79%	32.69%	0.04%	32.19%	0.75%	31.67%	1.09%
	Void Volume Fraction	8.47%	1.65%	9.47%	0.03%	10.26%	1.89%	7.81%	0.35%	8.90%	1.60%	11.13%	2.20%
Speed Reduction	Fiber Volume Fraction	32.75%	1.01%	32.85%	0.51%	32.64%	0.87%	32.94%	0.43%	32.79%	0.81%	33.11%	0.33%
	Void Volume Fraction	7.80%	2.30%	7.61%	0.87%	7.78%	1.46%	6.97%	0.80%	7.59%	1.71%	6.77%	0.72%
Load Ctrl	Fiber Volume Fraction	32.83%	0.90%	33.70%	3.41%	32.69%	0.36%	32.69%	0.02%	32.95%	1.68%	32.58%	0.61%
	Void Volume Fraction	6.21%	1.67%	8.54%	1.20%	7.14%	1.33%	7.10%	0.02%	7.04%	1.58%	8.63%	1.10%
Both	Fiber Volume Fraction	33.20%	0.76%	32.84%	0.30%	32.80%	0.51%	33.26%	0.20%	33.06%	0.59%	36.95%	1.24%
	Void Volume Fraction	6.22%	1.99%	6.98%	1.41%	7.92%	1.28%	6.03%	1.37%	6.67%	1.78%	6.59%	0.59%

In general, the beam sections from these samples show higher void contents than the previous crossover study using positional control. This is most likely due to the lower roller temperature and higher deposition speed. In comparing table 25 with table 30, it appears that the beam void content does decrease with decreasing crossover thickness. However, upon further examination, the standard deviations of the void contents of the beam sections do overlap as seen in figure 61.

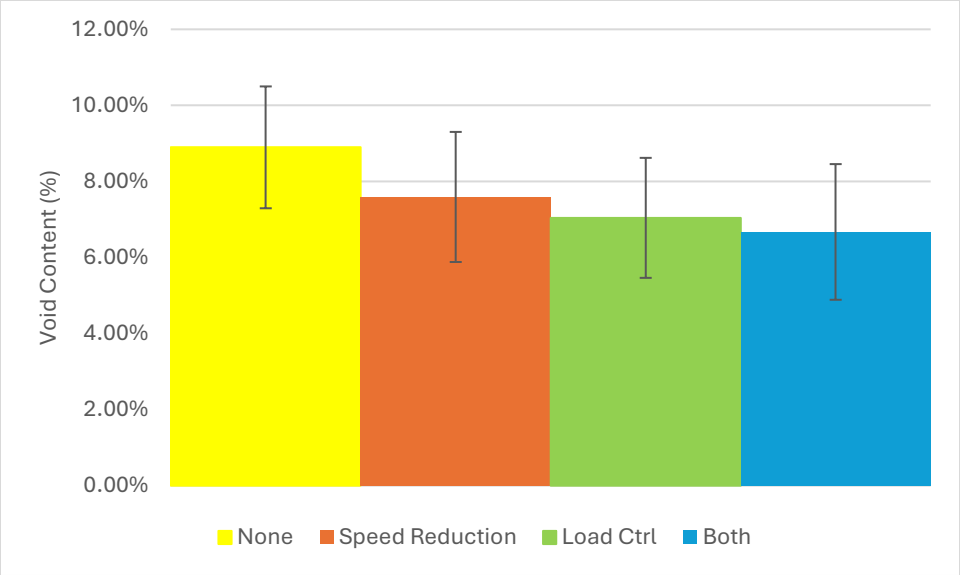

Figure 61: Beam void content comparison Lower is better.

Similar to the previous crossover study, the crossover void content decreases with decreased speed. This is also supported by the trends seen in the beam optimization study where decreased speed had a more significant impact on the reduction of voids as compared to increased force. The void content of the crossovers is summarized in figure 62.

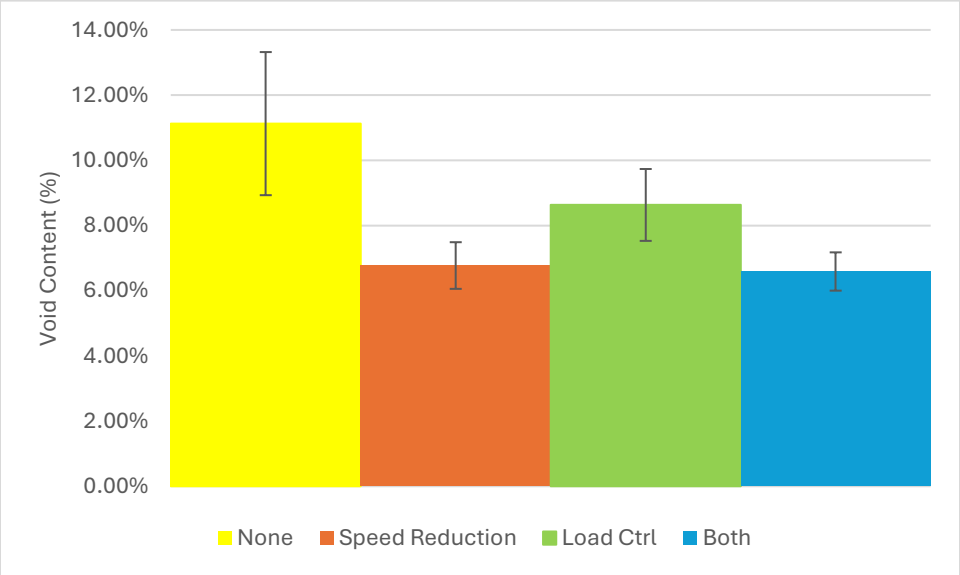

Figure 62: Crossover void content comparison. Lower is better.

All samples had relatively high void contents as all were more than 6.00% voids. This could be due to the "optimized" print parameters found for the 7.5mm/s (450mm/min) speed. As discussed previously in Chapter 4, the temperature was the most influential parameter on the void content and the lower temperature of the roller (240C) results in a higher void content. Clearly, the two samples with reduced speed at the crossovers had the lowest void content. Increasing the force at the crossovers did reduce the voids as compared to doing nothing; however, the increased force seemed to have little impact when comparing the speed reduction sample to the sample with both effects applied. This indicates the diminishing returns of the force increase to control void content.

5.3.3 Metallographic Evaluation

The final analysis done for this study was microscopic analysis. Images of all the left half of all crossover specimen can be seen in figures 63-66.

Figure 63: Crossover cross section of baseline sample (None).

Figure 64: Crossover cross section of speed reduction sample.

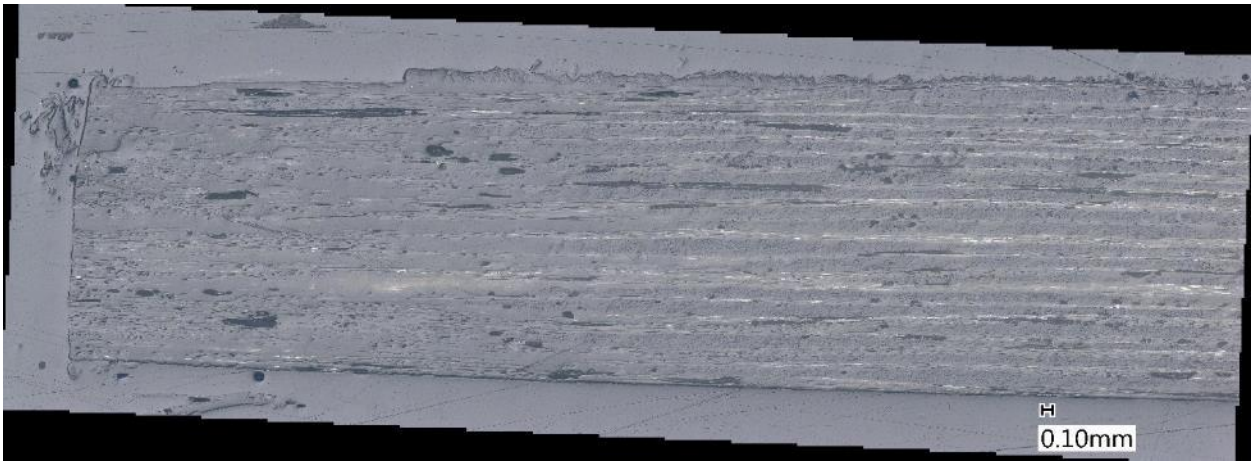

Figure 65: Crossover cross section of load control sample.

Figure 66: Crossover cross section of sample with both effects applied.

The fibers can be recognized in three different forms due to the sectioning: circles, rods and ellipses. The fibers that appear as circles are perpendicular to the sectioning plane as one would expect to see when looking at a 0° composite. The fibers that appear as rods are running parallel to the sectioning plane as one would expect to see when looking at a 90° composite. The fibers that appear as ellipses are at some angle coming out of the sectioning plane between the other two orientations. This indicates the in plane bending that is occurring when the tow is spread.

It should be noted that what look like voids of the same shape and orientation as these spread fibers, are most likely an artifact of the polishing process. As the fibers are cut at a shallower and shallower angle, the longer and longer the elliptical cross section becomes. Because the fibers are significantly harder than the matrix, the matrix is ground away at a faster rate during the polishing. This causes the reinforcing fibers to protrude slightly from the surface. The polishing media builds up on one side of the fibers as a result. Because of the large cross-sectional area of these angled fibers, this build up gives the impression of a large number of voids, but this is not the case. This can be seen in figure 67.

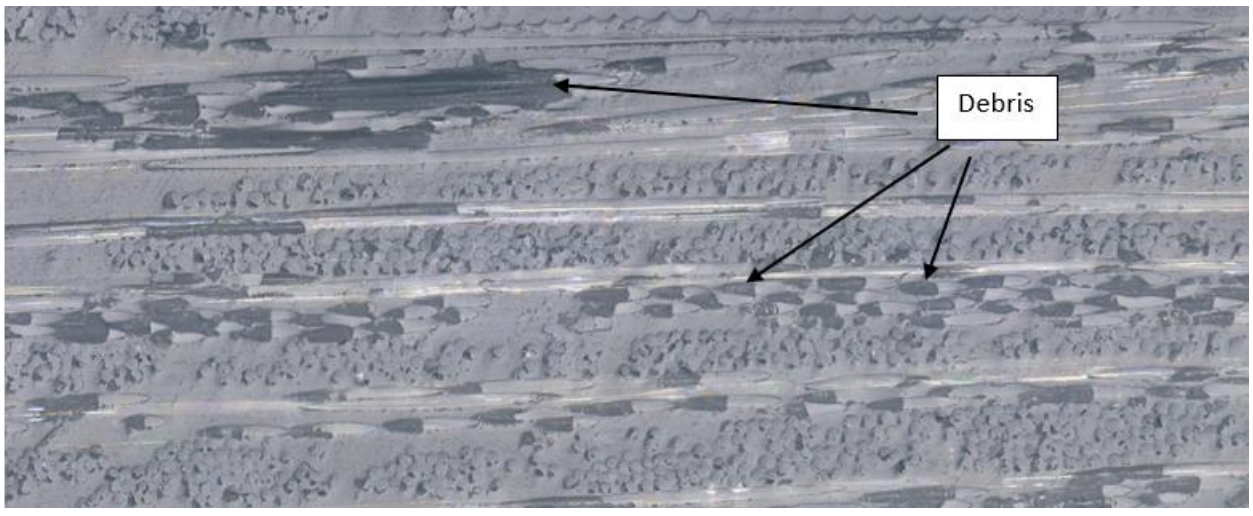

Figure 67: Polishing debris build up on fibers.

5.4 Discussion

From the Taguchi study, the increased force had the largest impact on the crossover geometry; this is consistent with the previous Taguchi study on beams where force had the strongest influence over the beam thickness. Similarly, from the burn off results, slowing the deposition speed had more of an impact on the crossover void content than the change in force. This was also indicated in the burn offs done on the beams. In that study, the speed had the second strongest influence on the beam void content while increased force had the smallest influence.

For the thickness control, the average beam thicknesses using the load control were comparable to, or better than, the values obtained from the 50mm/min positional control sample evaluated in Chapter 3. The average beam thicknesses for the load control samples were 3.188mm, 3.219mm and 2.858mm for the 750mm/min, 600mm/min and 450mm/min samples, respectively. The average beam thickness for the positional control sample printed at 50mm/min was 3.218mm. The target thickness for all samples was 3mm. This is a very promising result as the load control samples were printed between 9x and 15x faster than the 50mm/min sample. Additionally, the crossover average thickness of the load control samples was again comparable or better than the 50mm/min positional control sample. The percent crossover deviations were also better for two of the load control samples as compared to the 50mm/min positional control sample. The 750mm/min and 600mm/min load control samples had % crossover deviations of 0.71% and -0.08%, respectively. The 50mm/min positional control sample had a % crossover deviation of -1.14%. However, the samples made using the load control method did generally have a higher standard deviation than the samples using positional control. This can be seen in comparing the X direction standard deviations in Table 28. The largest standard deviation of the positional control method was 2.30% deviation from the 300mm/min sample while the smallest standard deviation of the load control sample was 3.37% from the 450mm/min sample. Changing the speed clearly has an impact on the standard deviation of the beam thicknesses; using the positional

control method, increasing the speed from 50mm/min to 300mm/min caused the standard deviations to increase from 1.65% to 2.30%, respectively. The load control samples did not follow this trend, as the highest standard deviation was from the 600mm/min sample with 7.15%. This suggests that the deposition speed has influence over the deviation of the thickness. However, at higher speeds the standard deviation of the samples is influenced more by other parameters such as temperature.

In terms of the void content of the beam sections, the general trend appears to be that as the crossover thickness decreases, the void content in the beams also decreases. However, due to the high standard deviation in the specimen, this observed trend is not validated. The expected trend for the beam sections is that there is no trend; because the beam sections used in the testing were far from the crossover point and the print parameters were the same for all beam sections, it is expected that the void content is the same from all the beams. This is the trend that is shown in the burn off testing, indicating the transients induced by the change in print parameters have been resolved within 25mm of the crossover. To be clear, this is only in regard to void content within the beams.

For the void content in the crossover sections, unsurprisingly there was an influence of the changing print parameters on the void content. The only definitive trend is that as the roller slowed, the void content was reduced. The addition of more force does appear to have an impact, but the overlapping error bars of the baseline (None) and the Load Ctrl make it difficult to verify this trend. In the positional control study and the beam optimization study the deposition speed did have a clear impact on the void content of the specimen. Slowing the deposition speed in both previous studies resulted in a reduction of voids; this is due to the tow being in the heated zone, under the heated roller, for a longer duration. The effect of this slowing is twofold: the plastic gets heated to a higher temperature, reducing the viscosity of the matrix, and the matrix is under pressure for a longer period of time, allowing for more flow to occur. Additionally, in the beam optimization study, it was found that force had the smallest impact on void volume fraction out of the examined parameters. This was attributed to the high matrix

viscosity at lower roller temperatures/speeds being a significantly more dominate factor than the applied force. The influence of the deposition speed and the lack of influence of the increased force on the void content is further supported by this study.

One of the assertions made in the positional control study was that the higher void content in the crossover sections was due to fiber bridging as the tow transitioned from the beam to the crossover and vice versa. Microscopic analysis was not done in this original study, which could have given greater insight. In the present study, this microscopic analysis was done to determine the influence of the crossover height and process parameters on the presence of voids in the transition region between the crossover and beams. It was determined that the transition regions have more voids, particularly when the crossover is thicker than the beam.

As mentioned previously, there is a buildup of polishing debris on the fibers. At first glance, these appear to be voids but are not; many of the voids appear to be filled with the polishing mount material. This is most obvious in figure 68. On the left side of the image, an open cavity can be seen which is full of the mount material; the mount is a slightly lighter shade of grey than the matrix material. Additionally, a boundary can be seen between the different materials.

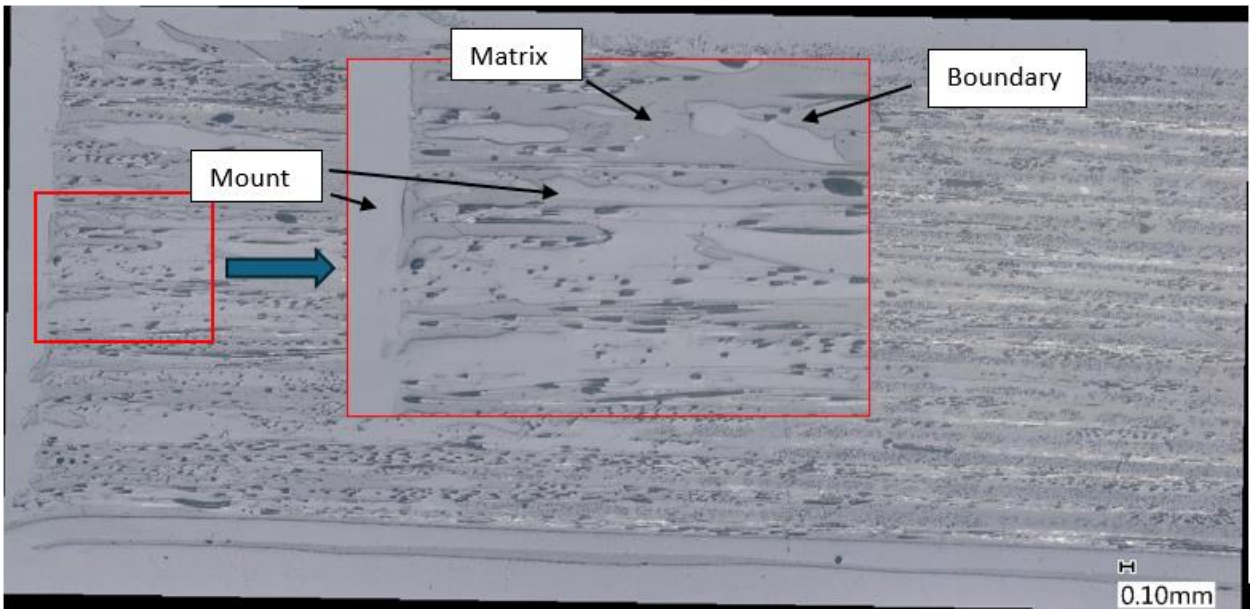

Figure 68: Mount material captured within voids.

Generally, the fiber distribution is significantly better in the specimen with both force and speed effects applied compared to the specimen without either effect applied. This is not surprising as in the burn off testing, the fiber volume fraction increases from 31% to 36% when comparing the specimen with no effects applied to the specimen with both effects applied. Two representative images from the respective specimen can be seen in figures 69 and 70.

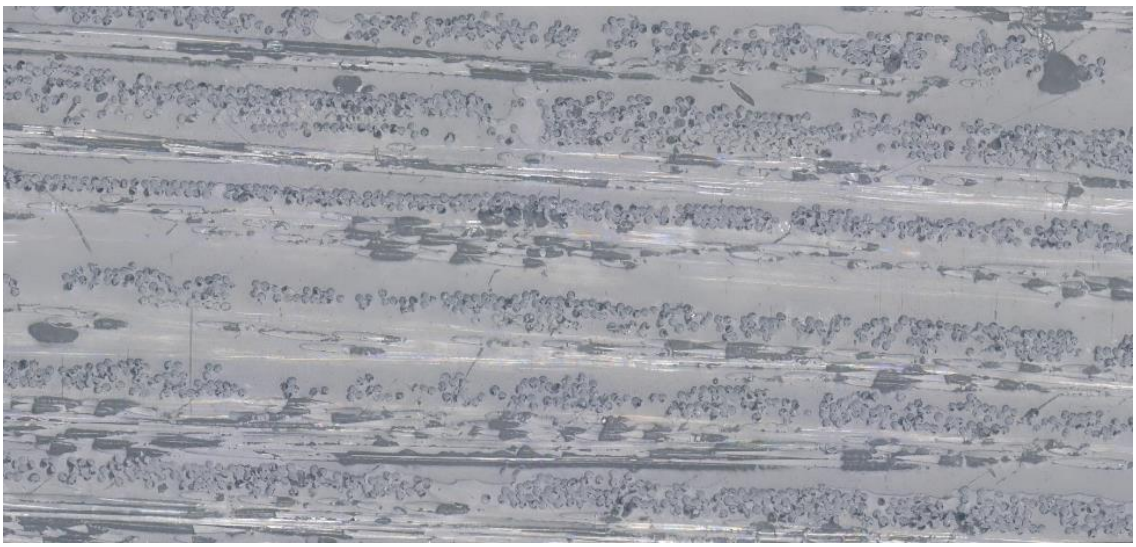

Figure 69: Fiber distribution with no effects applied. Image taken from the center of crossover.

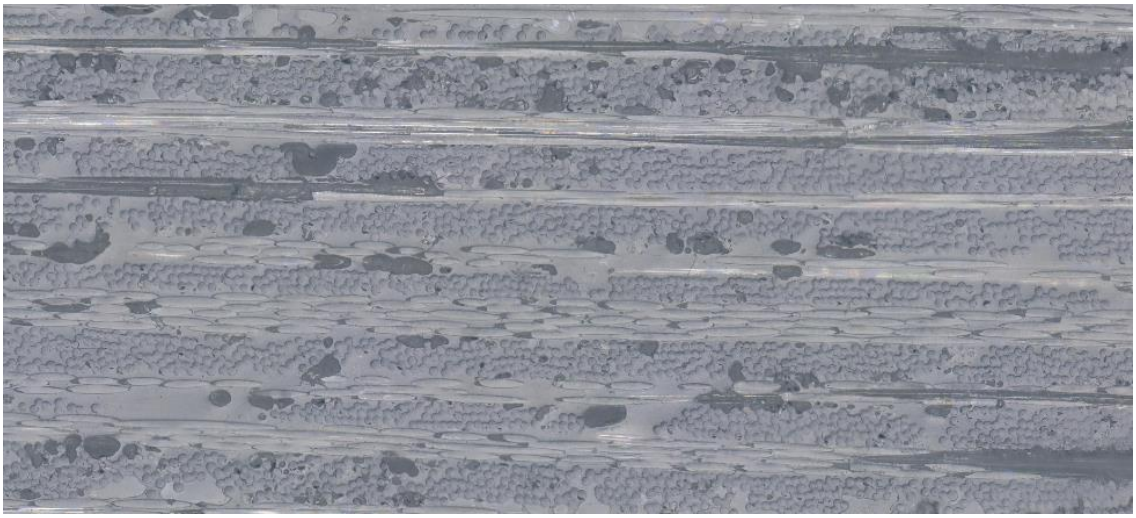

Figure 70: Fiber distribution with both effects applied. Image taken from the center of crossover.

Without any effects applied, there are clearly large matrix rich regions, especially in between the layers. This makes sense considering the higher fiber volume fraction of the specimen with both effects applied as well as the thinner geometry of the specimen. This, again, is due to the matrix being able to flow more easily, experiencing a larger pressure gradient and experiencing the pressure gradient for a longer period of time.

Visual examination of the transition between ply directions was necessary to determine if a higher concentration of voids exists in this region. The noteworthy observation is that the fiber volume fraction does decrease, and resin rich areas increase as the specimen transitions from crossover to beam regions. This can be seen in figure 71; the higher fiber volume fraction area is on the right side of the image whereas the resin rich area is on the left side of the image. This is the transition region where fiber bridging, and subsequently voids, is likely to occur.

Figure 71: Fiber volume fraction gradient in specimen without any effects applied.

The center of the crossovers have relatively few voids as seen in figures 69 and 70. This is not surprising as even with no effects applied, the crossover gets processed twice as much as the beam sections. Examination of the transition region between the two different ply directions reveals an increased number of voids. Moving further along the specimen into the beam section, the voids continue to increase. This can be seen in figure 72. The number of voids increases from right to left of the image. This corresponds to the center of the crossover and the beam section, respectively. This increase in void content does support the idea that the transition region contains more voids than the center of the crossover or the beams. Additionally, qualitatively, it appears that the sample with both the speed reduction and the increased force has significantly fewer voids in the adjacent beam than the other specimen. One explanation for the lower void content in the adjacent beam is the lack of fiber bridging. Fiber bridging, as described in Chapter 3, is the phenomena that occurs when the fibers fail to conform to a sharp contour. In continuous fiber grid stiffened composites, this can occur at the crossover points using traditional manufacturing methods. Because there is twice as much material at crossover points, the intersection is thicker than the beam. As the tow transitions from the beam to the crossover, and vice versa, tension in the fibers prevents the tow from conforming to the change in geometry. This can be seen in figure 72.

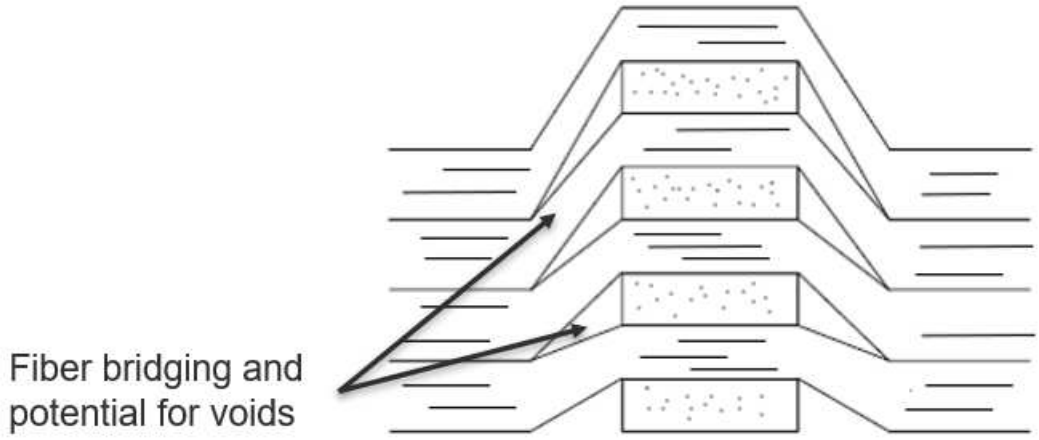

Figure 72: Depiction of fiber bridging and location for potential voids.

The fibers “bridge” the transition between the beam and the crossover. This bridging causes a lack of consolidation in this transition region which, in turn, results in a resin rich pocket. The lack of consolidation in this region also fails to push the voids out. The sample with both effects applied also had the lowest average crossover height. The flatter geometry would reduce the amount of fiber bending through the thickness, reducing the amount of fiber bridging. This can be seen by comparing figures 73 and 74.

.

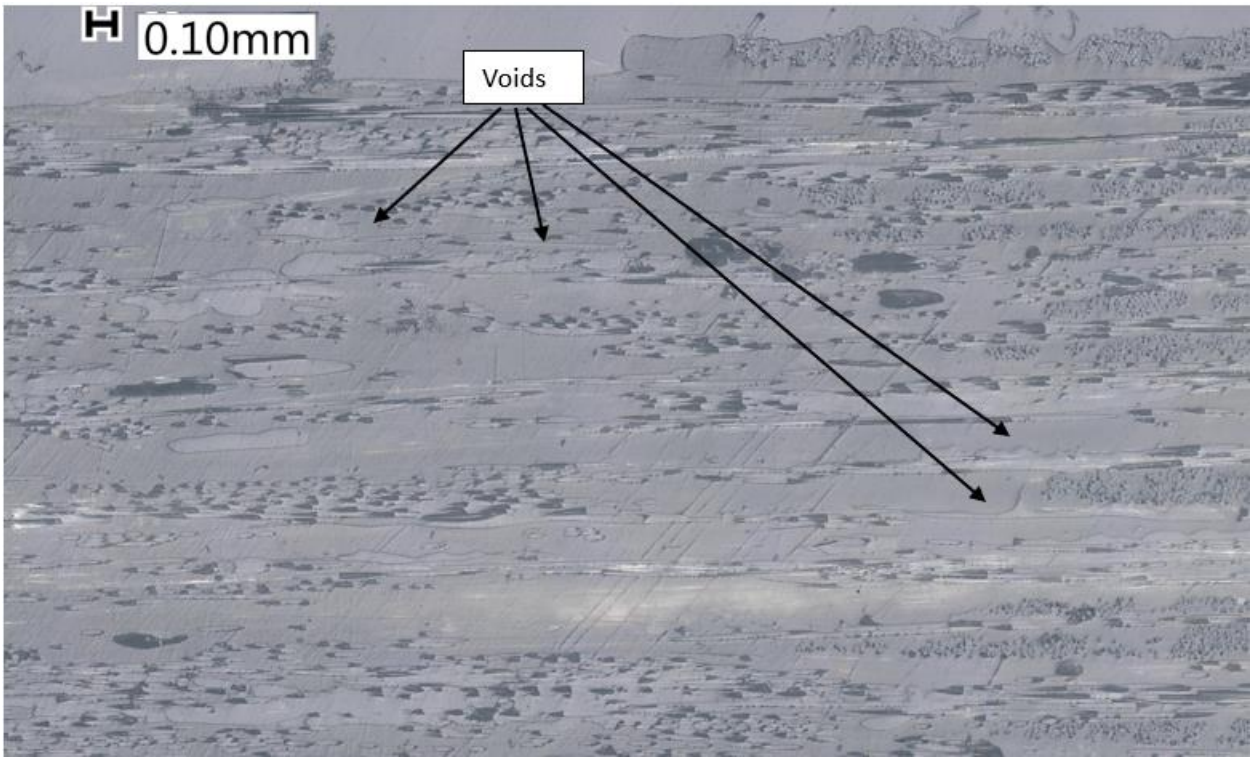

Figure 73: Increase in voids, from right to left in specimen with load control applied. Concentration of voids at crossover transition can also be seen.

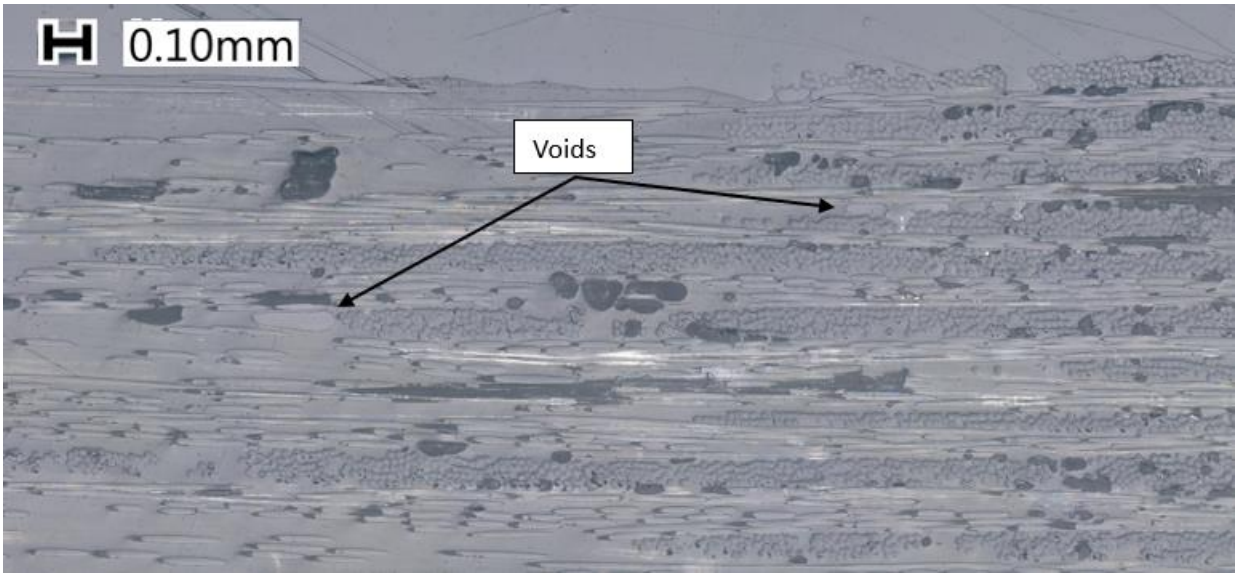

Figure 74: Voids at crossover transition for specimen with both effects applied.

5.5 Conclusions

This study has proven that using the system developed, consistent crossover geometries can be printed at three different speeds, 450mm/min (7.5mm/s), 600mm/min (10mm/s) and 750mm/min (12.5mm/s). These were achieved through the manipulation of two variables: the force and speed at the crossovers. By increasing the force and decreasing the deposition speed at the crossovers, the tow was effectively thinned and spread so that there was a minimal amount of material build up. Similar to beam optimization, the increase in force had the largest impact on the geometry of the crossover. The optimized parameters for the crossovers were found to be an increase in force from the beam force setpoint to 25lb and a speed reduction of 75%; three samples were printed using the parameters found in this study and the parameters determine in the beam optimization study for the three different speeds. These samples were then compared to the positional control samples printed in the initial system comparison study. The samples using force control were closer to the target thickness than the positional control samples. However, there was less thickness variation in the positional control samples. Additionally, void and volume fraction measurements were taken on the beams and crossovers of the samples used in the optimization study. Again, similar to the beam optimization, the speed reduction had a larger impact on the void content of the crossovers as compared to the force increase. The slower speed of deposition allowed the matrix to heat more, decreasing the viscosity and reducing the voids Finally, microscopic images were taken of the crossover sections used in the optimization study. It was found that the thicker the crossover sections had a greater number of voids in the transition regions between the beam and the crossover. This was due to a large amount of out of plane fiber bending and subsequent fiber bridging that occurs in the samples with thicker crossovers. The fiber bridging results in resin rich areas at the transitions which allows for voids to be entrained in these areas.

CHAPTER 6: FUTURE WORK

6.1 Shoe Beam Development and Testing

Previous work done at the CMMS using the commingled tow has always noted a “flash” or resin rich region at the edges of the tow. This not only results in rough, visually unpleasing sides of the composite, but also results in high void content in the resin rich region. This is well demonstrated in figure 75.

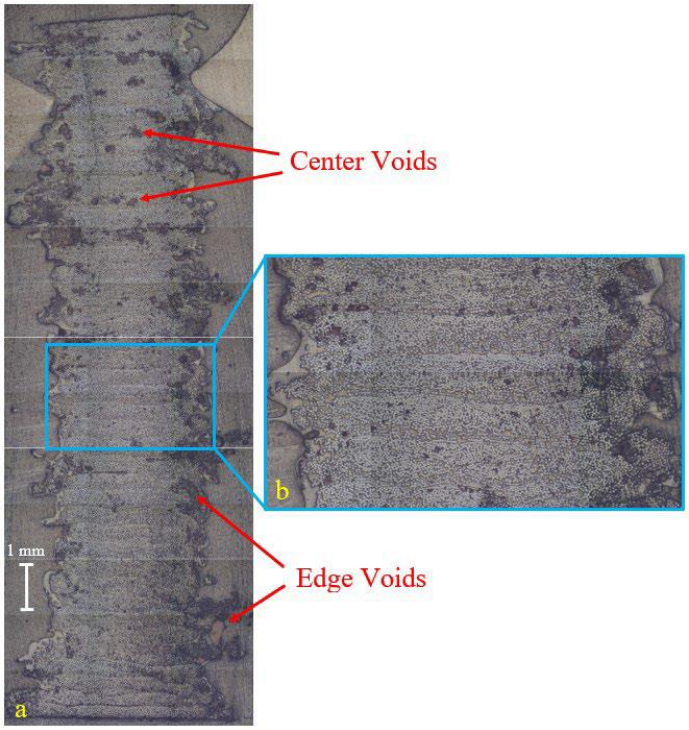

Figure 75: Flash and voids on the edges on high aspect ratio beam [50].

This is assumed to be a result of the sides of the tow not being molded; the top and bottom surfaces are molded either by the placement system (nozzle or roller) and by the substrate (previous layer or build plate), respectively. Because there is no constraint on the sides of the deposited tow, there is a pressure gradient along the width of the tow. The pressure is at a maximum in the center of the tow and drops to atmospheric pressure at the tow edge. The side walls could be molded as a separate operation after deposition, however, due to the concern about the voids entrained in the sides, the constraint of the tow

must be done in-situ. The difficulty of consolidating in-situ is that the side molds must extend to or past the top of the previously deposited tow. However, if the side walls are rigidly fixed and extend past the top of the previously deposited tow, there has to be some amount of thickness already built up on the build plate surface for the top of the tow to be consolidated. This would suggest that the side walls have to be able to move somewhat independently from the nip of the placement head (nozzle or roller). While it may be possible to implement a molding solution on the nozzle-based systems, the 3-axis control of these systems is not sufficient for making complex geometries; rotation about the z-axis is necessary if anything other than single direction beam are to be made. As a result, the conception of this system was done knowing it would eventually go on a roller-based with 6-axis capabilities.

6.1.1 System Design

After determining the system was going to utilize the deposition roller, the next issue was determining how the molding shoe was going to actuate. The molding shoe needed to not only actuate down but also up; this would allow for the system to print crossovers, which is the emphasis of the previous work done. One concept was to use a linear stepper motor, similar to the one used to actuate the consolidation roller up and down for the force control system, albeit much smaller. One issue with this concept was attempting to package the actuator into the current deposition head. This method would allow precise control of the molding shoe height relative to the deposition roller; this brought forward a question: how accurate does the positional control of the shoe height need to be? The conclusion that was reached was that as long as the bottom of the shoe extended past the top of the previous layer by two- or three-layer thicknesses, then it would not make a difference to the part quality. Additionally, if the shoe ran into the build plate and ran along it, it would not be an issue either. As such, the actuator that was selected was a small air actuator. The small packing of the air actuator would make overall attachment and packaging into the current system easier. Further, the required force output from the actuator was assumed to be small, which this actuator met. A minimal force is assumed as the friction

from the matrix on the up and down actuation of the shoe was assumed to be low. From previous testing, the matrix acted as a lubricant when heated to print temperatures and was assumed to "lubricate" the shoe during the actuation up and down.

With the actuator selected, the design of the rest of the system and packaging could be done. One of the goals of this system was to not only mold the side walls of the beams but to also increase the aspect ratio of the beams. Using roller deposition, the tow was spread and thinned significantly more than nozzle deposition; this was highlighted previously in work done comparing the two systems in Chapter 3. The tow width using the roller was about 12mm while the unprocessed commingled tow had a width of approximately 6mm. Because of this, the target width of the beams was selected to be 8mm. This would allow some spreading but would still result in a beam with a higher aspect ratio. With this width selected, the roller and shoe width was set. The heating method for this design was the same as for the roller-based system without the shoe: using cartridge heaters in the axle that runs through the roller. Similarly, the same IR thermometer was used for this system as well. The intent behind this design was to use the force control system developed in combination with the shoe; as a result, the shoe assembly needed to be attached to the linear stepper that varied the position in the consolidation roller. The resulting shoe assembly can be seen in figure 76.

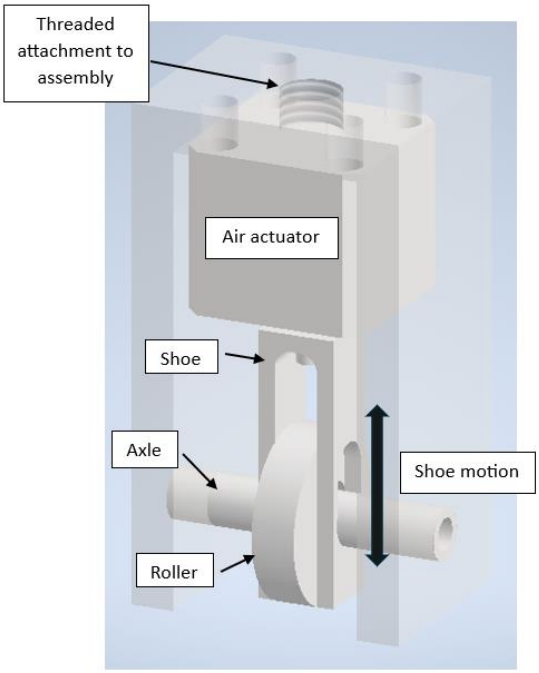

Figure 76: Shoe assembly.

6.1.2 System Concerns

One of the main concerns with this design was the proximity of the air actuator to the heated roller. The maximum temperature rating for the air actuator was 80C. Because of this concern, some rudimentary testing was done to determine what temperatures were possible with this system. The air actuator was removed, and cartridge heaters were installed in the axle. The temperatures at two different locations were taken. The two locations were at the top of the whole assembly and at the top of the shoe itself, where it attaches to the actuator shaft. The locations of the temperature measurement can be seen in figure 77.

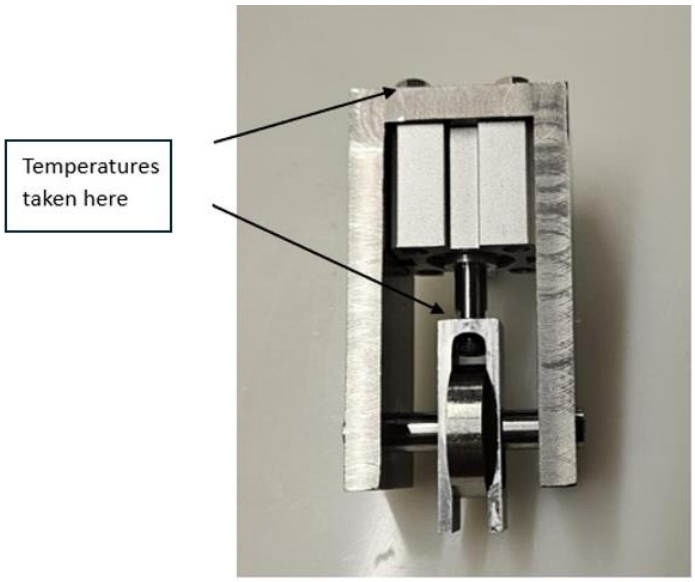

Figure 77: Temperature probing locations.

The roller was heated to 250C and the assembly, without the actuator, was left to sit until the temperatures at the measurement locations reached steady state. The top of the assembly reached a high temperature of 120C, and the top of the shoe reached a high temperature of 200C. Clearly, for anything other than preliminary testing, some type of cooling needs to be applied to the air actuator if it is to be used in a final design. Alternatively, the actuator could be positioned in a more remote location, isolated from the heated roller.

Another concern was keeping the tow under the roller. Some amount of clearance has to exist between the roller and the shoe if the two are going to move independently. This clearance is a location for the glass fibers to become entrapped, between the roller and shoe. Finally, the main impetus for moving to a roller-based system was so that a cut and refeed system could be implemented. While the cut and refeed system works well, there are some issues with it. For instance, the consolidation roller is significantly wider than the tow; this is to compensate for the tow not refeeding perfectly under the roller. In the shoe design, the consolidation roller and shoe are much narrower than in the previous design, just slightly wider than the tow. As a result, there is no tolerance in the design to compensate for the tow

being fed at a slightly askew angle. This was assumed to create problems for refeeding the tow under the roller.

6.2 Shoe System Testing

Due to the concerns about the design, some preliminary testing was initiated.

6.2.1 Materials

The commingled tow feedstock used in this study is Compofil PP-60-R-1870N (Fiberglass Industries Twintex), a continuous E-glass/Polypropylene (EG/PP) untwisted commingled tow. The Tex of the roving is 1870. The unprocessed weight fraction of the reinforcement is 60%, which corresponds to a 35% fiber volume fraction. PP tape was placed on top of the glass build plate to improve the bed adhesion of the commingled tow and to maintain the as-printed position on the substrate. The unprocessed commingled tow width is approximately 6mm.

6.2.2 Experimental Setup

The geometry for the testing was just a simple beam; this could demonstrate some functionality without the need for a 5/2 pneumatic valve. For this testing, the shoe was actuated in the down position the whole time. The extended actuator acts as a constant force compression spring which compensates for the change in roller height off the build surface. The installed system can be seen in figure 78.

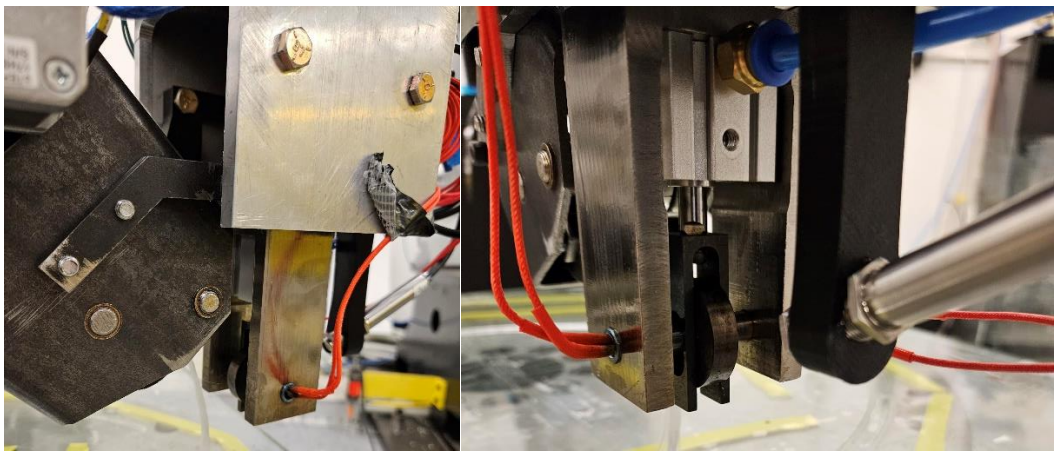

Figure 78: Installed shoe system.

All the parameters for this testing were the same as the 7.5mm/s optimum beam printing parameters. The temperature setpoint was 240C, the print speed was 7.5mm/s, the layer height was 0.15mm, the force setpoint was 3lb, and no tension was applied. The force setpoint accommodated the reaction force from the air actuator. Because there was a reaction force from the shoe/actuator contact with the build plate, the force setpoint was set higher than for previous prints. The result was that the force applied on the tow matched the 3lbs used in previous testing at this speed.

6.2.3 Results

While the manufacturer specified upper use temperature of the actuator is only 80C, there were no obvious issues with air actuator during the testing. The push-on connector, however, did fail. While the temperature of the air actuator was not measured during the testing, previous testing determined the bolted connection between the shoe housing and the actuator got up to 120C when the roller was heated to 250C. During this testing, the roller setpoint was 240C.

The first issue with the system was heating the roller. Despite letting the system heat for more than 10 min, the roller only reached ~200C; this was verified with the IR thermometer and a separate thermocouple. In previous testing, the roller was able to heat up to 250C, but this was done without the air actuator installed. Most likely, the heat transfer to the roller was limited by the installation of the air

actuator. The shoe itself was turning a blueish hue (~250C) due to the temperature it reached; this indicates the high temperature reached by the shoe but not by the roller. This indicates that the heat was transferring into the system as a whole but not to the roller. Additionally, in the previous testing, the measured temperature at the interface between the shoe and the actuator shaft was ~200C.

Refeeding was another issue with the system. While the cutting was automatic, the tow had to be manually pulled under the roller, in between the shoe. Because the shoe was only in the down position, fibers would get trapped under and severed by the shoe.

However, the biggest issue with the system was when fibers got caught between the shoe and the roller. This issue can be seen in figure 79.

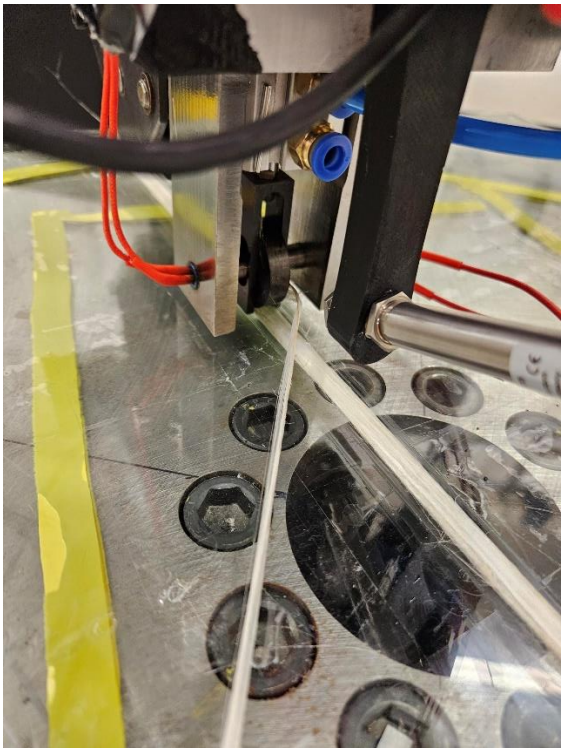

Figure 79: Tow getting caught between shoe and roller.

The beam printed had only 5 layers actually deposited and can be seen in figure 80.

Figure 80: Printed beam.

The shoe did help to constrain the tow width as seen in figure 81.

Figure 81: Controlled tow width.

6.2.4 Metallographic Evaluation

The printed beam was also sectioned and mounted for metallographic evaluation. This was critical for this sample as the shaping or constraint of the sidewalls was the main driving force behind this hardware change. This can be seen in figure 82.

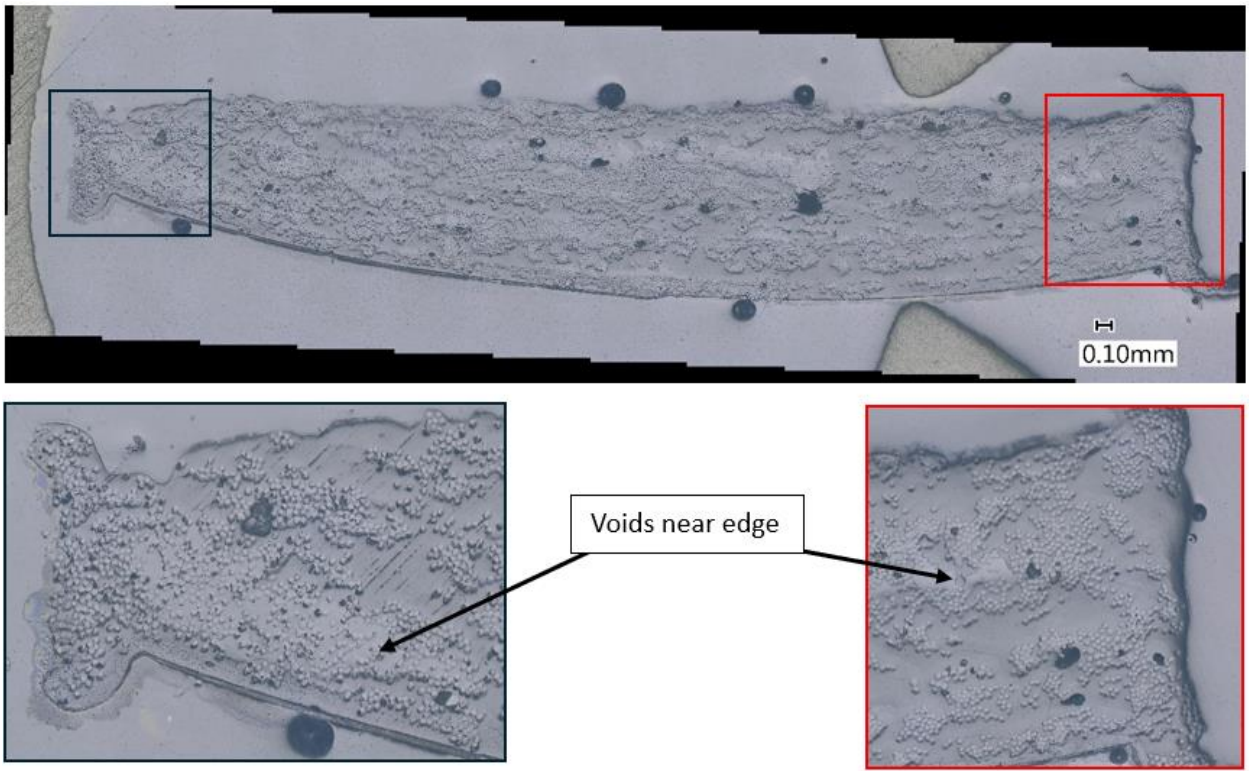

Figure 82: Printed shoe beam cross section.

Large regions of voids exist in this sample, primarily due to the low temperature of the roller. It is assumed that these voids exist on the bottom side of the tow as the heat transferred from the roller, down through the tow, into the previous layer. If the roller is not hot enough, not enough heat will be transferred to get good inter layer fusion.

Overall, the shoe did help to constrain the tow as seen in figure 83. This is especially noticeable on the right side of the image. It is difficult to determine if this caused reduced voids at the edges of the tow; in the previous roller deposition testing, there was not a concentration of voids at the tow edges. Unlike

with nozzle deposition, there were no large resin rich “flash” regions at the edges of the cross-section. As a result, there were no large regions of voids at the edges in sample printed without the shoe. So the absence of voids at the edges of the tow may be due to the use of a roller and not necessarily a result of shoe.

6.3 Shoe Future Work Recommendations

In terms of the functionality of the shoe system, the main issue was the roller and shoe being two separate pieces. The clearance between the shoe and the vertical side of the roller allowed for fibers to be entrapped in this gap. This effectively pultrudes a “rod” in the air as seen in Figure 6, which is clearly undesirable. If the shoe and roller could be combined into a single piece, i.e. such as a grooved roller, this issue would be eliminated. While a grooved roller could control the tow geometry on the beam sections, it would not allow for the tow to spread at the crossovers.

Previously, it had been noticed that the roller can fail to roll when depositing the tow, especially at higher temperatures. This does not, however, cause an issue with deposition. The roller manages to slide along the tow and does not damage the tow in any way. It is assumed that the high temperatures drop the viscosity of the plastic so much that the polymer effectively acts as a lubricant between the roller and the tow. While this is not ideal, it does provide an interesting solution to the shoe design.

One idea how to solve this issue is to have a grooved roller but either the roller or the groove is shaped similar to a cam and to control the rotational position of the roller. Given that the roller can slide along the tow rather than roll, the shoe and roller can be made out of a single piece as the roller and shoe don’t need to actuate separately. Controlling the rotational position is necessary as then any thickness of tow can have molded sides and the tow can be spread effectively at the crossover points. Both of these concepts can be seen in figure 83.

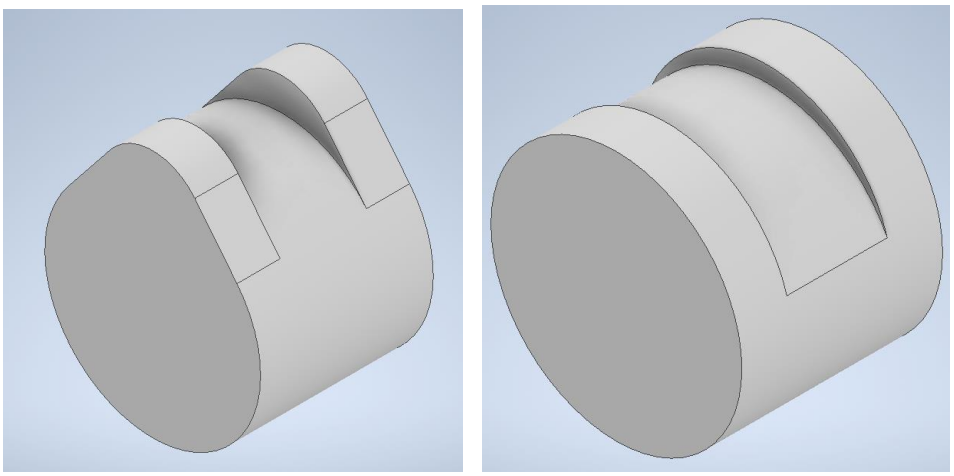

Figure 83: Concepts for single piece roller and shoe design.

6.4 Direct Width/Thickness Monitoring

Rather than relying on indirect geometric control of the sample, such as controlling the force of deposition, or having open loop control of the geometry, such as a predetermined step size, direct control of the geometry is preferred. Open loop control can be successful but requires fine tuning of the build plate or highly accurate bed leveling. Additionally, the flatness of the bed can have a significant impact on the part quality.

One option is to monitor the width of the tow during printing. The width of the tow is related to the thickness as it is assumed the tow has a constant volume. By controlling the width, the thickness can be controlled as well. One possibility is to use a vision system to monitor the width of the tow and feed that data back to control the width/thickness. Some issues with this are the glass tow is transparent and generally difficult to recognize using computer vison. Additionally, the build plate material can affect the contrast between the tow and the background. Retuning the system for differing build plates is a possibility but not desirable. Finally, the change in light in the environment can affect the accuracy of the vision system. Tuning the system to accept the lighting conditions throughout the day is undesirable; the system should be insensitive to such inconsistencies. This is most likely a minor issue as lighting in industrial environments is generally consistent.

Using a thermal camera to detect the edge of the tow is another option. Using a vision system with a thermal camera may have some merit as the contrast between the hot tow and the build plate. This was explored and there was difficulty when the thermal image was treated as a digital image. It was often difficult to distinguish the tow with the build plate. This was due to the rapid cooling of the tow. Also, thermal cameras will rescale the colors in the image based on the hottest object in the field of view. Thus, a 50C difference between the tow and build plate was effectively lost when compared to the 200C difference between the roller and build plate. Instead of using a vision system, the thermographic data could be used to find the edge of the tow where the temperature gradient isn't lost due to the hottest object in the field of view. However, thermal imaging has much worse resolution compared to traditional digital imaging. Also, high resolution thermal cameras are not only expensive but difficult to package on a mobile head. Finally, due to the amount of data is processed by the thermal imaging cameras, the frame rate can be relatively low. This can result in a system that cannot respond quickly enough for the processing speeds required.

Directly monitoring the height of the roller off the build plate is the final alternative path. This can give consistent layer height across a build plate of varying flatness and parallelism. This directly measures the layer thickness and therefore can directly control this variable. It is not clear, however, if low-cost sensors can meet the requirements. Also, manufacturing on a prefabricated face sheet may not result in accurate parts due to the surface roughness of the face sheet.

6.5 Refeed System Improvements

While the refeed system works well, it could still use improvement. One of the primary issues with the current system is the tensioning method. Passing the tow through a tube does add tension to the system but the tension is constantly applied. During refeed, this causes some issues as the tow has to be tacked and then dragged through the system for a successful refeed. The added tension requires more tack

force to be present for the refeeding action to be successful. On the initial layers, there is enough heat conduction to the build plate to freeze the tow in place, creating sufficient tack force for the tow to refeed even at the highest tension level. By having an active tensioning system, the tow tension can be reduced during refeed and increased during the normal deposition. Further, changing the tension may be required steering of the tow. Alternatively, or in addition to, having forced air cooling would aid in the refeed of the tow at higher temperatures. As stated earlier, as the layers increase, the tow will not freeze against the substrate as there is not enough heat conducted out of the tow. Adding active cooling is one method of getting the tow to tack against the substrate. Both of these could improve the refeed of the tow.

An additional issue is fibers getting imbedded in the anvil roller during cutting. Changing the durometer of the roller or roller material (current material is polyurethane) are two potential solutions to this issue. The durometer of the roller was changed to effectively cut the PP fibers in the tow. Adding a system to recognize whether refeeding has occurred is an additional method of overcoming this issue. This could be done using computer vision. Computer vision is suggested as the sensing method most likely needs to be noncontact. Also, the failure to refeed is generally complex and can be caused by a variety of issues. Computer vision could categorize and recognize the differences between these failures.

6.6 Tow Steering

While not the emphasis of this work was with straight beams, one of the main advantages of using commingled tow as a feedstock is the ability for the tow to shear. This allows the tow to subsequently be steered. Tow steering is highly desirable as allows for creating composites in which the fibers accurately follow the load paths around discontinuities, such as window cutouts in a fuselage. For 3D printing, this increase in manufacturable geometries is critical for this technology to be competitive with current methodologies. Previous work at the CMMS has demonstrated this technology for the nozzle-based

printers [42], [43], [44], [50]. Some demonstration of the roller-based end effector has been done. Note: this is not done with molding shoe modifications.

Several example prints were done to demonstrate the capabilities of this system. One such part was a simple circle with a radius of 250mm. The print parameters were a roller temperature of 250C, a speed of 5mm/s, 12 layers tall, and had a layer height of 0.1mm. This sample can be seen in figure 84. This was a continuous path sample made with the turntable installed as part of the ABB robotic cell.

Figure 84: Circular sample.

Additionally, a continuous square was also printed, using similar parameters to the circle: a roller temperature of 250C, a speed of 5mm/s and had a layer height of 0.1mm. Only 5 layers were printed as this was only a demonstration piece. The geometry of the square was 400mm for all sides and the radius of the corner was 10mm. The overall result was positive but did not tack in the corners. This can be seen in figures 85 and 86.

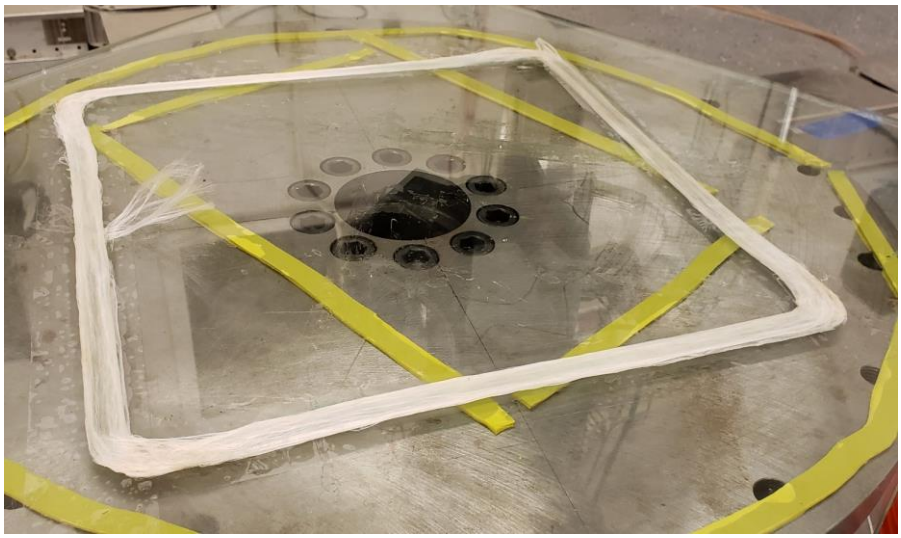

Figure 85: Final square part.

Figure 86: Fibers not tacking in corners.

These samples were manufactured before the force feedback control was implemented which is why that parameter was not specified. The lack of tacking could be due to a lack of forced cooling.

Other discontinuous steered samples were manufactured as well. One such sample was made after the beam optimization testing was done and used the optimized parameters for the 450mm/min (7.5mm/s) speed. Those parameters are a roller temperature of 240C, no tube (no added tension) and a force setpoint of 3lb. 20 layers were printed. This can be seen in figure 87.

Figure 87: Steered sample.

The curves have a 50mm radius. The roller was slowed by 75% for the duration of the curve. The tow had difficulty tacking along the curve as the layers increased. This is most likely due to heat being transferred to the build plate at lower layer counts; this effectively froze the matrix allowing the tow to be steered better.

Finally, in order to demonstrate the advantages of the tow steering applied to a grid stiffened panel, a curvilinear grid stiffened panel was printed with a face sheet. The parameters were the same as for the 450mm/min (7.5mm/s) speed. Those parameters are a roller temperature of 240C, no tube (no added tension) and a force setpoint of 3lb. Additionally, the optimized parameters for the crossovers was done as well: an increase in force to 25lb at the crossover and slowing the speed at the crossover by 75%. The face sheet was $[0/90]_2$ and the grid had 26 layers in it. This resulted in a part with 30 layers total. The face sheet dimensions were 500mmx500mm. This can be seen in figure 88.

Figure 88: Curvilinear grid stiffened panel.

This work on tow steering is a proof of concept but further iteration is required. No actual quality evaluation of these parts has been done other than a cursory visual go-no-go. A bounding study to determine the limits of the steering capabilities would be appropriate as well as an optimization study. It was assumed that the tow would not tack at small radii as the tow was not frozen in place. Adding forced convection cooling may aid in steering smaller and smaller radii.

CHAPTER 7: CONCLUSIONS

The use of continuous fiber reinforced thermoplastic matrix composites for grid stiffened structures is an attractive option for lightweight design and recyclability. However, the widespread implementation of these continuous fiber grid stiffened composites is limited by the complex tooling required for manufacturing and the material buildup at the crossover points in the grid stiffened structure. The buildup of fibers at the crossovers can lead to geometric variation, which can compromise a design, but also can lead to a degradation of mechanical properties of the part. The reduction in mechanical properties is due to the out of plane fiber bending, or fiber bridging, causing a matrix rich region adjacent to the crossover; this region has a greater likelihood of containing voids due to a lack of consolidation.

Digital manufacturing has the potential to solve both of these problems with grid stiffened continuous fiber composite structures. Using digital manufacturing can not only eliminate the need for complex molds but can also eliminate the need for curing or reconsolidating the parts. Further, by decreasing the speed and increasing the force of deposition at the crossover points, the tow can be spread in-situ. This spreading of the tow not only results in a wider tow but also in a thinner tow; the thinning of the tow is what prevents the material buildup at the crossover points. Previous nozzle-based deposition systems developed at the CMMS have demonstrated the ability to additively manufacture grid stiffened structures of uniform thickness in the grid stiffener and intersection, using continuous fiber composites at the lab scale. However, the lack of cut and refeed capabilities limit these systems to manual stopping, cutting and restarting, or printing using continuous paths. Also, these nozzle-based systems rely on open loop control of the consolidation force. These are major hurdles for moving digital manufacturing beyond the lab scale and into an industrial setting.

By developing a cut and refeed system and a roller-based deposition end effector, this work moves digital manufacturing towards a more robust, industry-ready technology. The cut and refeed system integrates the two separate systems into one and reduces the number of required actuators to one. A single stepper motor is required for cutting and refeeding. Further, implementation of closed loop force feedback control results in a system that can directly control the consolidation force in real time. Finally, this system can be fitted to many other 6-axis robotic arms with a minimal amount of retooling; only a mounting adapter plate needs to be remanufactured.

The roller-based end effector was able to manufacture grid stiffeners of comparable void content as the nozzle-based system. Also, the stiffer roller-based system had less thickness deviation between the beams and the crossovers. The greater the deviation between the beam and crossover the greater the amount of fiber bridging. Fiber bridging can lead to a greater number of voids in the beams adjacent to the crossover. Finally, by slowing the deposition speed of both nozzle and roller-based systems, the void content and thickness deviation of the crossovers was reduced. This is due to the matrix being exposed to the heat of the nozzle/roller for a longer period of time, which increases the temperature and reduces the viscosity of the matrix. The reduction of viscosity allows for the voids to be removed more easily and the tow can spread more as there is less resistance from the matrix.

Optimum levels for tension, temperature and force were found so that a consistent part thickness could be achieved for 450mm/min, 600mm/min and 750mm/min. Generally, the higher the roller temperature, the more the tow spread and the less voids where present. Also, the slower the speed, the more spreading occurred, and fewer voids were found. Increasing the force had a huge impact causing the tow to thin but resulted in only a limited reduction in void content. Changing the tension, by itself, had a limited impact on both tow spreading and void content. Interestingly, the tension and temperature interacted in an unexpected way. At a low roller temperature, increasing the tension caused thickening to occur while at higher temperatures, the increase in tension caused the tow to thin. This is most likely

due to the high matrix viscosity at the lower temperature constraining the tow, preventing thinning or spreading. Finally, during a microscope analysis of specific sections, unmelted polymer fibers were seen between layers, on the bottom side of the tow. It was assumed that this was due to not enough heat transferring through the thickness of the tow, from the heated roller.

A more formal optimization of the crossover thickness was also done. Two parameters were examined: the speed and the consolidation force at the crossover. Decreasing the speed and increasing the force at the crossover was necessary to spread the tow and minimize the material buildup at the crossovers. The constituent materials were also examined; it was found that the sample with decreased speed and increased force also had the lowest void content. When a metallographic sample was examined, it was observed that the thinnest crossover sample had the least amount of resin rich areas, and subsequent voids, adjacent to the crossover. This confirmed the assumption that more fiber bridging results in more voids adjacent to the crossover.

Finally, all of these advancements culminated with the manufacture of a curvilinear grid stiffened panel and preliminary work manufacturing a fully molded beam sample.

This work has not only demonstrated the ability for the roller deposition system to manufacture tow steered composites, but also exhibited the capability to autonomously make discrete fiber paths with a greater degree of control at a higher deposition speed and of comparable quality to the nozzle base systems.

REFERENCES

1. Baker, Alan A. *Composite materials for aircraft structures*. AIAA, 2004.
2. “Guide to compression molding from prototyping to mass production”*,* Formlabs, https://formlabs.com/blog/compression-molding/
3. Hoa, Suong V. *Principles of the manufacturing of composite materials*. DEStech Publications, Inc, 2009.
4. Brasington, Alex, et al. "Automated fiber placement: A review of history, current technologies, and future paths forward." *Composites Part C: Open Access* 6 (2021): 100182.
5. Crosky, A., et al. "Fibre placement processes for composites manufacture." *Advances in composites manufacturing and process design*. Woodhead Publishing, 2015. 79-92.
6. Brasington, Alex, et al. "A review and framework for modeling methodologies to advance automated fiber placement." *Composites Part C: Open Access* 10, 2023: 100347.
7. Denkena, Berend, Carsten Schmidt, and Patricc Weber. "Automated fiber placement head for manufacturing of innovative aerospace stiffening structures." *Procedia Manufacturing* 6, 2016: 96-104.
8. Pourahmadi, Emad, Rajamohan Ganesan, and Farjad Shadmehri. "Micromechanical characterization of Carbon/PEEK thermoplastic composite material in-situ consolidated by automated fiber placement: Stiffness prediction." *Composites Science and Technology* 246 2024: 110390.
9. Sloan, Jeff., “What Is the Genesis of Automated Tape Laying Technology?*”, CompositesWorld*, October 15, 2020. https://www.compositesworld.com/articles/what-is-the-genesis-of-automated-tape-laying-technology.
10. Karlson, H., and E. Hardesty. "Composite-tape placement head." U.S. Patent No. 3,775,219. 27 Nov. 1973.

11. Calawa, Rick, and John Nancarrow. *Medium wave infrared heater for high-speed fiber placement*. No. 2007-01-3842. SAE Technical Paper, 2007.
12. Rizzolo, Robert H., and Daniel F. Walczyk. "Ultrasonic consolidation of thermoplastic composite prepreg for automated fiber placement." *Journal of Thermoplastic Composite Materials* 29.11 (2016): 1480-1497.
13. Deden, Dominik, et al. "Comparison of heat sources for automated dry fibre placement: Xenon flashlamp vs. infrared heating." (2019).
14. Boon, Yi Di, Sunil Chandrakant Joshi, and Somen Kumar Bhudolia. "Filament winding and automated fiber placement with in situ consolidation for fiber reinforced thermoplastic polymer composites." *Polymers* 13.12 (2021): 1951.
15. Funck, R., and M. Neitzel. "Improved thermoplastic tape winding using laser or direct-flame heating." *Composites Manufacturing* 6.3-4 (1995): 189-192.
16. Lamontia, Mark A., et al. "Conformable compaction system used in automated fiber placement of large composite aerospace structures." *23rd SAMPE EUROPE Conference, Paris*. 2002.
17. Donough, Matthew J., et al. "Process modelling of In-situ consolidated thermoplastic composite by automated fibre placement–A review." *Composites Part A: Applied Science and Manufacturing* 163 (2022): 107179.
18. Jiang, Junxia, Yuxiao He, and Yinglin Ke. "Pressure distribution for automated fiber placement and design optimization of compaction rollers." *Journal of Reinforced Plastics and Composites* 38.18 (2019): 860-870.
19. Bakhshi, Nima, and Mehdi Hojjati. "Effect of compaction roller on layup quality and defects formation in automated fiber placement." *Journal of Reinforced Plastics and Composites* 39.1-2 (2020): 3-20.

20. Song, Qinghua, et al. "Research on void dynamics during in situ consolidation of CF/high-performance thermoplastic composite." *Polymers* 14.7 (2022): 1401.
21. Deignan, A., W. F. Stanley, and M. A. McCarthy. "Insights into wide variations in carbon fibre/polyetheretherketone rheology data under automated tape placement processing conditions." *Journal of Composite Materials* 52.16 (2018): 2213-2228.
22. Muzzy, John D., Yi Zhang, and Jurron Bradley. "Flow of thermoplastics through fiber assemblies." *5th International conference in flow processes in composite materials*. 1999.
23. Wong, Joanna CH, Javier Molina Blanco, and Paolo Ermanni. "Filament winding of aramid/PA6 commingled yarns with in situ consolidation." *Journal of Thermoplastic Composite Materials* 31.4 (2018): 465-482.
24. Heathman, Nathaniel, et al. "In situ consolidation of carbon fiber PAEK via laser-assisted automated fiber placement." *Composites Part B: Engineering* 249 (2023): 110405.
25. Jiang, Wei, et al. "Carbon nanotube-induced localized laser heating toward simultaneously enhanced laydown efficiency and fracture toughness of in-situ consolidated glass fiber thermoplastic composites." Composites Part B: Engineering 280 (2024): 111531.
26. Donough, Matthew J., et al. "Influence of deposition rates on the mode I fracture toughness of in-situ consolidated thermoplastic composites." *Composites Part B: Engineering* 251 (2023): 110474.
27. Chanteli, Angeliki, et al. "Influence of repass treatment on carbon fibre-reinforced PEEK composites manufactured using laser-assisted automatic tape placement." *Composite Structures* 248 (2020): 112539.
28. Shadmehri, F., et al. "Effect of in situ treatment on the quality of flat thermoplastic composite plates made by automated fiber placement (AFP)." *Advanced Manufacturing: Polymer & Composites Science* 4.2 (2018): 41-47.

29. Huybrechts, Steven M., S. Hahn, and T. Meink. "Grid Stiffened Structures: A Survey of Fabrication." *Analysis and Design Methods* (1999).
30. Zhao, Cong, et al. "Influences of ply waviness and discontinuity on automated fibre placement manufactured grid stiffeners." *Composite Structures* 256 (2021): 113106.
31. Huybrechts, Steven M., et al. "Manufacturing theory for advanced grid stiffened structures." *Composites Part A: Applied Science and Manufacturing* 33.2 (2002): 155-161.
32. Buragohain, M., and R. Velmurugan. "Study of filament wound grid-stiffened composite cylindrical structures." *Composite Structures* 93.2 (2011): 1031-1038.
33. Lee, Yeon-Gwan, et al. "Compressive strength stabilizing manufacturing method of anisogrid composite structure ribs without an outer skin." *Composites Part B: Engineering* 203 (2020): 108452.
34. Ahmadi, Hamed, and Gholamhossein Rahimi. "Analytical and experimental investigation of transverse loading on grid stiffened composite panels." *Composites Part B: Engineering* 159 (2019): 184-198.
35. Shroff, Sonell, Ertan Acar, and Christos Kassapoglou. "Design, analysis, fabrication, and testing of composite grid-stiffened panels for aircraft structures." *Thin-Walled Structures* 119 (2017): 235-246.
36. Qureshi, Z., et al. "In situ consolidation of thermoplastic prepreg tape using automated tape placement technology: Potential and possibilities." *Composites Part B: Engineering* 66 (2014): 255-267.
37. *Continuous carbon fiber - high strength 3D printing material*. Markforged. https://markforged.com/materials/continuous-fibers/continuous-carbon-fiber
38. *Desktop anisoprinting*. Anisoprint. https://anisoprint.com/solutions/desktop/, Nov. 2022
39. *Leverage the power of Carbon Fiber Composites*. Homepage. https://www.9tlabs.com/materials

40. Hedin, Kevin M. *A Thermoplastic Matrix Continuous Fiber Reinforced Composite Impregnation Method by Direct Polymer Extrusion*. Diss. Colorado State University, 2018.
41. Radford, Donald W., and Kevin M. Hedin. "Fused Deposition Technology Applied to Thermoplastic Matrix Placement and Wetout in Filament Winding." *20th International Conference on Composite Materials*. 2015.
42. Warlick, Kent M. *The Effect of Tow Shearing on Reinforcement Positional Fidelity in the Manufacture of a Continuous Fiber Reinforced Thermoplastic Matrix Composite via Pultrusion-Like Processing of Commingled Feedstock*. Diss. Colorado State University, 2017.
43. Warlick, K. M., and D. W. Radford. "Combining aspects of additive manufacture and filament winding to produce composites with novel fiber reinforcement patterns, 3rd Annu." *Compos. Adv. Mater. Expo CAMX 2016* (2016).
44. Warlick, K. M., and D. W. Radford. "Tow Positional Fidelity in a Continuous Fiber/3D Printing Approach on a Curved Surface." *Proceedings of the CAMX* (2017).
45. Rodriguez, P. A., and D. W. Radford. "Effect of Applied Consolidation Pressure in Direct Digital Manufacture of Continuous Fiber Reinforced Composites." *Proceedings of the CAMX Conference, Orlando, FL, USA*. 2017.
46. Rodriguez, Patrick A., and Donald W. Radford. "A DMA-based approach to quality evaluation of digitally manufactured continuous fiber-reinforced composites from thermoplastic commingled tow." *Journal of Composites Science* 6.2 (2022): 61.
47. Rodriguez, Patrick A. *Dynamic Mechanical Analysis for Quality Evaluation of Additively Manufactured Continuous Fiber Reinforced Thermoplastic Matrix Composites subject to Manufacturing Defects*. Diss. Colorado State University, 2019.

48. Bourgeois, Mark E., and Donald W. Radford. "Digital Manufacture of a Continuous Fiber Reinforced Thermoplastic Matrix Truss Core Structural Panel Using Off-the-Tool Consolidation." *Journal of Composites Science* 6.11 (2022): 343.
49. Bourgeois, Mark E., and Donald W. Radford. "Consolidation and tow spreading of digitally manufactured continuous fiber reinforced composites from thermoplastic commingled tow using a five-axis extrusion system." *Journal of Composites Science* 5.3 (2021): 73.
50. Hogan, Steven J., and Donald W. Radford. "COMPOSITE GRID STIFFENERS: Direct Digital Manufacture of Continuous Fiber Reinforced Thermoplastic High Aspect Ratio Composite Grid Stiffeners with Radically Reduced Tooling." *SAMPE Journal* 59.1 (2023).
51. Qureshi, Z., et al. "In situ consolidation of thermoplastic prepreg tape using automated tape placement technology: Potential and possibilities." *Composites Part B: Engineering* 66 (2014): 255-267.
52. Gardiner, Ginger. “Integrating Antennas into Composite Aerostructures.” *CompositesWorld*, www.compositesworld.com/articles/integrating-antennas-into-composite-aerostructures.
53. Hogan, Steven J. *DIRECT DIGITAL MANUFACTURE OF CONTINUOUS FIBER REINFORCED THERMOPLASTIC HIGH ASPECT RATIO COMPOSITE GRID STIFFENERS AND GRID STIFFENER INTERSECTIONS WITH RADICALLY REDUCED TOOLING.* Master’s Thesis, Colorado State University, 2024.
54. “Parts for 1171-a Chopper Gun.” *Fibre Glast Developments Corp*, www.fibreglast.com/product/Parts_for_1171_A_Chopper_Gun_1850.
55. “Spray-up Process.” *Manufacturing Products for Spray-up Process*, www.eppcomposites.com/spray-layup-process.html.
56. Xie, Yingxi, et al. "Fracture behavior of PAN-based carbon fiber tow in a chopping process on an elastic support." *Fibers and Polymers* 17 (2016): 1262-1268.

57. Lu, Longsheng, et al. "Fracture analysis of a single polyacrylonitrile-based carbon fiber in rigid-fixing and flexible-fixing chopping processes." *Textile research journal* 87.12 (2017): 1435-1444.
58. Alexander, Ryan W. *The Effect of Backing Material on Carbon Fibre Severing for High-Volume Production of Composites*. The University of Western Ontario (Canada), 2015.
59. Freeman-Gibb, Evan, Jennifer Johrendt, and O. Remus Tutunea-Fatan. "The Effect of Backing Profile on Cutting Blade Wear during High-Volume Production of Carbon Fiber-Reinforced Composites." *SAE International Journal of Materials and Manufacturing* 11.4 (2018): 491-498.
60. Adamovsky, Michael Francis Anthony. *The Effect of Cutting Blade Geometry and Material on Carbon Fiber Severing as Used in High-Volume Production of Composites*. The University of Western Ontario (Canada), 2015.
61. Michaeli, W., and S. Hoelzel. "Production of near net shaped preforms from chopped FRTP hybrid rovings." *47 th International SAMPE Symposium and Exhibition 2002*. 2002.
62. Foreyt N., et al., "Continuous Fiber End Effector"*, Senior Design Practicum Final Report*, Colorado State University, 2019.
63. Bahar, Mohammad, and Michael Sinapius. "Adaptive feeding roller with an integrated cutting system for automated fiber placement (AFP)." *Journal of Composites Science* 4.3 (2020): 92.
64. "Nip Impressions: American Roller: Plasma Coatings." American Roller Company, 31 July 2018, americanroller.com/us/nip-impressions/.
65. Figure 1. Automated Fiber Placement (AFP) Process., www.researchgate.net/figure/Automated-Fiber-Placement-AFP-process_fig1_319491071.
66. "ASTM D792-20: Standard Test Methods for Density and Specific Gravity (Relative Density) of Plastics by Displacement".
67. "ASTM D3171-15 Standard Test Methods for Constituent Content of Composite Materials".

68. Gleadall, “Fullcontrol Gcode Designer: Open-Source Software For Unconstrained Design In Additive Manufacturing”, *Additive Manufacturing*, vol. 46, 2021
69. Roy, Ranjit K. *A primer on the Taguchi method*. Society of manufacturing engineers, 2010.
70. Krishnaiah, K., and P. Shahabudeen. *Applied design of experiments and Taguchi methods*. PHI Learning Pvt. Ltd., 2012.
71. Irfan, M. S., et al. "Lateral spreading of a fiber bundle via mechanical means." *Journal of Composite Materials* 46.3 (2012): 311-330.
72. Zhou, Qihong, et al. "Analysis and prediction of the width of spreading carbon fiber tow based on gray system theory." *Journal of Applied Polymer Science* 138.12 (2021): 50069.
73. Hopmann, Christian, et al. "Impact of winding parameters on the fiber bandwidth in the cylindrical area of a hydrogen pressure vessel for generating a digital twin." *Polymer Composites* 43.3 (2022): 1577-1589.
74. Oromiehie E, Garbe U, Gangadhara Prusty B. “Porosity analysis of carbon fibre-reinforced polymer laminates manufactured using automated fibre placement”. *Journal of Composite Materials*. 2020;54(9):1217-1231. doi:10.1177/0021998319875491